In Vitro Primary Neuron and *Ex Vivo* Retina Stimulation with Optoelectronic Biointerfaces

by

Hümeyra Nur Kaleli

A Dissertation Submitted to the
Graduate School of Health Sciences in Partial
Fulfillment of the Requirements for the Degree
of

Doctor of Philosophy

in

The Cellular and Molecular Medicine

KOÇ ÜNİVERSİTESİ

February 04, 2025

In Vitro Primary Neuron and *Ex Vivo* Retina Stimulation with Optoelectronic Biointerfaces

Koç University

Graduate School of Health Sciences

This is to certify that I have examined this copy of a doctoral dissertation by

Hümeyra Nur Kaleli

and have found that it is complete and satisfactory in all respects,
and that any and all revisions required by the final
examining committee have been made.

Committee Members:

Prof. Celal Murat Hasanreisoğlu (Advisor)

Prof. Afsun Şahin

Prof. Sedat Nizamoğlu

Prof. Yasemin Gürsoy Özdemir

Assoc. Prof. Hatice Tuba Atalay

Date: February 04, 2025

Sevgili aileme,

ABSTRACT

In Vitro Primary Neuron and *Ex Vivo* Retina Stimulation with Optoelectronic Biointerfaces

Hümeyra Nur Kaleli

Doctor of Philosophy in The Cellular and Molecular Medicine

February 04, 2025

Progressive vision impairment generally arise due to irreversible photoreceptor damage in retinal degenerative diseases. Although there are applications aimed at improving patients' life quality, the exact treatment of these diseases has not been found. Optoelectronic approaches aim to perceive the incoming light and convert it into electrical signals by performing an artificially similar function of photoreceptors, and to activate retinal neurons to send signals for perceiving light in brain.

Development of optoelectronic biointerfaces provides new strategies for therapeutic application in vision-related diseases. This thesis aims to investigate the design of photovoltaic devices, biocompatibility and functional applications. Fabricated novel biointerfaces were tested in *in vitro* culture conditions and *ex vivo* retinal stimulation. The final part of the thesis includes the optimization of an *in vivo* optic nerve injury model for further prosthesis testing in the future.

The first part of the results consists of *in vitro* tests including cell viability, intracellular stress level, mitochondrial health, calcium influx of primary embryonic hippocampal neurons cultured on different photovoltaic device designs based on P3HT:ITIC and $AgBiS_2$ quantum dots. More than 80% cell viability and minimal stress under light illumination made the biointerfaces suitable candidates for further studies. The next part includes the final design of $AgBiS_2$-based devices with return layer of RuO_2 and interlayer of ZnO nanowires to improve photocurrent and photovoltage values. In addition to the biocompatibility and functionality tests on primary hippocampal neurons, the stimulation capacity of $AgBiS_2$-based biointerface

was validated by *ex vivo* retinal recordings from rats with retinal degeneration under repetitive near-infrared light illumination. The last part includes the optimization of animal studies for optic nerve crush model. Histological and functional analysis showed that injury-related conditions such as retinal layer deformation, gliosis, fibrosis and decrease in retinal ganglion cell activity progressed with increasing injury duration. The *in vivo* model provided a new platform to study the neuroprotective and neuroregeneration capacity of photovoltaic devices in the future.

ÖZET

Optoelektronik Biyoarayüzler ile *In Vitro* Primer Nöron ve *Ex Vivo* Retina Uyarımı

Hümeyra Nur Kaleli

Hücresel ve Moleküler Tıp Doktora

04 Şubat 2025

Retinal dejeneratif hastalıklarda genellikle ilerleyici görme kaybı geri dönüşümsüz fotoreseptör hasarına bağlı olarak ortaya çıkar. Bu gibi hastalıklarda klinik açıdan hastalık seyrini daha iyileştirmeye yönelik uygulamalar olsa da tam olarak tedavi sağlayan çözümler bulunamamıştır. Optoelektronik yaklaşımlar, fotoreseptörlerin yapay olarak benzer bir işlevini yerine getirerek gelen ışığı algılayıp elektrik sinyallerine dönüştürmeyi ve retina nöronlarını aktive ederek beyinde ışığı algılamaya yönelik sinyaller göndermeyi amaçlamaktadır.

Optoelektronik biyoarayüzlerin geliştirilmesi, görmeyle ilgili hastalıklarda terapötik uygulama için yeni stratejiler sağlar. Bu tez, fotovoltaik cihazların tasarımını, biyouyumluluğu ve işlevsel uygulamaları araştırmayı amaçlamaktadır. Üretilen yeni biyoarayüzler, *in vitro* kültür koşullarında ve *ex vivo* retinal stimülasyonlar ile test edilmiştir. Tezin son kısmı, gelecekte daha fazla protez testi için *in vivo* optik sinir yaralanması modelinin optimizasyonunu içermektedir.

Sonuçların ilk kısmı P3HT:ITIC ve $AgBiS_2$ kuantum noktalarına dayalı farklı fotovoltaik cihaz tasarımları üzerinde kültürlenen birincil embriyonik hipokampal nöronların hücre canlılığı, hücre içi stres seviyesi, mitokondriyal sağlık, kalsiyum akışı dahil olmak üzere *in vitro* testlerden oluşmaktadır. Hücre canlılığının %80'inden fazla oluşu ve ışık aydınlatması altında minimal strese sahip olması biyoarayüzleri ilerleyen çalışmalar için uygun aday kılmıştır. İkinci kısım, fotoakım ve fotovoltaj değerlerini iyileştirmek için geri dönüş elektrodu RuO_2 ve ZnO nanotellerinin ara katmanına sahip $AgBiS_2$ tabanlı cihazların son tasarımını içermektedir. Birincil hipokampal nöronlar üzerindeki biyouyumluluk ve işlevsellik testlerine ek olarak, $AgBiS_2$ tabanlı biyoarayüzün uyarılma kapasitesi, tekrarlayan yakın kızılötesi ışık aydınlatması altında retina dejenerasyonuna uğramış sıçanlardan alınan *ex vivo* retina

kayıtları ile doğrulanmıştır. Son kısım, gören sıçanlarda *in vivo* optik sinir yaralanması modelinin optimizasyonunu içermektedir. Histolojik ve fonksiyonel analiz, retina katmanlarının deformasyonu, gliozis, fibrozis ve retina ganglion hücre aktivitesinde düşüş gibi yaralanmaya bağlı durumlar hasar süresinin artışı ile ilerlediği gösterilmiştir. *In vivo* model, gelecekte fotovoltaik cihazların nöroprotektif ve nörorejenerasyon kapasitesini incelemek için yeni bir platform sağlamıştır.

ACKNOWLEDGMENTS

I want to thank Prof. Celal Murat Hasanreisoğlu for allowing me for my individual progress in the mentorship of undergrad and grad students, writing grant proposals, project managements and becoming an independent researcher. I want give my special thanks to Prof. Afsun Şahin for supporting me to work as an active researcher in corneal crosslinking and cornea stem cell studies during my PhD. My special gratitudes to Prof. Sedat Nizamoğlu for supporting me in the field of optoelectronic biointerface studies, providing all the opportunities as the researchers in his own team, introducing me to researchers in and out of the field, and creating a network. My special gratitudes to my external PhD thesis jury members; Assoc. Prof. Hatice Tuba Atalay and Prof. Yasemin Gürsoy Özdemir for their valuable time to evaluate my thesis.

My current and former team mates at Vision Research Lab; Şeyma Yaman, Gülsüm Deniz, Dr. Erdost Yıldız, Dr. Eda Kuşan, and especially my queen sisters; Dr. Ayşe Dilara Aydemir, Merve Gözel, Zehra Canbulat and Çiğdem Pehlivan, I am grateful for all your contributions. My queen sisters, I am grateful for your support, your nice conversations, scientific discussions and the unforgettable memories we made here and at abroad. Sincere thanks to our clinician group; Dr. Cem Kesim and Assoc. Prof. Ayşe Yıldız for their assistance. Current and former team members at my second lab (IDEALAB); Dr. Onuralp Karatüm, Dr. Güncem Özgün Eren, Asım Önal, Rıdvan Balamur, Ömer Faruk Özelci, Tarık Safa Kaya, Berkay Uğur Çalışkan, Gizem Yıldız, Lokman Kaya, and Muhammad Hassnain, thank you for your efforts and our coffee times, we had a good time.

I want to thank students, technicians, researchers and professors working at KUTTAM for providing intellectual environment, giving experimental advices and sharing materials or equipment in case of any need. I want to express my thanks to Uğur Çerez, Şimal Laçin, Seyit Aydın, Zeynep Kahya, İmren Karaca and Güven Ayvaz for their assistance on materials and technical support 7/24. I want to thanks to my colleagues and collaborators; Prof. Seda Kızılel, Prof. Önder Metin, Dr. Zafer Eroğlu, Ayesha Gulzar, 252 Lab members especially; Dr. Gizem Söyler, Dr. Büşra Köse, Kardelen Yangın, İpek Yılmaz, Ecem Ayvaz, Dr. Duygu Aydemir, and Büşra Tekirdağlı. Sincere thanks to KUTTAM-ARF members for their technical and

experimental support during operations; Dr. Nilhan Coskun, Mustafa Demir, Emre Uğur, Ahmet Kocabay, Oğuzkan Yaralı, and Elif Abla.

I would like to thank Prof. Serge Picaud at Institut de la Vision Paris and his team, Dr. Antoıne Chaffiol and Corentin Joffrois, for opening their labs, trainings for ex vivo retinal measurements and providing multielectrode array recordings. I would like to acknowledge the European Union (ERC, MESHOPTO, 101045289) for partial support of my studies on MEA recordings and 2224-A Grant Program provided by TUBITAK for participation in scientific meetings abroad.

My dear friends who are just a phone call away even though we are far away; Kübra Kaleli, Tuğba Türk, Ayşen Endes, Gözde Sert, Ayşenur Bıdak, Huriye Türk and Meyra, thank you for your good wishes and support.

My deepest gratudes to my family; Sonnur Kaleli, Prof. Süleyman Kaleli, Dr. Muhammed Fatih Kaleli, Dr. Merve Buse Kultaş Kaleli, Karmen and Yaren for their eternal support. I love you and I am thankful to have you. I feel your continued support, your endless kindness and patience during all challenging times. None of my achievements would be complete without your deep belief in me.

TABLE OF CONTENTS

LIST OF TABLES xiii
LIST OF FIGURES xiv
ABBREVIATIONS xxii
1. CHAPTER 1 INTRODUCTION 1
1.1 Structure of Retina 1
1.2 Retinal Degeneration 6
1.3 Visual Prosthesis 9
1.4 Hypothesis and Aims 13
1.4.1. Aim 1 In vitro biocompatibility of devices 13
1.4.2. Aim 2 Recording of intracellular stress level under repetitive light illumination 13
1.4.3. Aim 3 In vitro biointerface activation 13
1.4.4. Aim 4 Ex vivo retina tissue isolation, optimization and recording 14
1.4.5. Aim 5 In vivo optic nerve injury model optimization 14
2. CHAPTER 2 MATERIALS and METHODS 15
2.1 Materials. 15
2.2 Biointerface Fabrication and Characterization 15
2.2.1 Fabrication of P3HT:ITIC Biointerface 15
2.2.2 Fabrication of Quantum Dots or Nanocrystal based Photovoltaic Biointerfaces 16
2.2.3 Characterization of Biointerfaces 16
2.3 Cell Culture 17
2.3.1 Animal Ethics 17
2.3.2 SH-SY5Y Neuroblastoma and Müller Glia Culture 17
2.3.3 Primary Neuron Isolation and Culture 17
2.3.4 Primary Astrocyte Culture Condition 18
2.3.5 Preparation of Substrates for Cell Culture 19
2.4 In Vitro Biocompatibility Tests 20
2.4.1 CTG Cell Viability Assays 20
2.4.2 Lactate-dehydrogenase (LDH) Release Assay 21
2.4.4 Live/Death assay with calcein AM and Propidium Iodide (PI) 21
2.4.5 Immunofluorescence Staining and Imaging 22

2.4.6 The cell number/mm^2 counting 22
2.4.7 Neurite Length Measurement 23
2.5 Intracellular ROS Assay 23
2.6 Mitochondrial Membrane Potential (MMP) Examination 23
2.7 Recording of in vitro Neural Responses with Calcium Imaging 24
2.8 Ex Vivo Retina Tissue Preparation and Multielectrode Array (MEA) recordings 25
2.8.1 Retina Preparation for Recording 25
2.8.2 Recording of Action Potential Ability with MEA 27
2.9 Optimization of In vivo Optic Nerve Crush (ONC) Model 28
2.9.1 Establishment of optic nerve damage model in rats 28
2.9.2 Electrode implantation on the skull for Visual Evoked Potential (VEP) Electroencephalography (EEG) Recordings 29
2.9.3 Electroretinography (ERG) and VEP-EEG measurements 30
2.10 Retina and Optic Nerve Immunohistochemically Analysis 31
2.10.1 Collection and Fixation of Tissues 31
2.10.2 Hematoxylin & eosin staining 32
2.10.3 TUNEL Assay 32
2.10.4 Immunofluorescence staining and imaging 33
2.11 Statistical Analysis 33
3. CHAPTER 3 RESULTS 34
3.1 P3HT:ITIC Photovoltaic Biointerfaces for Neural Photostimulation 34
3.1.1 Background 34
3.1.2 P3HT:ITIC biointerface fabrication and performance check 35
3.1.3 Biocompatibility Assessments of P3HT:ITIC Biointerface 38
3.2 Near Infrared Stimulation of Neurons by $AgBiS_2$ Nanocrystals 43
3.2.1 Background 43
3.2.2 Performance Assessments of $AgBiS_2$/P3HT:RuO_2 Biointerface 44
3.2.3 Biocompatibility Assessments of $AgBiS_2$/P3HT:RuO_2 Biointerface 45
3.3 Biointerfacing with $AgBiS_2$ Quantum Dots for Pseudocapacitive Photostimulation 52
3.3.1 Background 52
3.3.2 Photo-electrochemical performance of ITO/ZnO NW/AgBiS2 NC Biointerface 52
3.3.3 Biocompatibility of ITO/ZnO NW/$AgBiS_2$ NC Biointerface 53
3.4 Near infrared photostimulation of in vitro neuron and ex vivo retina via ZnO nanowire based $AgBiS_2$ NC 58

3.4.1 Background 58
3.4.2 Performance Analysis of ITO/ZnO NW/$AgBiS_2$ NC/P3HT:RuO_2 Biointerface ..59
3.4.3 Biocompatibility of ITO/ZnO NW/$AgBiS_2$ NC/P3HT:RuO_2 Biointerface 60
3.4.4 Ex vivo Retina stimulation through ITO/ZnO NW/$AgBiS_2$ NC/P3HT:RuO_2 Biointerface 67
3.5 A Preliminary Study to Determine ONC Injury Duration and Degree of Gliosis . 74
3.5.1 Background 74
3.5.2 ERG and VEP-EEG measurements 75
3.5.3 Histological Evaluation of Tissue Sections 77
4. CHAPTER 4 DISCUSSION 81
5. CHAPTER 5 FUTURE DIRECTIONS AND CONCLUSION 92
6. Appendix A List of Materials 95
7. Appendix B Ethical Committee Approvals 99
8. Appendix C Multielectrode Array Optimization 102
9. BIBLIOGRAPHY 106

LIST OF TABLES

Table 1.1. Clinical Trials 12
Table 6.1 Cell Culture Solutions & Reagents 95
Table 6.2 Antibodies for immunofluorescence staining 95
Table 6.3 Assays and Kits 96
Table 6.4 Chemicals & Reagents 96
Table 6.5 Preparation of Solutions and Culture Media 97
Table 6.6 List of Softwares 98
Table 6.7 List of Equipments 98

LIST OF FIGURES

Figure 1.1 Representative image of retina structure. Created with BioRender. 2
Figure 1.2 Illustration of phototransduction in photoreceptors. Adapted from (Klapper et al., 2016) 4
Figure 1.3 Comparison of healthy retina, retinitis pigmentosa and age related macula degenerated retina. Created with BioRender. 9
Figure 2.1 Demonstration of hippocampal and cortical tissue isolation from emryonic rat. A. Top and B. side views of the fetus after decapitation. C. Cutting the skull along the midline using fine-tipped forceps. D. Top and E. bottom views of the dissected brain. F. Superior and G. inferior views of the brain separated from its meninges. H. The area of hippocampus is visible after separating the right and left cortex in the middle. I. Post-dissection view of the crescent-shaped hippocampus. J. Cortex isolation after hippocampal dissection from the right and left cerebral hemispheres. K. Light microscope image of the primary neuron culture obtained from the hippocampus. L. Light microscope image of primary astrocyte and glia culture obtained from the cortex. 19
Figure 2.2 *In vitro* experimental procedure. Created with BioRender. 20
Figure 2.3 Schematic representation of *ex vivo* retina recording with MEA system. Created with BioRender.....25
Figure 2.4 Retina isolation from eyeball. The enucleated eyeball (A) was opened at the Cornea was seperated from the eyeball by cutting from corneoscleral junctions to isolate the retina (B). Isolated retina was placed on microelectrode array for recording (C). Schematic representation of retina on microelectrode array (D). The photovoltaic bionterface is placed toward the outer retina while retina ganglion cells are in contact with the microelectrode array. Illumination is given at the bottom of transparent MEA through microscope objectives. 26
Figure 2.5 MEA system compartments and retina placement representation A. Combined MEA amplifier system with the inverted light microscope. B. Retina

isolation unit. C. Perfusion and temperature controller unit. D. Perfusion inlet and outlet on MEA chamber. 27
Figure 2.6 Experimental flow of optic nerve crush and histological analysis. 28
Figure 2.7 Preliminary testing of A . optic nerve operation on a Wistar Albino rat that is not included in the main experimental group, followed by B. VEP-EEG electrode implantation. 29
Figure 2.8 Optic nerve crush procedure. The optic nerve area was accessed via A. lateral cantotomy, and the crush was performed using tweezers. B. Retinal fundus photographs of rats in the main experimental group captured using a 90D fundoscopy lens, C. operation followed by VEP-EEG electrode implantation. 30
Figure 3.1 ITO/ZnO/P3HT:ITIC device fabrication and characterization. A. Schematic representation of P3HT:ITIC biointerface structure. B. Biointerface's energy band diagram. C. Absorption spectrum of P3HT:ITIC biointerface. 35
Figure 3.2 Characterization of photoelectrical performance of ITO/ZnO/P3HT:ITIC device. A. Schematic representation of a three-electrode electrochemical measurement system for the photocurrent and photovoltage measurement. B. Photocurrent measurement of ITO/ZnO/P3HT:ITIC devices obtained by coating P3HT:ITIC (20 mg/ml, 1:1.5 mixing ratio) solution with spin coat speeds of 1000 rpm, 2000 rpm, and 4000 rpm. C. Photocurrent and D. photovoltage measurements of devices in ITO/ZnO/P3HT:ITIC under 780 nm, 1 mW/mm^2 light intensity. Light-colored rectangles show the intervals at which the 10 ms light pulse is applied. 37
Figure 3.3 Structural properties of P3HT:ITIC device. Surface characteristics of device with different magnification (top) and cross sectional view to show thickness of each layer (bottom). 38
Figure 3.4 Biocompatibility of P3HT:ITIC biointerface. Bright field light microscope images of primary neuron, primary astrocyte and Mio-M1 cells on ITO and P3HT:ITIC (A.,D.,G.) (Scale bar, 100μm). CTG analysis of neurons, primary astrocytes and Mio-M1 cells cultured ITO and P3HT:ITIC biointerface (B.,E.,H.,) and LDH cell viability results (C.,F.,I.) (mean ± SD for n = 4). 40
Figure 3.5 Comparison of primary cells cultured on ITO control and P3HT:ITIC biointerface by immunofluorescence staining. Primary neurons were stained with NeuN and F-actin to show expression of neuronal biomarker and to show structure. Primary astrocytes were stained with GFAP (Scale bar, 100μm). 41
Figure 3.6 Expression of glutamine synthetase of Mio-M1 cells cultured on ITO and biointerface (Scale bar, 100μm). 41

Figure 3.7 Calcium imaging of neuron on the biointerface (Scale bar, 100μm). 42
Figure 3.8 $AgBiS_2$ NC based biointerface electrochemical measurements. A. Schematic representation of ITO/ZnO/$AgBiS_2$/P3HT biointerface structure. Created with BioRender. B. Representation of energy band diagram. C. Visible to NIR absorption spectrum. D. ITO/ZnO/$AgBiS_2$/P3HT biointerface photocurrent response and control without $AgBiS_2$ under 780 nm NIR and 20 ms ON). F. Photovoltage value measured with 780 nm LED. G. Charge levels with different pulse durations. 44
Figure 3.9 Biocompatibility tests of SH-SY5Y neuroblastoma cells cultured on control ITO and biointerface device. A. Light microscope images of cells on ITO and device (Scale bar, 100μm). B. CTG cell viability assay (mean ± SD, n = 4). C. The integrity of the cell membranes on the materials is measured using the LDH leakage assay (mean ± SD for n = 4). 45
Figure 3.10 Biocompatibility tests of control ITO and ITO/ZnO/$AgBiS_2$ biointerface. A. During the two-week culture period, neurons were cultivated on ITO and biointerface. B. Immunofluorescence pictures of neurons grown on the ITO and ITO/ZnO/$AgBiS_2$ at Days 0 and 14. The nuclear marker DAPI (blue) and the neuronal structural marker anti-β-III-tubulin (green) were used to co-stain the cells (Scale bar: 100μm). 46
Figure 3.11 Cell viability tests of neurons cultured on biointerface. A. phase contrast images of neurons (Scale bar: 100μm). B. CTG and C. LDH cell viability of neuronal cells on ITO/ZnO/$AgBiS_2$/P3HT and ITO control samples. 47
Figure 3.12 Immunofluorescence images of neuronal nucleus on the ITO and biointerface. A. DAPI (blue) and Anti-NeuN (green) nuclear markers were used to co-stain the cells (Scale bar: 100μm). B. Comparison of NeuN expressed cells to the total amount of cells/mm^2 during culture period (mean ± SD, n = 4).....49
Figure 3.13 Immunofluorescence images of neuronal structures. A. Co-staining with DAPI (blue) and anti-βIII Tubulin (green) (Scale bar, 100μm). B. Comparison of neurite length (mean ± SD, n = 50 cells). 51
Figure 3.14 ZnO NW-$AgBiS_2$ NC based biointerface electrochemical measurements. A. Schematic representation of ITO/ZnO NW/$AgBiS_2$ biointerface structure. Created with BioRender. B. Representation of energy band diagram. C. Charge as function of illumination intensities under 780 nm light for 20 ms. D. Photocurrent of the control (ITO/ZnO seed/P3HT), devices with ITO/ZnO seed/$AgBiS_2$ and NW-QD under pulsed light illumination. The red line at the bottom indicates when the light is on, while the gray bar represents when the light is off. 53

Figure 3.15 The live/dead-calcein AM/PI co-staining was visualized for the viability of cells. Propidium iodide (PI) in red denotes dead cells, whereas calcein AM in green indicates living cells (Scale bar, 250 μm). 54
Figure 3.16 Changes in intracellular oxidative stress under light illumination. with ROS assay. A. ROS level of primary neurons cultured on device. Cells were illuminated with 780 nm LED with 10000 cycle, illumination: 5 Hz, 20 ms pulse and 1.5 mW.mm-2 intensity. ITO is negative control and ITO with H_2O_2 is positive control (Scale bar, 100 μm). B. Measured relative intracellular fluorescence intensities. 55
Figure 3.17 Mitochondrial membrane potential (MMP) changes in neurons cultured on biointerface. A. JC-1 red aggregates refer to healthy mitochondria while JC-1 green monomers show disrupted mitochondria. Cells were illuminated with 780 nm LED with 10000 cycle, illumination: 20 ms pulse, 5 Hz, 1.5 mW/mm^2 intensity. B. Mean fluorescence intensity of red and green signals in device before and after light illumination. C. Ratio of aggregate to monomer in device before and after light illumination. 56
Figure 3.18 Flou-4AM calcium imaging. A. Changes in fluorescence signals before, during, and after light illumination. B. Rainbow representation of calcium release of single neuron (red arrow) cultured on biointerface after 780nm light stimulation with stimulus frequency, 5 Hz; 20 ms pulse-width; light duration, 10s. C. Florescence intensity changes before and after illumination on single neurons. Light stimulation was performed at 60s for 10s. D. Mean of relative florescence intensity changes of eleven different neurons on biointerface.....57
Figure 3.19 Electrochemical features of ITO/ZnO NW/$AgBiS_2$ NC/P3HT:RuO_2 Biointerface. A. Schematic representation of biointerface structure. Created with BioRender. B. Cross-sectional SEM image. C. Photocurrent and D. photovoltage of the biointerface under 880 nm NIR light (20 ms, 89 mW/cm^2). E. Photogenerated charge density of the biointerface for different pulse durations. F. Charge density of the biointerface by change in light intensity. 60
Figure 3.20 Cell viability tests of neurons cultured on control and device. A. Bright field images of cells at DIV 3 (Scale bar, 100 μm). B. CTG assay for quantifying cell viability through cellular ATP level (mean ± SD, n = 4). ITO sample was used as a control. C. MTT assay for measuring cytotoxicity of neurons (mean ± SD, n = 4). D. LDH leakage from neurons (mean ± SD for n = 4). E. Relative cell viability. 61

Figure 3.21 Short and long term neuron culture on substrates. A. Co-staining with DAPI (blue) and anti-NeuN (green) (Scale bar, 100μm). B. Comparison of NeuN expressed and total number of cells per mm^2 during culture period shown in immunofluorescence images (mean ± SD, n=8). 62
Figure 3.22 Short and long term neuronal structural changes cultured on substrates. DAPI (blue) and anti-βIII-Tubulin (green)(Scale bar: 100μm). 63
Figure 3.23 Intracellular oxidative stress with ROS assay. A. Representative image of H_2DCFDA working principle. B. Stress level of primary neurons cultured on the biointerface was visualized after subjecting to 10000 photoexcitation cycle, illumination: 5 Hz, 20 ms pulse, 1.5 mW/mm^2 intensity. ITO is negative control, ITO with H_2O_2 is positive control (Scale bar, 50 μm). C. Measured relative intracellular fluorescence intensities. 64
Figure 3.24 Dynamic mitochondrial health assessment through JC-1 staining before and after light illumination. A. Schematic representation of mitochondrial membrane polarization. B. Bright field and fluorescence images of cells cultured on ITO control and devices. (Scale bar, 50 μM). Cells were subjected to 780 nm light for 2 sec with 5 Hz, 20 ms, 1.5 mW/mm^2 intensity. C. Average fluorescence intensity of green monomer and red aggregate in the device and control over time. D. Comparison of JC-1 aggregate to monomer fluorescence intensity ratio. 65
Figure 3.25 Calcium signal traces (Ft/F0) of randomly selected neurons before, during, and after light illumination. A. Schematic representation of calcium release under illumination. B. Calcium release of single neuron cultured on biointerface after 780nm light stimulation (stimulus frequency, 5 Hz; 20 ms pulse-width; light duration, 2s or 10s). C. Time dependent florescence intensity changes before and after illumination. D. Relative florescence intensity changes of selected cells on biointerface. E. Average of florescence intensity changes. F. Comparison of ITO control and the biointerface averaged florescence changes after 780nm light stimulation (stimulus frequency, 5 Hz; 20 ms pulse width; light duration, 2s). G. Area under the curve of graph F. 67
Figure 3.26 Light responsive electrodes during recording and their firing rate peaks at 5 and 10 ms pulse width. Red area indicated as 880 nm near-infrared (NIR) laser illumination pulses with 5 Hz frequency, 5 or 10 ms durations, ~5 mW/mm^2 power intensity for 100 repeats. 69
Figure 3.27 Averaged firing rate peaks of 5 ms and 10 ms light durations and RGC response during recordings. Spontaneous activity was indicated in graphs as active

electrode while light stimulation generated response indicated as responsive electrode. 70
Figure 3.28 Light responsive electrodes during recording and their firing rate peaks at 20 and 50 ms pulse width. Red area indicated as 880 nm near-infrared (NIR) laser illumination pulses with 5 Hz frequency, 20 or 50 ms durations, ~5 mW/mm^2 power intensity for 100 repeats. 71
Figure 3.29 Averaged firing rate peaks of 20 ms and 50 ms light durations and RGC response during recordings. Spontaneous activity was indicated in graphs as active electrode while light stimulation generated response indicated as responsive electrode. 71
Figure 3.30 Comparison of averaged firing rate peaks of 5, 10, 20 and 50 ms light durations and latency during recordings. 72
Figure 3.31 Averaged firing rate peaks of RGC response during 5, 10, 20 ms and 50 ms light durations at 5 Hz without active device. 73
Figure 3.32 Right eyes with ONC during the one-week recovery period after injury operation. 75
Figure 3.33 . ERG measurements in the Dark Agouti rat retina under 1 Hz frequency with 20 ms pulse width of white LED light stimulation at 500 μW/cm^2 light intensity. Pulsed lights are expressed as yellow dashes. 76
Figure 3.34 VEP-EEG measurements in the control and 120 sec ONC group under 1 Hz frequency with 20 ms pulse width of white LED light stimulation at 500 μW/cm^2 light intensity. Pulsed lights are expressed as yellow dashes 77
Figure 3.35 Hematoxylin and eosin-stained images of control and damaged Dark Agouti rat retina and optic nerve sections. Red blood cells represented as red arrows were observed in the injury groups (scale bar: 50μm). 78
Figure 3.36 The progressive increase in apoptotic cells in response to the ONC injury. TUNEL stained cells (red) and DAPI nuclear marker (blue). 78
Figure 3.37 Immunofluorescence staining of control 15 sec and 30 sec ONC rat retinas and optic nerve. Tissue sections were stained with the glial cell marker, GFAP (green), and the cell nuclear marker, DAPI (blue). 79
Figure 3.38 Immunofluorescence staining of control, 15 sec and 30 sec ONC rat retinas and optic nerve. Rat retinas and optic nerve were stained with the Müller cell indicator, glutamine synthetase (green), active Müller glia and fibroblast marker, Vimentin (orange), and the cell nucleus marker DAPI (blue). 80

Figure 3.39 Immunofluorescence staining of control 15 sec and 30 sec ONC rat retinas. Rat retinas were stained with the photoreceptor cell marker, rhodopsin (orange), the ganglion cell marker, NeuN (green), and the cell nucleus marker, DAPI (blue). retinas. 80
Figure 8.1 Measurement of photovoltage value of only 850 nm light with 100% power.....102
Figure 8.2 Measurement of photovoltage value of only 850 nm light with 50% power. 103
Figure 8.3 Measurement of photovoltage value of biointerface with MEA electrodes during 850 nm light illumination with 5 Hz frequency, 20 ms pulse and 50% intensity. 104
Figure 8.4 Retina recording with ITO/ZnO NW/$AgBiS_2$ NC/P3HT:RuO_2. a. retina on MEA electrode with and without bioinerface device (4 mm^2 in area). b. Spontaneous retina ganglion cell spikes at electrode M16. c. spike waveforms recorded from 256 individual electrodes, zoom in spike figure of electrode M16. d.Raster plot of 256 electrodes before and after 850nm light illumination with 5 Hz frequency, 20 ms pulse and 50% intensity.....105

ABBREVIATIONS

aCSF	Artificial cerebrospinal fluid
AMD	Age related macular degeneration
cGMP	Cyclic guanosine monophosphate
ERG	Electroretinography
GFAP	Glial fibrillary acidic protein
GS	Glutamine synthetase
H&E	Hematoxylin and eosin
H_2DFCDA	2',7'-dichlorodihydrofluorescein diacetate
ITO	Indium thin oxide
INL	Inner nuclear layer
LDH	Lactate-dehydrogenase
LGN	Lateral geniculate nucleus
MEA	Multi electrode array
MTT	3-(4,5-dimethylthiazol-2-yl)-2,5-diphenyltetrazolium bromide
NCs	Nanocrystals
NBM	Neurobasal medium
NeuN	Neuronal nuclei
NW	Nanowire
ONC	Optic nerve crush
OPL	Outer plexiform layer
P3HT	Polymer poly(3-hexylthiophene)
PFA	Paraformaldehyde
PI	Propidium Iodide
RPE	Retina pigment epithelium
RGC	Retina ganglion cells
RP	Retinitis pigmentosa
RuO_2	Ruthenium oxide
SEM	Scanning electron microscopy
SC	Superior colliculus
VEGF	Vascular endothelial growth factor
VEP	Visual evoked potential

1. CHAPTER 1

INTRODUCTION

1.1 Structure of Retina

Structure of eye consists of several parts including the cornea, sclera, limbus, conjunctiva, iris, lens, vitreous, retina, choroid, and optic nerve head. Retina is a well-organized tissue made up of multiple cellular layers that are synaptically connected to one another (Figure 1.1). The retina pigment epithelium (RPE), which locates at the most outer part, absorbs incoming photons without reflecting them, preventing scattering of light (Strauss, 2005). Photoreceptors both rods and cones locate in front of RPE layer. Rod photoreceptors are densely present in the outer regions of retina, which are responsive to detect contrasts as well as movements in dim light compared to cone photoreceptors (Bloomfield & Dacheux, 2001). They cannot detect fine color details, but they are well capable of distinguishing the brightness of view by their specialized photopigment, rhodopsin. Cones on the other hand allow us to perceive color vision under bright light (Chui et al., 2008).

In order to enhance fine signal transmission, photoreceptors synapse secondary neurons at the outer plexiform layer (OPL) and have one or more lateral connections with horizontal cells at the inner nuclear layer (INL). Single horizontal cell may arrange dendrites connected to multiple photoreceptors, so it is responsible for surround inhibition to improve perception of edges, boundaries, and fine details. Depending on the changes in light intensity, photoreceptor cells located away from light can reduce their activity with the signals generated by horizontal cells (Grünert & Martin, 2020). The connection of photoreceptor with secondary neurons in OPL maintains main visual transmission through inner plexiform layer (IPL), at which bipolar cells have connections with retina specific neuron cells named retina ganglion

cells (RGC). During signal processing, amacrine cells, which reside between bipolar and RGCs, facilitate lateral communication between several retinal ganglion cells by regulating visual signals spatially and temporally so enhancing the perception of edges, contrasts, and moving objects. Complex connection of RGCs as second order neurons enables to perceive details with high-resolution.

Retina also contains Müller glia, a specific kind of glial cells that perform maintenance and support functions (Grünert & Martin, 2020). Although they do not transmit electrical signals like neurons, they have important role on sustaining health and functioning of metabolic support, ion regulation, and recycling of neurotransmitters in synapses.

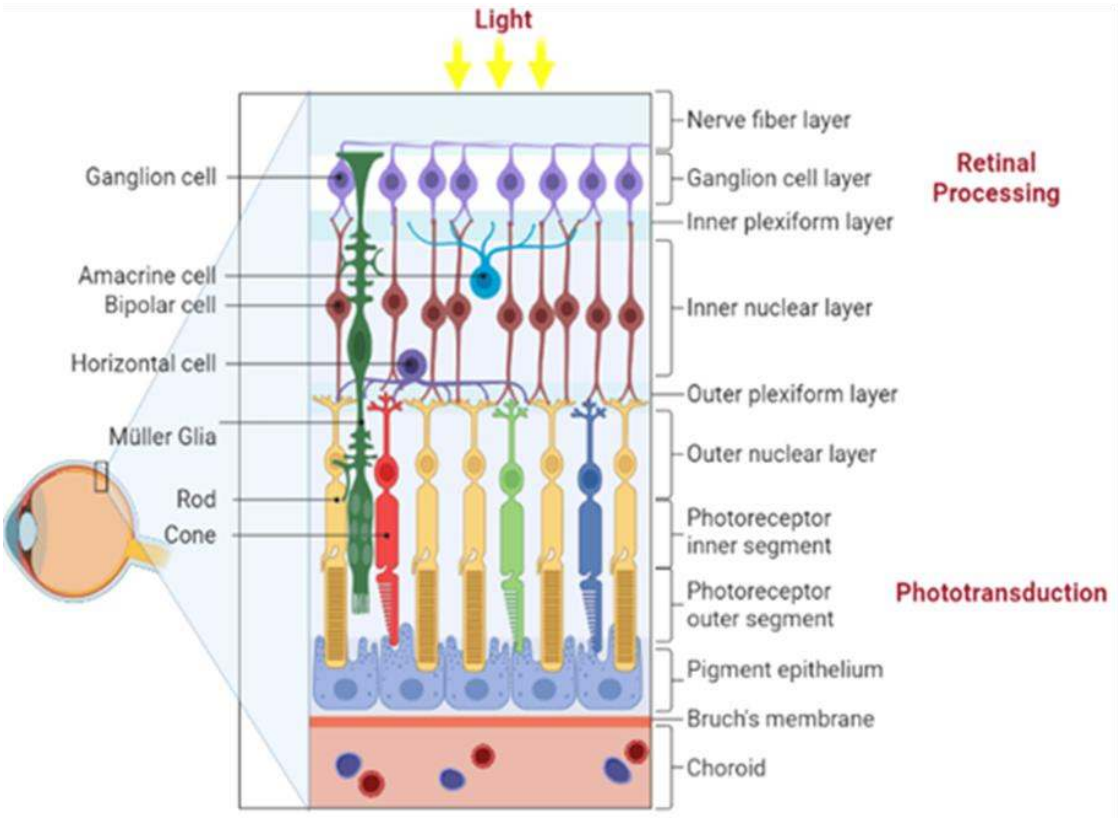

Figure 1.1 Representative image of retina structure. Created with BioRender.

When light reach the back of the eye, first, melanin pigments present in the retinal pigment epithelial cells absorb light and start signaling events named visual cycle between photoreceptors and RPE to maintain chemical signaling, named phototransduction (Rando, 2001). Phototransduction maintains converting photons into electrical signals (Figure 1.2).

The light-sensitive pigments are responsible for the recognition of photons (Rando, 2001). Photoreceptors when they are at rest in the dark constantly release glutamate as neurotransmitters by glutamate receptors. Glutamate is the principal neurotransmitter in the retina and is crucial for promoting and sustaining signal transmission. The selectivity of signal transmission is greatly enhanced by the variety of glutamate receptor types and their subunits (Brandstätter et al., 1998). Receptor expression is particularly effective in signal perception and transmission since it can differ not only between cell types but even within the same cell. The kind, distribution, quantity, and location of glutamate receptors within cells determine how the visual process develops at the cellular level (Ghosh et al., 2001). The Cyclic guanosine monophosphate (cGMP) gated ion channels in photoreceptors are the main mediator of the development of various signaling pathways (Molday & Moritz, 2015). cGMP gated ion channels allow sodium ions to enter the photoreceptors during glutamate release in the dark. However, under light conditions, photons cause conformational changes in opsins to activate G proteins called transducin. Activated G proteins initiate hydrolyzes of cGMPs via an enzyme called phosphodiesterase. Under the reduction of cGMP, sodium ion flow into cells decreases and this causes hyperpolarization of photoreceptors due to more negatively charged ions accumulation into the cytosol. In the meantime, this results in a decrease in glutamate release to synapses between bipolar cells and photoreceptors. Since phototransduction is a rapid and dynamic process, photoreceptors depolarize to return to their resting condition (Gill et al., 2019). This occurs when arrestin deactivates the rhodopsin protein. When rhodopsin is inactivated, it can no longer induce G-proteins to the breaking down of cGMPs. The level of cGMPs increases in cells and it induces sodium ion flux and glutamate release.

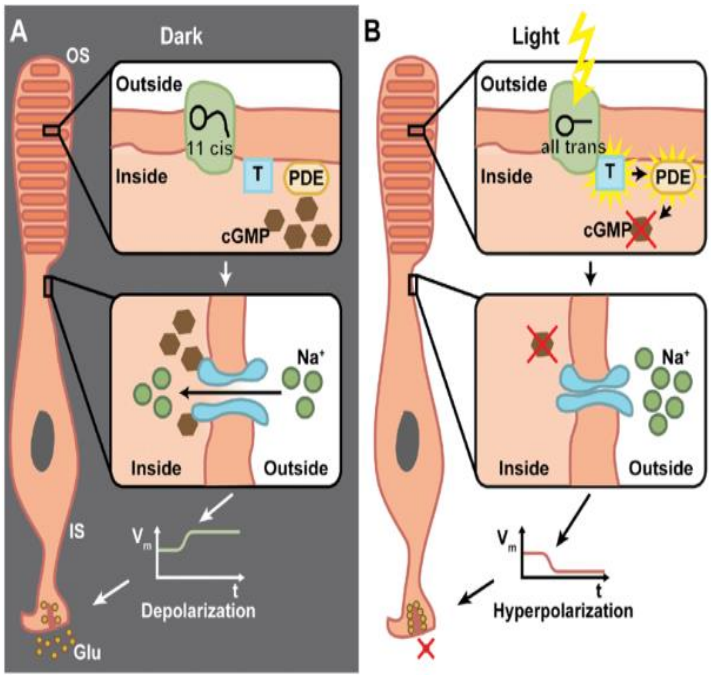

Figure 1.2 Illustration of phototransduction in photoreceptors. Adapted from (Klapper et al., 2016) .

Signal transmission from photoreceptors to ganglion cells with many synaptic connections is regulated by bipolar cells stimulated by phototransduction in photoreceptors. With varying synaptic connections that provide sign inversion or sign conservation, they can be either ON or OFF cells (Euler et al., 2014). These cells can quickly and efficiently interpret information about light levels by using ON and OFF signaling mechanisms. Bipolar cells (ON and OFF) response to glutamate in different ways due to their receptors (Ichinose & Habib, 2022). Decrease in glutamate at synapse region causes depolarization of ON bipolar cells to induce neurotransmitter release towards retina ganglion cells. Reduced glutamate causes ion channels to close and the membrane potential to become hyperpolarized in OFF bipolar cells, which prevents neurotransmitters released to synapses.

Each cellular event in retina creates a continuity of the process after the arrival of light until sending the messages by RGCs to brain. The final destination of electrical stimulus in retina is retina ganglion cells, stimulated by released neurotransmitters from bipolar cells. As in bipolar cells, RGCs have ON, OFF, and ON-OFF types

responding under dark and light conditions (Kim et al., 2021; Sanes & Masland, 2015). Under light, ON RGCs increase the action potential firings while OFF cells decrease their signaling. In contrast, in the dark, OFF RGCs exhibit an increase in action potential firings, while ON cells show a significant reduction in their activity. ON-OFF RGCs have special functions to get responses both under light and dark conditions. For action potential, the influx of sodium ions into the RGCs needs to reach a threshold level as other neuron cells. Voltage-gated ion channel activation is regulated by neurotransmitter release which triggers depolarization of membrane potential in RGC. When the depolarization approaches the threshold level, sodium ions are released through voltage gated ion channels, leading to fast firing (Kameneva et al., 2016). After firing rate, voltage gated potassium channels open and repolarization of cell membrane occurs which further allow RGCs to enter a resting state. Signals are transmitted to the brain via RGC axons. The axons exit the eye as nerve fibers through the optic disc and follow the path of the optic nerve. The optic disc is where the retinal nerve fibers come together to transmit visual signals, while the optic nerve is a tissue formation that can be described as a closed tunnel pathway protected by supporting cells. The majority of visual signals are first received by the brain's superior colliculus and lateral geniculate nucleus. For further visual perception, signals from these areas are integrated and transmitted to the visual cortex (Ichinose & Habib, 2022).

In the human eye, resolution of small details is affected by several elements, as they create the boundaries of visual perception. Neural information processing in the brain, the placement of photoreceptors on the fovea and peripheral sides of the retina, and the size of the eye's aperture are some of these variables (Cornsweet, 2012). For high resolution with good details, at cellular level, several chemical and electrical reactions need to happen which cause the production of impulses for transmitting to brain. Our ability to understand visual surroundings depends on the distribution of retina cells as well as brain's ability to interpret and process these signals. In retina, distribution of photoreceptors is responsible for high quality in vision.

Rod photoreceptors mainly exist in the peripheral regions of retina and could not detect fine color details, but they are well capable to distinguish brightness of view by their specialized photopigment, rhodopsin. The fovea at central retina offers significantly higher visual acuity (Provis et al., 2013). Fovea has an extremely high concentration of photoreceptor cells, primarily cones. There are approximately 200,000 cone cells packed into each mm^2 of retina. The distance between individual cone cells in the fovea is remarkably small, measuring merely 4-6 μm (Liu et al., 2018). The dense distribution of cone photoreceptors in the fovea provides high visual acuity that increase the ability seeing small details (Wells-Gray et al., 2016). Decrease in cone cells/mm^2 at periphery causes diminished visual acuity and color discrimination (Chui et al., 2008; Wells-Gray et al., 2016). And peripheral retina is more suited for detecting motion and changes in light levels rather than small details.

Fine detail vision is not just related to the density of cone photoreceptors at fovea, it is also occurred with a combination of connections of photoreceptors between interneurons to ganglion cells. Rod and cones have different synaptic connections at central and peripheral retina(Lamb, 2016). A rod cell can establish connections with more than one interneurons and this leads to gathering of processed signals coming from several rods in one retina ganglion cell. Therefore, RGC connected to diverse photoreceptors has responsibility to send several signals to the brain. Each cone cell at fovea region has certain connections to a number of horizontal or bipolar cells. This makes it possible to transmit messages with less alterations to the ganglion cells consequently demonstrates how the cellular level produces a perfect pixelated image. Retinal pathologies related with retinal cells degeneration or blockage in visual pathways from photoreceptors to RGCs cause disruption in vision.

1.2 Retinal Degeneration

Genetic variations in several genes involved in phototransduction in photoreceptors may cause the inherited disease known as retinal pigmentosa (RP) (Daiger et al., 2013). Some mutation in photoreceptors result in the retinal degeneration starting with cell death of rods followed by cones. Most distinguished changes in retina are unorganized retina layer morphology and shortened of photoreceptor outer segments.

The first symptom of the disease can be defined as the gradual weakening of night vision and the resulting narrowing of the night vision field. In people with RP, it is observed that they cannot see objects that people with normal vision can distinguish well in slightly dark environments. The disease starts at early ages with poor eyesight at peripheral vision and during late stages central vision is affected and the complete loss of vision occurs (Figure 1.3). Since retinitis pigmentosa is genetic disorder, there is not medical treatment to prevent disease. However, only for RPE65 gene therapy is under clinical testing with FDA approval (Russell et al., 2017) and other genetic variants that cause retinitis pigmentosa are still under investigation (Wu et al., 2023) as gene therapy and photovoltaic retinal prosthesis proposed for vision impairment (Wang et al., 2019).

Progressive vision loss affecting a patient's central vision is known as age-related macular degeneration (Figure 1.3). The disease is seen in elders and progression of vision loss depends on the type of the disease (Nowak, 2006). In the wet AMD, new blood vessels and blood leaks under the retina cause retinal damage so choroidal neovascularization causes subretinal hemorrhage and the disease progresses rapidly. Anti-vascularization agents as anti-VEGF drugs can delay the disease progression and they includes FDA approved treatment options that can control the progression of disease and enhance visual acuity (Mitchell et al., 2018). Anti-VEGF drugs to stop neovascularization are used in the clinic to diminish progression of wet AMD which is seen in 10% of diagnosed cases. The intraocular implant form designed to provide controlled drug release without the need for frequent injections. Although it is irreversible in patients with complete loss of their vision, the disease progression can be decreased at early stages with drug treatment. However, these treatments do not provide complete recovery of vision.

In dry AMD, there is an irreversible loss of vision due to the accumulation of cellular waste in RPE layer so the disease progresses with direct atrophy without neovascularization (Fleckenstein et al., 2018). Both RPE and photoreceptors are affected due to the amount of waste. The difference between the two diseases is the integration of new blood vessels under macula and leakage from these vessels due to

the excessive production of VEGF in wet AMD. In dry AMD, there is RPE and photoreceptor death due to accumulated cell waste. There is no treatment method to prevent this death, but retinal prostheses such as Prima (Pixium Vision) have been developed in clinical trials to perform the functions of photoreceptors (Palanker et al., 2020).

The common feature of diseases resulted in impairment in vision carried through retinal degeneration as retinitis pigmentosa, diabetic retinopathy, and AMD is alterations in photoreceptor cells, which have the greatest role in visual cycle and phototransduction pathways (Deng et al., 2022),(Chawla & Vohra, 2022). Nonfunctional photoreceptors induce permanent or irreversible vision deterioration depending on the progression of the disease. For years, interdisciplinary research groups from many different fields as an example of Ophthalmology, Molecular Biology, Electrical Engineering, Material Science and so on have been working together to find potential therapy on blindness. There are various strategies on restoration of vision as gene therapy (Acland et al., 2001; Bainbridge et al., 2008),(Böhm et al., 2020),(Hauswirth et al., 2008), cell therapy (Dalkara et al., 2016), optogenetic therapy (Jacobson et al., 2013) and retinal prosthesis (Chuang et al., 2014). Among all these approaches, retinal prosthesis is engineered to facilitate artificial vision as an alternative to photoreceptors function. These devices can partially restore the incomplete phototransduction that blocks visual signal transmission, and promote neuronal electrical stimulation.

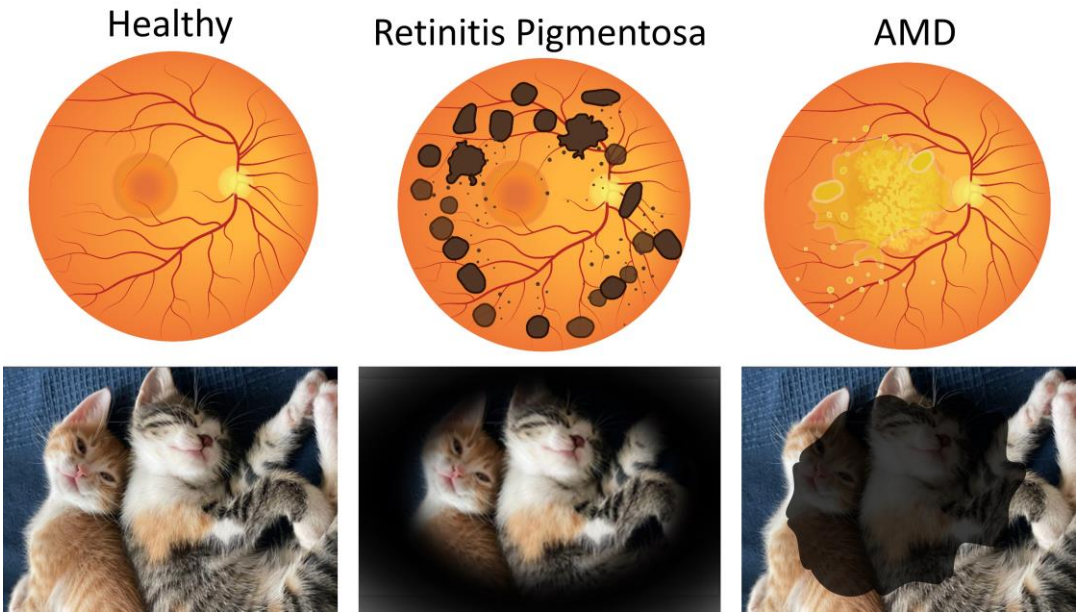

Figure 1.3 Comparison of healthy retina, retinitis pigmentosa and age related macula degenerated retina. Created with BioRender.

1.3 Visual Prosthesis

The history of visual prosthesis started in 1929 with curious neuroscientist Otfrid Foerster (Sarikcioglu, 2007). He performed electrocorticographic studies which include electrical stimulation of cortex under local anesthesia on his patients. During those experiments, some patients recognized the perception of light named as phosphene when visual cortex was stimulated without any light illumination on eyes (Oster, 1970). The development of visual prosthesis has accelerated since the emergence of the idea of using electrical stimuli (Ayton et al., 2020).

The first retinal prosthesis Argus I was introduced by Second Sight Medical Products in 2002 which was tested on six blind individuals. Four years later, the developed device Argus II was approved for clinical studies and after preclinical research, got FDA approval in 2013. Device was tested on 30 retinitis pigmentosa patients at different medical centers at Europe and US (Humayun et al., 2012). The system has an external camera system and implanted electrode array with its components to be placed in eye (Arevalo et al., 2021). Argus system works by converting photons taken

by external camera on glasses into electrical signals via visual processing unit. This unit sends electrical signals to stimulate prosthesis in the retina and to achieve visual sensation. To date, over 350 patients have had implants to restore their ability to see, identify the size and motion of objects, read letters, and perform other essential daily tasks (da Cruz et al., 2016). In the last 20 years, Alpha-IMS and Alpha-AMS subretinal prosthesis developed by Retina Implant AG (Kitiratschky et al., 2015),(Stingl et al., 2015),(Edwards et al., 2018), suprachoroidal retinal prosthesis (Ayton et al., 2014), PRIMA subretinal system (Lemoine et al., 2020),(Palanker et al., 2022) and the IRIS®II epiretinal system (Hornig et al., 2017) developed by Pixium Vision, EPIRET3 system (Roessler et al., 2009),(Menzel-Severing et al., 2012), suprachoroidal–transretinal stimulation prosthesis, and cortical implants were developed for vision restoration (Chuang et al., 2014) (Table 1).

Since every retinal prosthesis have different fabrication and design, the most important features are sizes, pixel resolution and the implantation area in the retina. There are distinguished differences in the structure and functionality of visual implants based on their implantation site. To date, epiretinal, subretinal, suprachoroidal, and cortical implants have been developed and tested in clinical trials. Each implantation approaches offer specific benefits as well as limitations (Shaheen et al., 2024). For instance, suprachoroidal devices are associated with lower risks compared to subretinal and epiretinal implants, as they avoid direct contact with the retinal neurons. Nevertheless, the resolution achieved by suprachoroidal devices is generally less than other implantation areas due to its distance from retinal ganglion cells and secondary neurons.

While epiretinal prosthesis have less surgical challenges and operation side effects than subretinal implants, they require an external camera sources to conduct light processing into electrical pulses. On the other hand, subretinal devices have more chance to stimulate visual processing owing to connection between both inner and outer layers of retina, however risks in surgical operation are higher including two main side effects, inflammation and rejection of implantation.

Implants placed in the visual cortex aim for a different approach. In this application, blindness that develops due to damage in the brain rather than light perception and stimulation pathways in the retina is aimed to create phosphene, defined as instantaneous light beams. In these approach, the implant's placement location, the size of area, and prosthesis material are quite important. A fully developed and healthy visual network is required, therefore, its suitability for individuals who are blind from birth has not yet been developed. In addition, there are severe complications such as infection, inflammation and neurodegeneration that may arise after the surgical operation (Liu et al., 2022).

Another approach is to target visual stimulation by stimulating the optic nerve located between the retina and the visual cortex (Sakaguchi et al., 2009; Veraart et al., 2003). Instead of implantation at the more sensitive structure of the retina, the optic nerve is targeted to repair vision loss caused by optic nerve damage and to generate phosphene in the visual center with electrodes wrapped around it (Kim et al., 2025; Paknahad et al., 2022). In recent animal studies, stimulation of the visual cortex with different types of electrodes placed in the optic nerve region has been investigated with aiming to classify incoming visual responses at specific visual region on the brain (Borda et al., 2022; Gaillet et al., 2021)

In order to restore light perception and increase electrical stimulation of neurons, numerous research teams have been focusing on stimulation with retinal prosthesis. The major handicaps of retinal prosthesis are biocompatibility problems after implantation and visual acuity limitations. Newly established neural interfaces focus on overcoming those challenges with using next-generation quantum dot based biointerfaces to ensure safe stimulation with high resolution. Quantum dot-based biointerfaces provide neuron stimulation by converting light into electrical signals in retina from outer to inner layers.

Table 1.1. Clinical Trials

Device Name	Company	Type of Disease	Year	Number of Pixel	Implant material and size	Ref
Epiretinal Device						
Argus I	Second Sight	retinitis pigmentosa (RP)	2002	16	Platinum electrodes	(Humayun et al., 2003)
EpiRet3	RWTH Aachen	retinitis pigmentosa (RP)	2006	25	Hexagonal iridium oxide electrodes, diameter with 100 µm and thickness with 25 µm	(Roessler et al., 2009)
Argus II	Second Sight	retinitis pigmentosa (RP)	2011 (CE), 2013 (FDA)	60 electrodes	Platinum electrodes (200 µm diameter)	(Humayun et al., 2012)
PRIMA	Pixium Vision	age-related macular degeneration (AMD)	2017	378 (Mikro-fotodiyot)	2x2mm size, 100 µm electrode diameter 30µm in height	(Palanker et al., 2020)
Subretinal Device						
Alpha IMS	Retina Implant AG	retinitis pigmentosa (RP)	2013 (CE)	1500 photodiodes	50 × 50 µm titanium nitride electrode	(Stingl et al., 2015)
Alpha AMS	Retina Implant AG	retinitis pigmentosa (RP)	2016	1,600 microphotodiodes	70 × 70 µm titanium nitride electrode	(Stingl et al., 2017)
IRIS II	Pixium Vision	retinitis pigmentosa (RP)	2016	150 electrode	-	(Muqit et al., 2019)
Artificial Silicon Retina (ASR)	Optobionics Corporation	retinitis pigmentosa, age related macular degeneration (AMD)	2004	5000 micro-photodiodes	2mm diameter silicone semiconductor array 20×20 µm square pixel with 9×9 µm IrO_2	(Chow et al., 2004)
Tübingen retina implant	Retina Implant AG (Germany)	retinitis pigmentosa (RP)	2011	16 TiN electrode	First generation 50 × 50 µm Second-generation 100 × 100 µm	(Wilke et al., 2011)
Cortical Device						
Dobelle Eye	Dobelle Institute	Variable diagnosis	1970	-	0-5 to 2-0 mm platinum iridium electrode	(Dobelle, 2000)
Orion	Second Sight	Variable diagnosis	2018	60 platinum electrode	-	(Caspi et al., 2021)
Suprachoroidal Device						
Gen 2 Suprachoroidal Device	Bionic Vision Technologies	retinitis pigmentosa (RP)	2018	44 platinum electrode	19 × 8 mm	(Petoe et al., 2025)
Gen 1 Suprachoroidal Device	Bionic Vision Australia	retinitis pigmentosa (RP)	2012	33 platinum electrode	19 mm long - 8 mm wide 30 × 600 mm & 3 × 400 mm diameter	(Ayton et al., 2014)
Suprachoroidal Transretinal Stimulation Device	Osaka University	retinitis pigmentosa (RP)	2009	49 platinum electrode	5.7 × 4.6 mm	(Fujikado et al., 2011)

1.4 Hypothesis and Aims

In the PhD thesis project, new types of optoelectronic devices, based on a semiconductor organic polymers, quantum dots and nanocrystals, were aimed to investigate in *in vitro* cell culture followed by *ex vivo* retina stimulation.

1.4.1. Aim 1 In vitro biocompatibility of devices

The first aim is examination of neurons in terms of viability, expression of characteristic markers and morphological alterations when growing on photovoltaic devices. After isolation from hippocampus, primary neurons were cultured on control ITO and different types of biointerfaces. Biosafety of each biointerface was checked on Day 0 and Day 14 of the culture by controlling neural specific biomarkers through immunofluorescence staining. Specifically, the characteristic features of neurons were analyzed with neural lineage markers and their morphology was checked with cytoskeleton staining.

1.4.2. Aim 2 Recording of intracellular stress level under repetitive light illumination

To examine whether the electrical signals produced by light illumination on the device surface trigger the stress mechanism in cells, 2',7'-dichlorodihydrofluorescein diacetate (H_2DFCDA) staining was performed for visualization of intracellular oxidative stress level. Second strategy is to examine the mitochondria's health, as they are responsible for the cell’s energy mechanism. To visualize healthy and disrupted mitochondria after light illumination, JC-1 staining as a fluorescent indicator of mitochondrial membrane potential was performed.

1.4.3. Aim 3 In vitro biointerface activation

To measure neural dynamics and physiological activity of single neurons, intracellular calcium flow was recorded upon stimulation. In order to show calcium signaling, cells were stained with Flou-4AM and calcium influx was recorded before and after photostimulation under time-lapse fluorescence microscopy.

1.4.4. Aim 4 Ex vivo retina tissue isolation, optimization and recording

Retina tissues was isolated from rats. Since optimum culture condition for retina tissue is critical for getting good electrophysiology recordings; isolation timing, perfusion and experiment temperature was optimized on rats having vision. Then P23H retina degenerated rats were used to assess RGC activation under light illumination with biointerface.

1.4.5. Aim 5 In vivo optic nerve injury model optimization

The last part of thesis aimed to generate optic nerve crush model on rats with vision. Degree of vision loss in animals was measured through electroretinography and visual evoked potential recordings and the degree of retinal damage and gliosis on tissue level was analyzed through immunofluorescence staining of retina cell specific biomarkers.

2. CHAPTER 2

MATERIALS and METHODS

2.1 Materials

All the materials used in experiments, chemicals, kits and custom made solutions were indicated at Appendix A.

2.2 Biointerface Fabrication and Characterization

2.2.1 Fabrication of P3HT:ITIC Biointerface

The indium thin oxide (ITO) glasses were prepared with initial cleaning through sonication in Hellmanex II reagent following by incubation in nanopure H_2O, acetone and isopropanol respectively for 15 min. Prepared ITO glasses then dried in 50°C oven. After that, ultraviolet (UV) ozone treatment was carried out prior initiating layered structure fabrication. 40 nm zinc oxide (ZnO) layer on ITO was coated using the sol-gel method. To crystallize the film, 30 min of annealing at 150°C were applied on ZnO sol-gel materials. For active layer, the binary mixture of polymer P3HT: ITIC was prepared and spin coated on ZnO layer at 2000 rpm. After active layer coating, the photoactive P3HT:ITIC layer was obtained by annealing the thin film layer at 160 ^{o}C for 10 minutes. By testing different P3HT and ITIC solution concentrations and P3HT:ITIC mixing ratios, the concentrations and mixing ratio that give the highest photocurrent was determined. For characterization of different P3HT:ITIC solution, the optical absorption and radiation spectrum of the photoactive P3HT:ITIC structure was measured with the FS5 Spectrometer (Edinburgh Instruments).

2.2.2 Fabrication of Quantum Dots or Nanocrystal based Photovoltaic Biointerfaces

Photovoltaic devices were fabricated on glass ITO substrates after Hellmanex II and alcohol rinsing and UV ozone sterilization processes. For the ITO/ZnO/$AgBiS_2$/P3HT biointerface fabrication, ZnO was annealed onto 2/3 of the total ITO glass area, and $AgBiS_2$ nanocrystals (NCs) were spin-coated as the active layer. Photoactive P3HT layer was coated onto the Silver bismuth sulfide ($AgBiS_2$) layer to complete ITO/ZnO/$AgBiS_2$/P3HT biointerface (Balamur et al., 2024). Lastly return electrode was prepared by ruthenium oxide (RuO_2) coating onto remaining 1/3 area of the total ITO glass. For ITO/ZnO nanowire (NW)/$AgBiS_2$ NCs biointerface fabrication, ZnO NW were grown on coated ZnO layer. $AgBiS_2$ NCs were coated on ZnO NWs. For ITO/ZnO NW/$AgBiS_2$/P3HT biointerface design, P3HT photoactive part was coated on $AgBiS_2$ NC while RuO_2 return electrode was coated onto remaining 1/3 of the ITO glass area.

2.2.3 Characterization of Biointerfaces

Chronoamperometry and chronopotentiometry recordings were measured for electrochemical characteristics of devices. Photocurrent density and photovoltage measurements of the photovoltaic devices were taken with a three-electrode electrochemical measurement system. After the devices fabrication, they were placed in the artificial cerebrospinal fluid (aCSF), photocurrent and photovoltage measurements were recorded under repetitive light illumination by adjusting the ITO as working electrode, the counter electrode in the platinum rod medium, and Ag/AgCl reference electrode as reference electrode in the medium. In order to excite the devices, pulses given through Thorlabs M780LP1 or M880LP1 LED controlled by Thorlabs DC2200 LED Driver.

2.3 Cell Culture

2.3.1 Animal Ethics

All animal experiments were conducted in compliance with the relevant guidelines and were approved by the Animal Ethics Committee of the Institutional Animal Care and Use of Koç University with protocol numbers for Wistar Albino rat embryos Approval No: 2021.HADYEK.017 and 2021.HADYEK.022; for Dark Agouti, P23H adult rats 2022.HADYEK.043 with respect to Directive 2010/63/EU of the European Parliament and of the Council on the Protection of Animals Used for Scientific Purposes and the Republic of Turkey 5199 Animal Protection Law, Article 9 and 17.

2.3.2 SH-SY5Y Neuroblastoma and Müller Glia Culture

Complete Dulbecco's Modified Eagle's Medium (DMEM), with 10% fetal bovine serum (FBS), % L-glutamine, and 1% penicillin-streptomycin (pen/strept) was used to maintain SH-SY5Y neuroblastoma and immortalized human retinal Müller glia (Mio-M1) cells cells at 37 °C in a culture incubator with 5% CO_2. Cells were passaged by removing them from the surface with trypsin-EDTA when they reached 80-90% confluency to ensure the continuity of the experiments.

2.3.3 Primary Neuron Isolation and Culture

Wistar Albino rats at the embryonic day of 16-18 were included in primary hippocampal neuron and cortical astrocyte isolation procedures shown at Figure 2.1. After being dissected, the hippocampal regions were transferred in falcon tube including Hank’s Balanced Salt Solution (HBSS) on ice box. Specimens were treated in Trypsin-EDTA solution (0.25%) including DNase-I (2%) for 20 min to induce enzymatic disruption. After incubation, excess enzyme activity was stopped with DMEM-F12 cell medium. Then suspension was centrifuged for three minutes at 300g. In order to resuspend tissue pellet, fresh Neurobasal Medium (NBM) including 2mM β-mercaptoethanol, 20mM L-glutamine, L-glutamate, B27, and pen/strept were added. Cells were cultured with devices pre-coated with Poly-L-Lysine (PLL) as 500,000 cells/well in 6 well plates after being passed over a 70 μm cell separator. Cells were

cultured for three days. After complete cell attachment reach in 3 days, fresh NBM including AraC solution were provided to eliminate glia cell population. After one-day incubation, fresh NBM was provided and the morphological development of the cells was observed with a light microscope. Cells were cultured for biocompatibility, characterization and electrophysiology experiments (Balamur et al., 2024), (Han, Yildiz, et al., 2022),(Karatum, Kaleli, et al., 2022b),(Karatum, Yildiz, et al., 2022a). To ensure that cells had enough nutrients before experiments, half of the media was replaced every three days.

2.3.4 Primary Astrocyte Culture Condition

Primary astrocyte isolation procedure was performed with modification of Güler et al.'s star protocols (Güler et al., 2021). Obtaining homogeneous astrocyte cell culture took 3 weeks, and their morphological and characteristic features were checked before culturing with the devices. After the isolation of hippocampi from embryonic rats described above, the remaining cortex tissues are placed in cold HBSS transport solution The tissues were incubated in Trypsin-EDTA (0.25%) including DNase-I (2%) and mixed by serological pipette several times and incubate 20-25 minutes at water bath. Centrifugation of cells was applied then pellet was resuspended with complete DMEM. The cells were cultured in 15 cm culture plates. The medium was replaced on the 1st, 2nd and 7th day of culture. On the 14th day of the culture, the cells that are completely confluent were subjected to a separate process to remove oligodendrocytes in the medium. After aspirating the supernatant, the cells underwent two rounds of washing with PBS. During the washing process, the culture dishes were gently shaken from the side; this process should not be done too harsh so that the astrocytes do not detach from the surface. Then, the cells were incubated in an incubator with 0.05% Trypsin-EDTA enzyme for 4 min. Then, enzyme activation was inactivated with complete DMEM. Cell suspension was centrifuged for 6 minutes at 200 rcf. Complete medium was added to dissolve pellet to seed into T75 cell flasks as 500000 cells/flask. Until confluency was achieved, the cell media was replaced every three days. Characterization and biocompatibility tests were conducted using confluent cells.

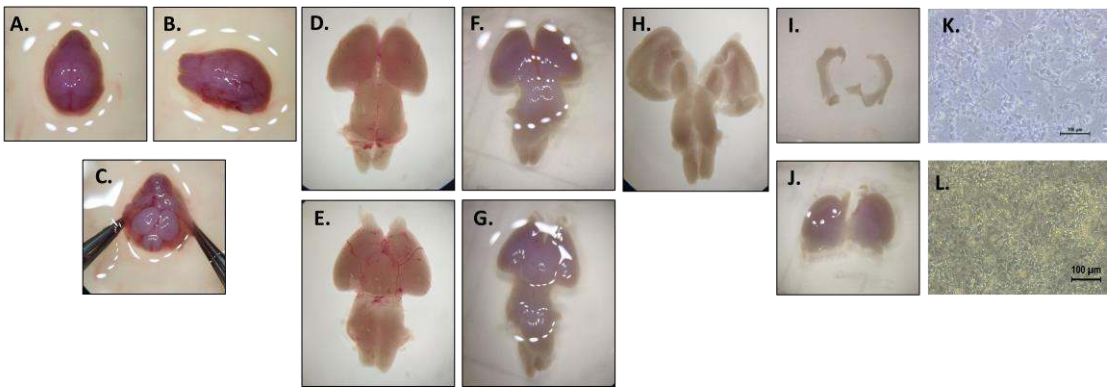

Figure 2.1 Demonstration of hippocampal and cortical tissue isolation from emryonic rat. A. Top and B. side views of the fetus after decapitation. C. Cutting the skull along the midline using fine-tipped forceps. D. Top and E. bottom views of the dissected brain. F. Superior and G. inferior views of the brain separated from its meninges. H. The area of hippocampus is visible after separating the right and left cortex in the middle. I. Post-dissection view of the crescent-shaped hippocampus. J. Cortex isolation after hippocampal dissection from the right and left cerebral hemispheres. K. Light microscope image of the primary neuron culture obtained from the hippocampus. L. Light microscope image of primary astrocyte and glia culture obtained from the cortex.

2.3.5 Preparation of Substrates for Cell Culture

For cell culture experiments, sterilization procedures were performed on biointerfaces. Firstly, to break hydrophobicity of substrates, they were incubated in nanopure H_2O for 24 hours to and then rinsed in 70% of ethanol solution. After rinsing, they were allowed for air dry. Biointerfaces were nailed to the surface of 6-well cell culture plates. After 30 minutes of room temperature UV sterilization, PLL or PDL solution was put on the substrates and allowed overnight at 37°C in an incubation.

2.4 *In Vitro* Biocompatibility Tests

After culture period of cells on fabricated biointerfaces, cell viability, ROS generation, mitochondrial membrane potential and calcium influx experiments were performed (Figure 2.2).

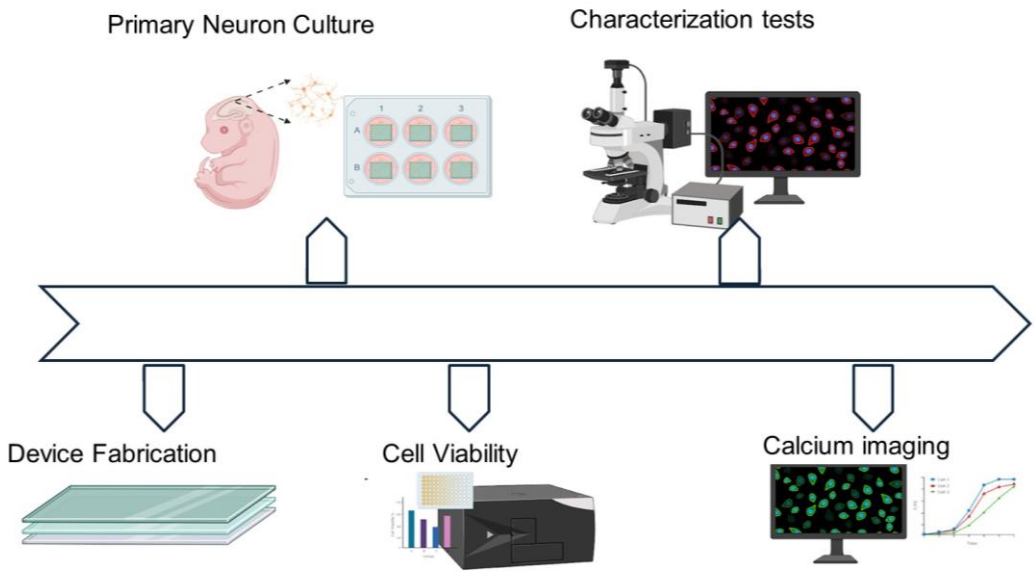

Figure 2.2 *In vitro* experimental procedure. Created with BioRender.

2.4.1 CTG Cell Viability Assays

The CellTiter-Glo vitality Assay (CTG, Promega, Mannheim, Germany) was used to assess the vitality of cells grown on control ITO and biointerface devices. Substrates were put in culture wells and stayed in PLL solution overnight after sterilization procedure. On PLL-coated devices, isolated primary hippocampus neurons and astrocytes were cultured as 500000 cells/well, Müller glia cells as 300000 cells/well, and SH-SY5Y neuroblastoma as 300000 cells per well. At room temperature, CTG solution was added on cells and allowed for ten minutes. The SynergyH1 Microplate Reader (BioTek Instruments) was used to record the luminescence signals after the solution was moved to a 96-well opaque plate. Each sample's relative viability was calculated as below: Alive cells equal to the sample's relative luminescence unit

(RLU) divided by the control's RLU × 100. The cells cultivated on the biointerface device provided the sample's luminescence signals (RLU), whereas cells cultivated on the ITO substrates provided the control's RLU.

2.4.2 Lactate-dehydrogenase (LDH) Release Assay

Enzyme release capacity of the cells due to breaking of membrane integrity was investigated using the LDH Cytotoxicity Assay for the lactate dehydrogenase enzyme release according to manufacturer's instructions. Briefly, control and experimental groups were treated with medium including Triton-X-100 (1%) for 10 min. at 37°C in culture incubator to cause cell membrane disruption as a positive control of the experiment. After 10 minutes of incubation with the medium containing 1% water for all experimental and control groups, 90 µL of media was combined with 10 µL test reagent and incubated for 30 min. at 37°C into an incubator for starting the reaction sufficiently. The SynergyH1 Microplate Reader (BioTek Instruments) was used to read at 450 nm.

2.4.3 MTT Cytotoxicity Test

Complete NBM containing 5 mg/ml of MTT was given to cells on day 0 and incubated for 4h in an incubator. Following incubation, devices were transferred to new plate, where they were incubated for 10 minutes with DMSO for dissolving formazan salts. Each well's solution was then moved to 96well plate to read at 570 nm at SynergyH1 Microplate Reader. Viability = (ODsample/ODcontrol) × 100 was the formula used to determine the relative cell viability of each substrate while normalizing the control ITO.

2.4.4 Live/Death assay with calcein AM and Propidium Iodide (PI)

After HBSS 1X washes, neurons were treated with 2 µM calcein AM working solution made in HBSS 1X and incubated for 10 min. After removing dye solution, PI solution made in HBSS 1X was added and incubated 30 min then washed with HBSS

1X. A confocal laser scanning microscope was used to detect fluorescence signals (Leica DMI8 SP8).

2.4.5 Immunofluorescence Staining and Imaging

As previously mentioned, ITO control and the biointerface were used to seed primary hippocampus neurons, astrocytes, and Mio-M1. The primary hippocampus neurons and astrocytes were treated with 4% paraformaldehyde for 20 minutes in a fume hood after Day 0 (DIV5) or Day 14 (DIV19). They were then rinsed in PBS with Tween-20 0.1%. Then samples were stayed for 8 minutes in Triton X-100 (0.1%) cell membrane permeabilization. Blocking was done for ten minutes at room temperature using Superblock. Primary astrocytes were treated with anti-glial fibrillary acidic protein (GFAP); Müller cells were cultured with anti-glutamine synthetase (GS) for an entire night at cold; and samples containing primary hippocampus neurons were incubated with anti-NeuN and anti-β-III tubulin. Following incubation, PBS-T was used three times to wash the cells. For fluorophore marking on the primary antibody, samples were then treated for 90 min with Alexa Fluor 488, 555, or 594 (Invitrogen) at 37°C. FITC-conjugated phalloidin antibody was also applied to neurons at 37°C for 90 min. in order to see the cytoskeleton. After three PBS-T washes, each sample was mounted using a mounting solution mixed with DAPI to view the cell nucleus and observed under a fluorescent light microscope (Axio Observer Z1) (Han, Yildiz, et al., 2022),(Karatum, Kaleli, et al., 2022b),(Karatum, Yildiz, et al., 2022a).

2.4.6 The cell number/mm^2 counting

Amount of neurons and total cells/unit area were determined by analyzing NeuN and DAPI stained cells. 10X objective images were used for the counting, the image size is 0.713 mm by 1.13 mm with an area of 0.805 mm^2. NeuN positive cells per area (neuron counts/mm^2) was counted for neuron cells and DAPI positive cells per area (neuron counts/mm^2) was counted for all cells in ImageJ (Balamur et al., 2024).

2.4.7 Neurite Length Measurement

Neurite length analysis was performed by anti-β-III Tubulin staining using NeuronJ plugin program in ImageJ. The length of neurite was measured by manually tracing a neurite from the boundary of the soma to the end of neurite. The average of 50 cells from each group were used in calculation (Balamur et al., 2024).

2.5 Intracellular ROS Assay

Oxidative stress was evaluated by intracellular ROS assay kit 2',7'-dichlorodihydrofluorescein diacetate (H_2DCFDA)(Kocyigit et al., 2019). On a control and device, 500000 primary hippocampus neurons were sown per well, and they were cultivated until DIV19. Experimental groups are ITO control, device before and after illumination, and a positive control incubated with 100 µM H_2O_2 for 30 min. Prior to imaging, neurons were first treated with 20µM H_2DCFDA for 45 min. The nucleus was stained with Hoechst (0.6 mg/ml) for 15 min before imaging. To stabilize the signals, cells were treated with a live cell solution for 10 min at room temperature then rinsed with PBS to visualize with time lapse fluorescence microscope (Axio Observer). Zen Blue 3.5 software was used to calculate the average fluorescence intensity. A light stimulation group was created using a 780 nm LED exposed to 10000 cycles, 1.5 $mW.mm^{-2}$ light intensity, 5 Hz, and 20 ms ON. When comparing relative fluorescence intensity, the ITO control's fluorescence intensity is accepted as 100% (Karatum, Yildiz, et al., 2022b).

2.6 Mitochondrial Membrane Potential (MMP) Examination

By guidelines provided by the manufacturer, the JC-1 Assay was perform to check the MMP. In short, 500000 cells/well of primary hippocampus neurons were sown onto the control and device, and they were cultivated for five to seven days. After staining the cells with 1 µM JC-1 in live cell solution at 37 °C, they were left for 30 minutes in the dark. JC-1 fluorescence was then viewed using a confocal laser microscopy (DMI8

SP8) after they had been cleaned twice with PBS to get rid of extra dye. For 20–40 seconds, cells were exposed to 780 nm light with a stimulation at 5 Hz with 20 ms ON time, and 1.5 $mW.mm^{-2}$ light intensity. Mean florescence intensity of green JC-1 monomers and red JC-1 aggregates was quantified and processed using LASX software (Leica, Germany).

2.7 Recording of *in vitro* Neural Responses with Calcium Imaging

Primary hippocampal neurons cultured on devices until DIV 10 then were treated with 1 µM Fluo-4 AM Invitrogen) and same amount of Pluronic-127 in neurobasal medium for 40 minutes at culture incubator. They were rinsed twice in PBS after incubation and treated with a neurobasal medium for 15 min at RT to stabilize the signals. Time-lapse recordings were taken with an inverted fluorescence microscopy (Axio Observer Z1) and confocal laser microscopy (DMI8 SP8). To avoid photobleaching, staining experiment and visualization procedure were performed under the dark condition. After establishing a baseline signal, 780 nm NIR light illumination was applied for 2 sec or 10 sec (Thorlabs M780LP1 LED driven with Thorlabs DC2200 LED Driver) and 180 sec recording was performed. Changes in the fluorescence intensity of each neuron over time were measured by selecting somas of neurons by Zen Blue and LASX software's. Normalization of fluorescence intensity was performed by dividinf Ft to baseline F0.

2.8 *Ex Vivo* Retina Tissue Preparation and Multielectrode Array (MEA) recordings

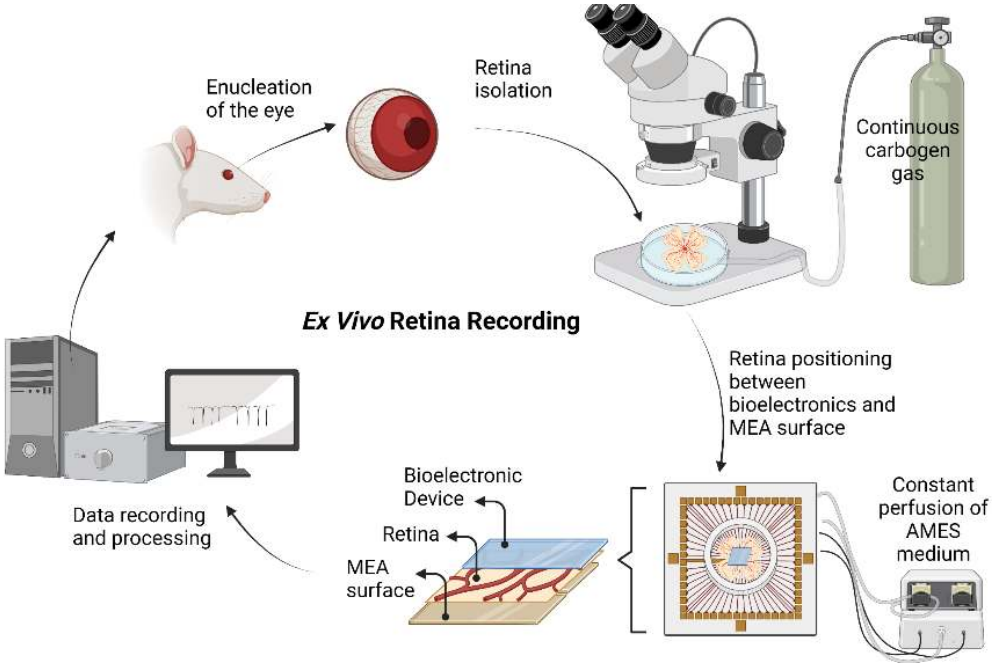

Figure 2.3 Schematic representation of *ex vivo* retina recording with MEA system. Created with BioRender.

2.8.1 Retina Preparation for Recording

Euthanasia and isolation of eyes:

8-month old Dark agouti rats were used for optimization experiments. Euthanasia was performed under carbon dioxide followed by cervical dislocation. The eyes were isolated under dim red light by cutting the eyelids, conjunctiva, optic nerve and removing excess muscle and connective tissues with ophthalmic scissors in oxygenated Ames media.

Retina isolation:

Ames medium was refreshed with fresh oxygenated Ames medium and retina isolation was performed under a stereomicroscope with dim red light. The eyeballs opened at the Rim side of the cornea and corneas were removed from the eyeballs by

cutting from the corneoscleral junctions. Then lens, vitreous body, and iris were dissected without touching retina (Figure 2.4 A-B). In order to get better contact of the retina ganglion cells on multi electrode array (MEA) surface removing of vitreous body is critical in this procedure. The optic nerve ending was cut from sclera and retina was dissected from subretinal space and released into plate.

Retina on MEA:

Retina was cut into two pieces. One piece remained in Ames medium until use and one was positioned on the membrane ring, which was prepared with PLL solution the night before. The Photoreceptor's side was touching the membrane while retinal ganglion cells were upwards (Figure 2.4 C, D). Ring was placed on MEA electrodes as RGCs facing the electrodes. The perfusion system was opened and flow of oxygenated Ames medium (32 °C) was adjusted to 3 ml/min. The temperature controller was adjusted to 32 °C for stage and perfusion inlet cannula.

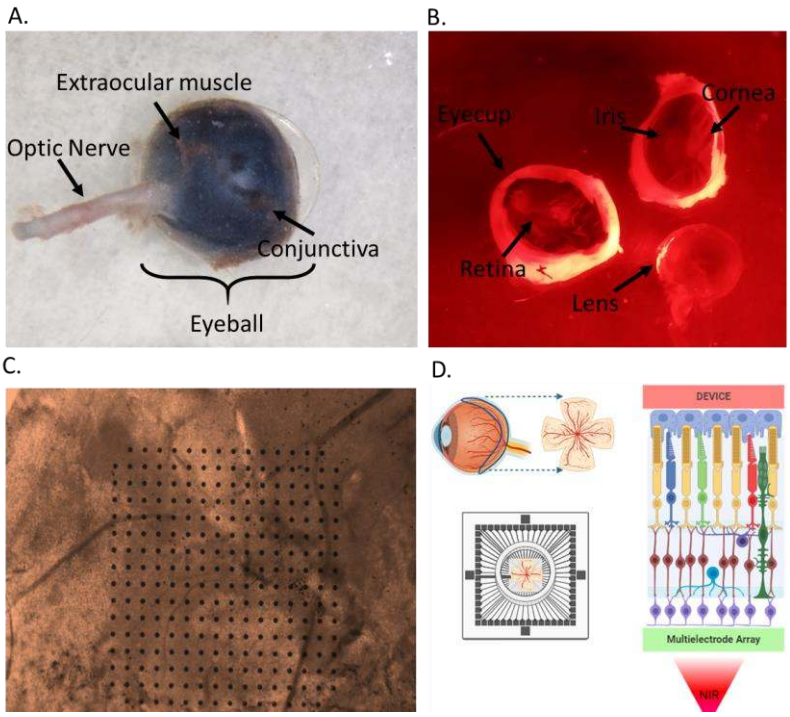

Figure 2.4 Retina isolation from eyeball. The enucleated eyeball (A) was opened at the Cornea was seperated from the eyeball by cutting from corneoscleral junctions to isolate the retina (B). Isolated retina was placed on microelectrode array for recording (C). Schematic representation of retina on microelectrode array (D). The photovoltaic bionterface is placed toward the outer retina while retina ganglion cells are in contact

with the microelectrode array. Illumination is given at the bottom of transparent MEA through microscope objectives.

2.8.2 Recording of Action Potential Ability with MEA

Ex vivo ERG recordings were conducted using MEA2100 setup (Figure 2.5) and Multi Channel Experimenter software (MCS) by manufacturer's instructions (GmbH, 2013). Retina was preserved in Ames solution to maintain optimum conditions during experiment. The solution temperature was maintained at between 32-35°C with temperature controller. A peristaltic perfusion system was used for long-term recordings. The flow rate of inlet and outlet solution was optimized for the recordings and adjusted to 3 ml/min. Recordings of neural activity was analyzed from individual cells using Multi Channel Analyzer software.

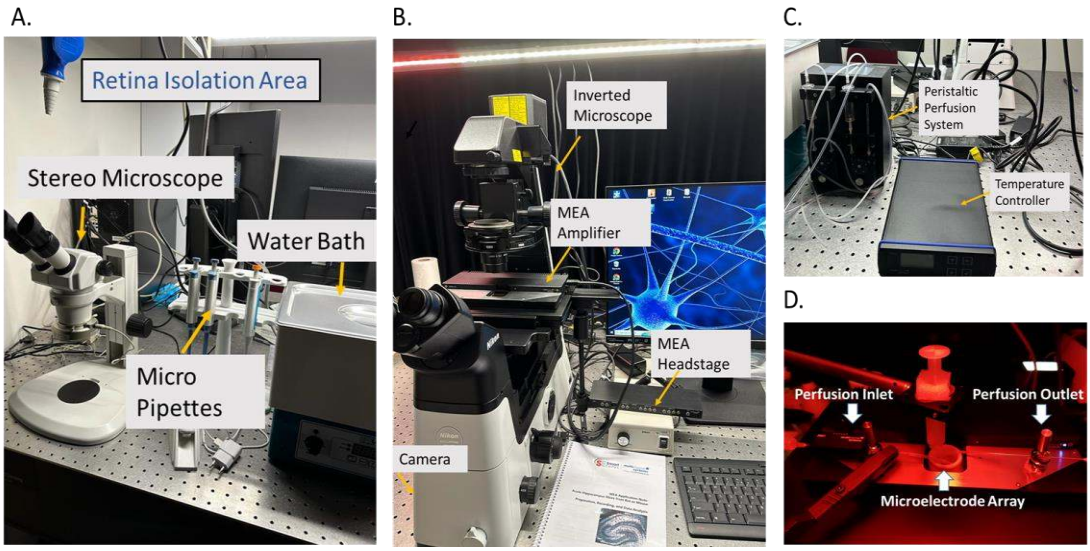

Figure 2.5 MEA system compartments and retina placement representation A. Combined MEA amplifier system with the inverted light microscope. B. Retina isolation unit. C. Perfusion and temperature controller unit. D. Perfusion inlet and outlet on MEA chamber.

2.9 Optimization of *In vivo* Optic Nerve Crush (ONC) Model

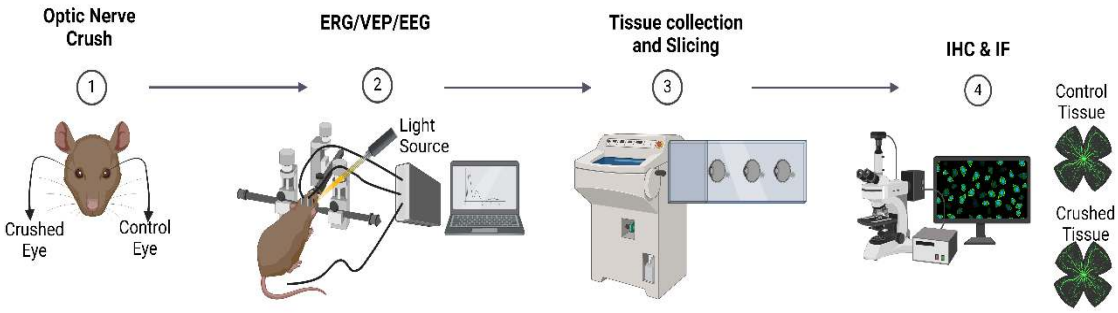

Figure 2.6 Experimental flow of optic nerve crush and histological analysis.

In the current study, we examine how the retinal structure and function were affected by different duration of optic nerve compression in adult Dark Agouti rats (4-8 mo).

The animals were split up into four groups for experiments;

- Control Group (n=4)
- 15 second ONC Group (n=4)
- 30 second ONC Group (n=4)
- 120 second ONC Group (n=2)

To get to the area, a lateral canthotomy and a lateral bulbar conjunctiva incision were made. With the aid of calibrated forceps, the optic nerve was held 2-3 mm posterior to the globe and crushed for 15 seconds, 30 seconds, and 120 seconds.

2.9.1 Establishment of optic nerve damage model in rats

General anesthesia induced in rats with intraperitoneal xylazine (10 mg/kg) and ketamine (75 mg/kg) and by assessing the paw pinch and tail reflexes anesthesia depth confirmed. Body temperature was regulated during the procedure by heat pad. The surgical procedure was performed on the right eye of the animals. For optic nerve damage, lateral canthotomy and lateral bulbar conjunctiva incision was applied, the lateral rectus muscle was excluded and retrobulbar area was found. In ONC model, compression was applied 2-3mm posterior to the globe with the help of calibrated

forceps on the intraorbital part of the optic nerve without any incision (Figure 2.7 and 2.8). No negative effects were expected to affect the integrity of the dura after the compression procedure.

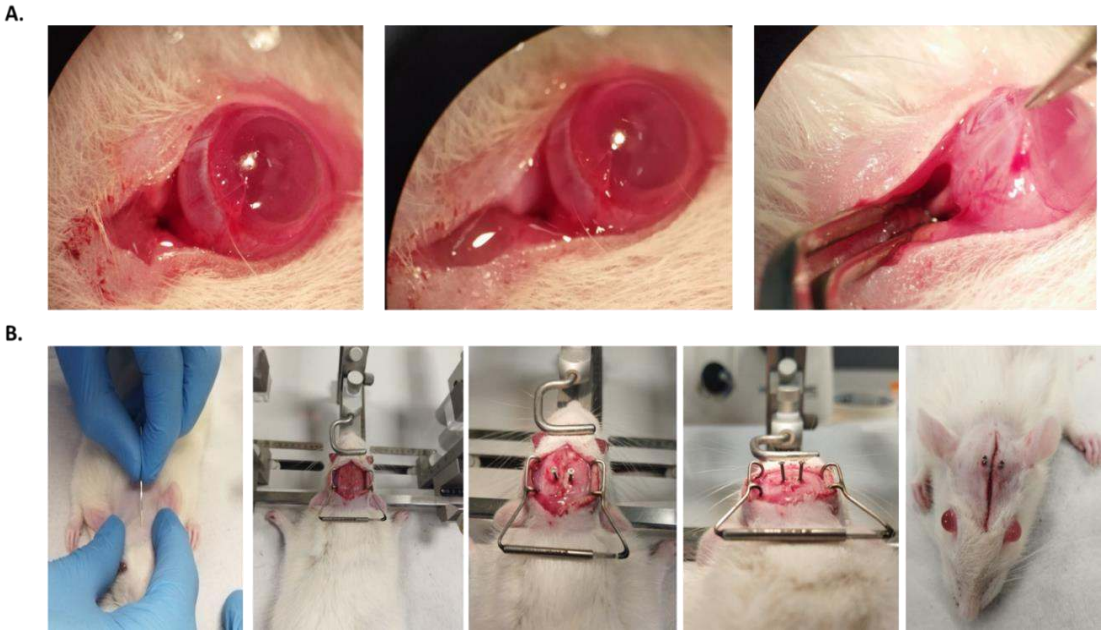

Figure 2.7 Preliminary testing of A . optic nerve operation on a Wistar Albino rat that is not included in the main experimental group, followed by B. VEP-EEG electrode implantation.

2.9.2 Electrode implantation on the skull for Visual Evoked Potential (VEP) Electroencephalography (EEG) Recordings

The rats were anesthetized and anesthesia depth confirmed by assessing the paw pinch and tail reflexes. Visual cortex's location in the rat brain was identified using the stereotaxic brain atlas (Paxinos & Watson, 2006). Permanent screw electrodes were selected for placement in the central area of the V1 region. Animal's scalp was shaved, and Betadine was applied on the surgical site. A longitudinal incision was made on the midline (Figure 2.8 B) and animal was placed at stereotaxic frame. The drilled areas were determined according to brain atlas and measured 3mm lateral to the midline, 7mm posterior from the bregma (Nguyen et al., 2016). The screw electrodes were implanted into the skull with two rotations (Figure 2.8 B, 2.9 C). The

surgical site was closed using Takilon solution and surgical sutures were applied to the skull skin.

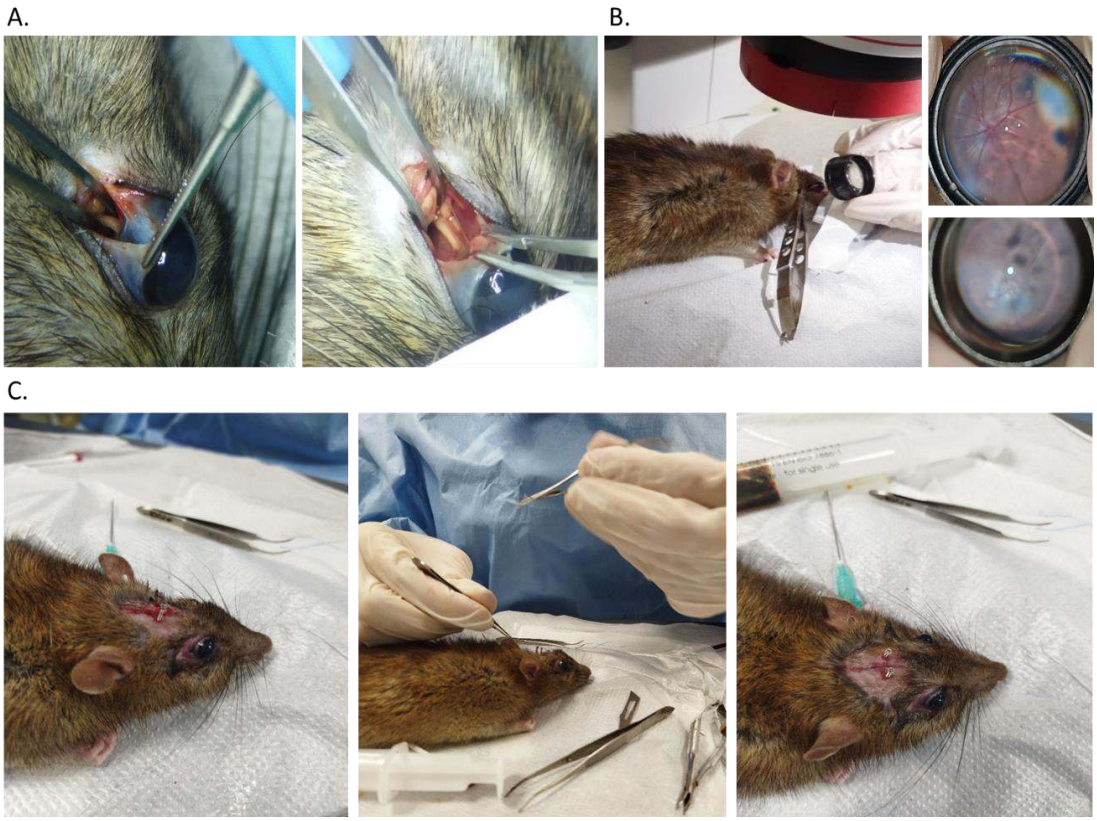

Figure 2.8 Optic nerve crush procedure. The optic nerve area was accessed via A. lateral cantotomy, and the crush was performed using tweezers. B. Retinal fundus photographs of rats in the main experimental group captured using a 90D fundoscopy lens, C. operation followed by VEP-EEG electrode implantation.

2.9.3 Electroretinography (ERG) and VEP-EEG measurements

For dark adaptation, the rats were waited at a dark room for half an hour before measurement. When the dark adaptation period finished, the animals were get under anesthesia and paw pinch reflex and tail reflex were checked to confirm the depth of anesthesia. In addition to general anesthesia, one drop of Alcaine proxymetacaini hydrochloridum (5mg/ml) solution was applied topically to each eye. Pupil was dilated by applying mydriatic tropamide eye drops on experimental eye to open pupil for getting enough light for stimulation.

To evaluate optic nerve damage degree in rats, ERG from the retina and VEP-EEG from the visual cortex were measured by giving a light stimulus under anesthesia, using the BIOPAC MP160 Data Acquisition System having ERS100C amplifier unit with AcqKnowledge software. Ambient illumination was provided with the help of red LED bulb (λmax = 650 nm) during preparation of animals for recordings. The stereotaxic equipment was used to fix head during the recording. Throughout the all procedures under anesthesia, heating pad used to regulate animal's body temperature.

For ERG measurement, custom made silver ring electrode was placed on the sclera as the positive electrodes and the negative electrode was placed touching the cornea. To provide electrode for grounding, the needle was positioned under the rat's tail skin. The system was surrounded by custom made Faraday cage to prevent ambient noise that could affect the measurement. After all electrodes were placed, the custom made light source with white LED 590 nm was opened to measure the retina activation.

2.10 Retina and Optic Nerve Immunohistochemically Analysis

2.10.1 Collection and Fixation of Tissues

Cervical dislocation was done after euthanasia under carbon dioxide in order to obtain tissue. The intraorbital portion of each eye's optic nerves were isolated. After being fixed for 24 hours with a 4% PFA solution, the optic nerves in the eyes were subsequently placed in 10%, 20%, and 30% sucrose solutions, respectively, for another 24 hours. Tissues were dehydrated and then carefully embedded on dry ice in a cryomold encircled by OCT freezing media. Before being sectioned, the frozen tissues were kept for a long time at -80°C. Using a cryostat apparatus (Leica CM 1950), tissues were cut into pieces 10 μm thick, which were then placed onto Superfrost Plus adhesion microscopy slides. Since the ONC model is a vertical procedure, a longitudinal section was taken to observe the damaged area and the healthy tissue transition around it.

2.10.2 Hematoxylin & eosin staining

Tissue sections with H&E staining were examined to evaluate morphological changes and variations in retina and optic nerve in each group. After 45 seconds of room temperature immersion in hematoxylin solution, the sections were rinsed with water to get rid of any remaining stain. The sections were then dipped 12 times in eosin solution and washed with water to eliminate residual dye. After removing excess liquid with a napkin, the sections were immersed in 50%, 70%, 90%, and 100% ethanol, five dips each, to dehydrate the tissue. Excess liquid was again removed with a napkin. The sections were then dipped five times in xylene and tissues were sealed with coverslips by Entellan sealing solution. To prevent air bubble formation, the coverslips were placed at a 45-degree angle while infiltrating the sections with Entellan. Finally, the specimens were observed under a light microscope (DMiL, Leica) to assess the morphological alterations in optic nerve and retina.

2.10.3 TUNEL Assay

Following a PBS rinse, the sections were treated for two minutes in PBS with Triton X-100 (0.1%). The TUNEL Assay-BrdU-Red was carried out by the manufacturer's guidelines was performed after a 5-minute PBS wash. The sections were coated with 50µL of DNA labeling solution and left under dark at 37°C for an hour. At room temperature, BrdU-Red antibody was applied for 30 minutes following a 10 minutes PBS wash. To get rid of any remaining antibody, they were then rinsed with PBS for 5 minutes. For visualization, tissue pieces were coated with coverslips and DAPI containing glycerol: PBS media was utilized. The identical procedures were used to prepare negative controls, with the exception of the antibody solution. Axio Observer Z1 microscopy was used for visualization.

2.10.4 Immunofluorescence staining and imaging

After eight minutes of permeabilization with Triton X-100 (0.1%), the fixed sections were blocked for ten minutes using a superblock solution. The primary antibodies listed below were employed for immunofluorescence staining;

Anti- NeuN: Marker for mature neurons (RGC)
Anti- GFAP: Marker for active Müller glia cells and astrocytes
Anti- GS: Müller glia marker
Anti-Vimentin: Marker for active Müller glia cells and fibroblasts
Anti-Rhodopsin: Photoreceptor cell marker

Following primary antibody incubation, Alexa Fluor 488, 555, 594 or Cy3 secondary antibodies were applied to the sections. Fluorescent microscopy (Axio Observer Z1) was used for tissue imaging.

2.11 Statistical Analysis

Statistical analysis was performed with Prism (GraphPad). In the results, the data is displayed using the mean ± SD or mean ± SEM and indicated. More than two group sizes, ordinary one-way ANOVA for the variations among the groups was performed and *$p < 0.05$ was indicated statistically significant. An unpaired, two-tailed t test was used to compare the two groups, with a statistical significance level of *$p < 0.05$. “ns” on the graphs represents non-significant differences between groups.

3. CHAPTER 3

RESULTS

3.1 P3HT:ITIC Photovoltaic Biointerfaces for Neural Photostimulation

Full text prepared with permission from Kaleli HN, et al. (2024) (Kaleli et al., 2024)
"**Kaleli HN**, Karatum O, Pehlivan Ç, Kesim C, Yıldız E, Sahin A, Nizamoğlu S, Hasanreisoğlu M. P3HT: ITIC polymer based photovoltaic biointerfaces for neural photostimulation. Acta Ophthalmologica. 2024 Jan;102."

3.1.1 Background

Organic photoactive polymers, which are widely used materials for solar panels, have recently been used for photoelectric stimulation on stem cell differentiation and regulating neural cell growth (Milos et al., 2021; Yang et al., 2017). For organic optoelectronic interfaces, the efficiency of the conversion of light into ionic currents and the safe operation of this reaction with cells are of great importance. The availability of different forms of the generated current is associate with active layer of the developed devices' surface. Since faradaic current profiles may effect pH of biological environment, the structures that generate reversible faradaic reactions or, more securely, capacitive reactions can provide safe stimulation for biological environments.

In this study, cell excitation under near-infrared light stimulation was studied with a photocapacitive device based on a donor-acceptor structure containing P3HT:ITIC, which was used for the first time in culture environment. P3HT:ITIC has a suitable structure for biomedical prostheses due to its ability to generate photoelectric current in near-infrared light (NIR). The low energy of the near infrared minimizes the risk of adverse effects while improving tissue penetration.

3.1.2 P3HT:ITIC biointerface fabrication and performance check

Fabrication of the photovoltaic P3HT:ITIC biointerface starts with spin-coating of ZnO nanoparticles as electron transport layer on ITO glass substrates and following P3HT:ITIC thin films as photoactive layer on ZnO layer (Figure 3.1 A). Similar to the working principle of P3HT:PCBM-based organic solar cells (Melikov et al., 2020), the electron-hole pairs formed in the active layer of P3HT:ITIC absorbing light separate due to the electron exchange between P3HT and ITIC (Lin et al., 2015; Yang et al., 2016) (Figure 3.1 B). The effective electron and hole separation due to the energy level of ITIC induces a capacitive current by accumulating ions at electrolyte-device interface. The absorption spectra of the biointerface shows P3HT:ITIC absorbs visible range to 780 nm. (Figure 3.1 C).

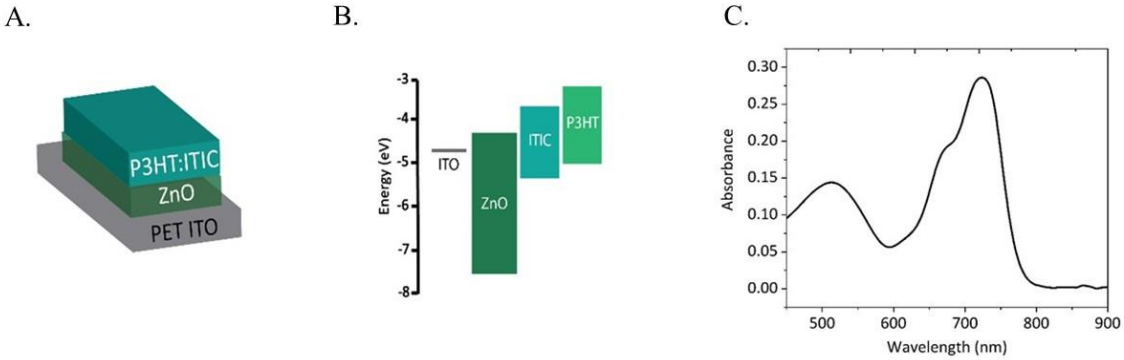

Figure 3.1 ITO/ZnO/P3HT:ITIC device fabrication and characterization. A. Schematic representation of P3HT:ITIC biointerface structure. B. Biointerface's energy band diagram. C. Absorption spectrum of P3HT:ITIC biointerface.

Three-electrode electrochemical system was employed to evaluate photocurrent/photovoltaic values of the devices under light pulses at a wavelength of 780 nm. Various concentrations of P3HT and ITIC solutions were generated in order to determine the optimal photocurrent level. The tested mixture ratios and the amount of generated photocurrent are indicated in the Table 1. It was observed that the P3HT:ITIC with 1:1.5 ratio has the highest photocurrent value compared to other ratios.

Table 1. Photocurrent values measured using different P3HT:ITIC ratio

20 mg/mL P3HT and 20 mg/mL ITIC ratio	Photocurrent values under 780 nm, 1mW/mm^2 light (μA/cm^2)
1:1	420
1:2	490
1:1.5	600
2:1	330
3:1	360
4:3	410

Three-electrode electrochemical setup with reference electrode-Ag/AgCl, platinum probe, and ITO as working electrode was used to measure the photovoltaic and photocurrent values in the aCSF (Figure 3.2 A). In order to excite the devices, light with 10 ms ON were applied using 780 nm LED with 1 mW/mm^2. As the maximum photocurrent level achieved with 1:1.5 ratio of P3HT:ITIC, photocurrent measurement of different layer thicknesses of P3HT:ITIC (20 mg/ml, 1:1.5 mixing ratio) with different spin coating speeds was also studied (Figure 3.2 B) Thinner layer thicknesses are obtained as the spinning speed increases. Increasing the layer thickness leads to more light absorption, resulting in higher photocurrent production until one point. The devices with the layer spin-coated at 2000 rpm have the highest photocurrent value compared to 1000 rpm and 4000 rpm coating speeds. The ITO/ZnO/P3HT:ITIC device prepared with 20mg/ml ITIC as 1:1.5 P3HT ratio and 2000 rpm spin coating has 600 μA/cm^2 capacitive photocurrent (Figure 3.2 C) and high photovoltage values as 200 mV under low light intensities (15 mW/cm^2, 10 ms) (Figure 3.2 D).

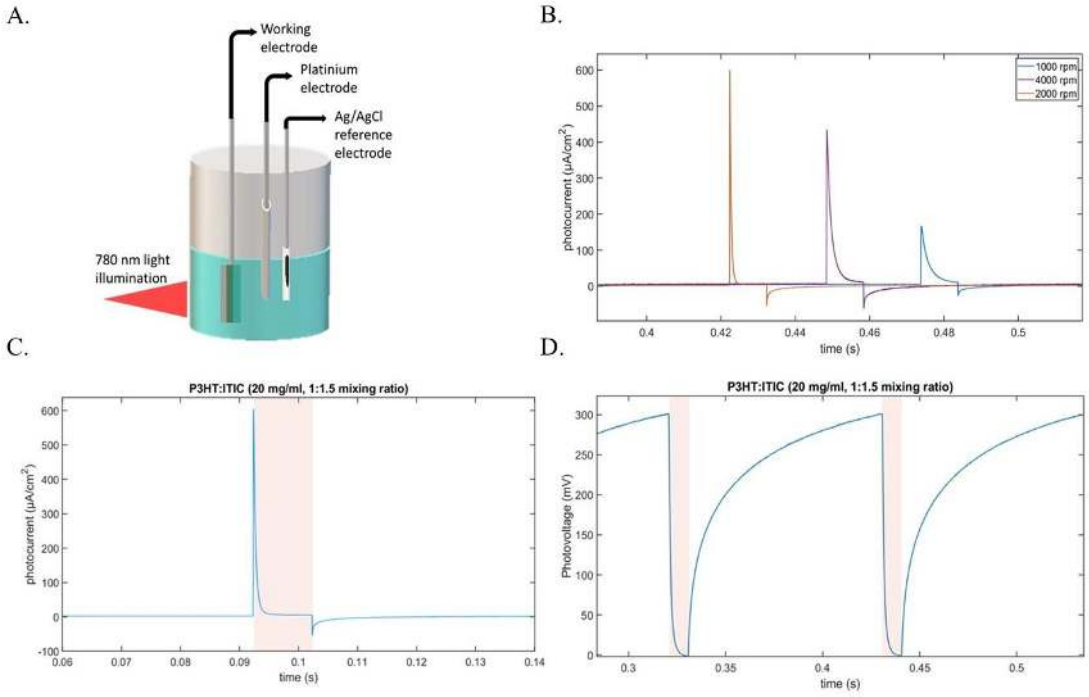

Figure 3.2 Characterization of photoelectrical performance of ITO/ZnO/P3HT:ITIC device. A. Schematic representation of a three-electrode electrochemical measurement system for the photocurrent and photovoltage measurement. B. Photocurrent measurement of ITO/ZnO/P3HT:ITIC devices obtained by coating P3HT:ITIC (20 mg/ml, 1:1.5 mixing ratio) solution with spin coat speeds of 1000 rpm, 2000 rpm, and 4000 rpm. C. Photocurrent and D. photovoltage measurements of devices in ITO/ZnO/P3HT:ITIC under 780 nm, 1 mW/mm^2 light intensity. Light-colored rectangles show the intervals at which the 10 ms light pulse is applied.

Since the thickness is important for the biointerface fabrication, the optimized devices were visualized under cross-sectional SEM to determine the actual thickness of each layer to calculate the total device thickness. Top and crosssectional view of P3HT:ITIC device are presented at Figure 3.3. Thickness of ITO layer was measured as 101 nm, ZnO was 37.4 nm and P3HT:ITIC was 52.65nm.

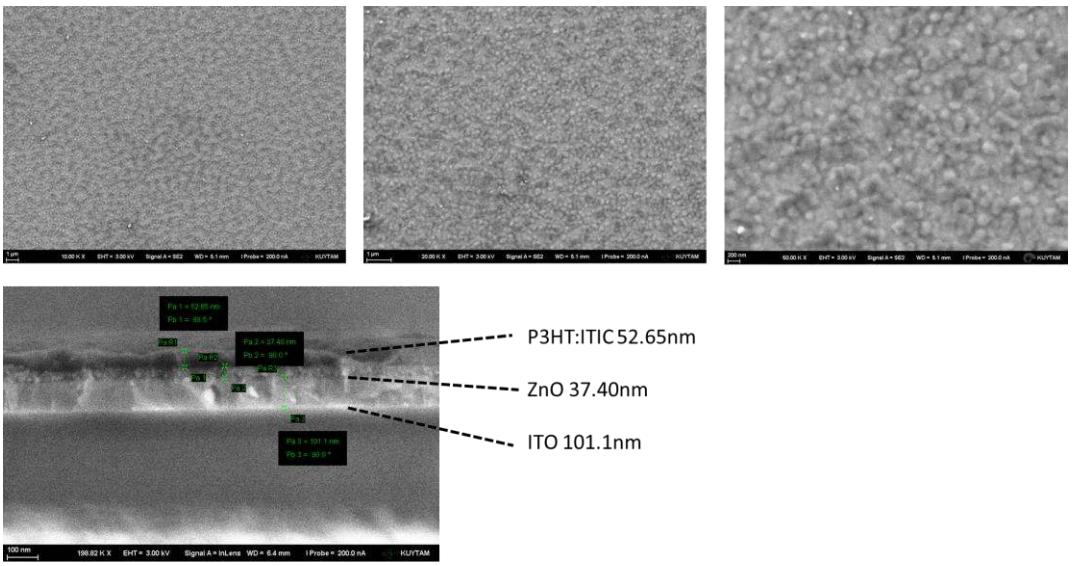

Figure 3.3 Structural properties of P3HT:ITIC device. Surface characteristics of device with different magnification (top) and cross sectional view to show thickness of each layer (bottom).

3.1.3 Biocompatibility Assessments of P3HT:ITIC Biointerface

To evaluate the biocompatibility of the photoactive P3HT:ITIC device, cell viability experiments were performed on primary nervous and visual system cells including primary hippocampal neuron, primary astrocytes and Müller glia (Mio-M1) cells. Müller cells are found between the outer and inner layers, whereas astrocytes are present in the layers of optic nerve fibers and RGCs. They offer physical support and are in charge of the retina's structural organization. Müller cells have special duty in retinal health as clearance of extracellular neurotransmitters generated during signal transduction (Bringmann et al., 2013). They are capable of producing glutamine synthetase, which is essential for neuron signaling and plays a part in the conversion of glutamate to glutamine. By this way metabolization of excessive amount of neurotransmitters and turnover of glutamine in signal mechanism is provided by Müller cells in the retina.

Primary hippocampal neurons and primary astrocytes were isolated from embryonic rats (E16-18) and cultured on control ITO and P3HT:ITIC until DIV5. Mio-M1 cells were cultured on ITO and biointerface when reaching confluency. CTG and LDH cell viability assays were performed to check biocompatibility of biointerfaces. CTG cell viability test measures the amount of ATP produced in the cells. When apoptosis and stress mechanisms are activated or cell metabolism disrupted, ATP level decreases. Surface characteristics of biointerface was suitable for cell attachment as compared to ITO (Figure 3.4 A, D, G). CTG analysis showed that neurons, astrocytes and Mio-M1 cells on P3HT:ITIC has >80% cell viability (Figure 3.4 B,E,H). When cells undergo necrosis or apoptosis, or when the cell membrane is disrupted, LDH is released into culture medium. In addition to CTG cell viability experiments conducted on ITO and P3HT:ITIC biointerfaces, the LDH test was used to assess the integrity of the cellular membrane. High cellular viability was found in three cell types cultured on control and biointerfaces (Figure 3.4 C, F, I).

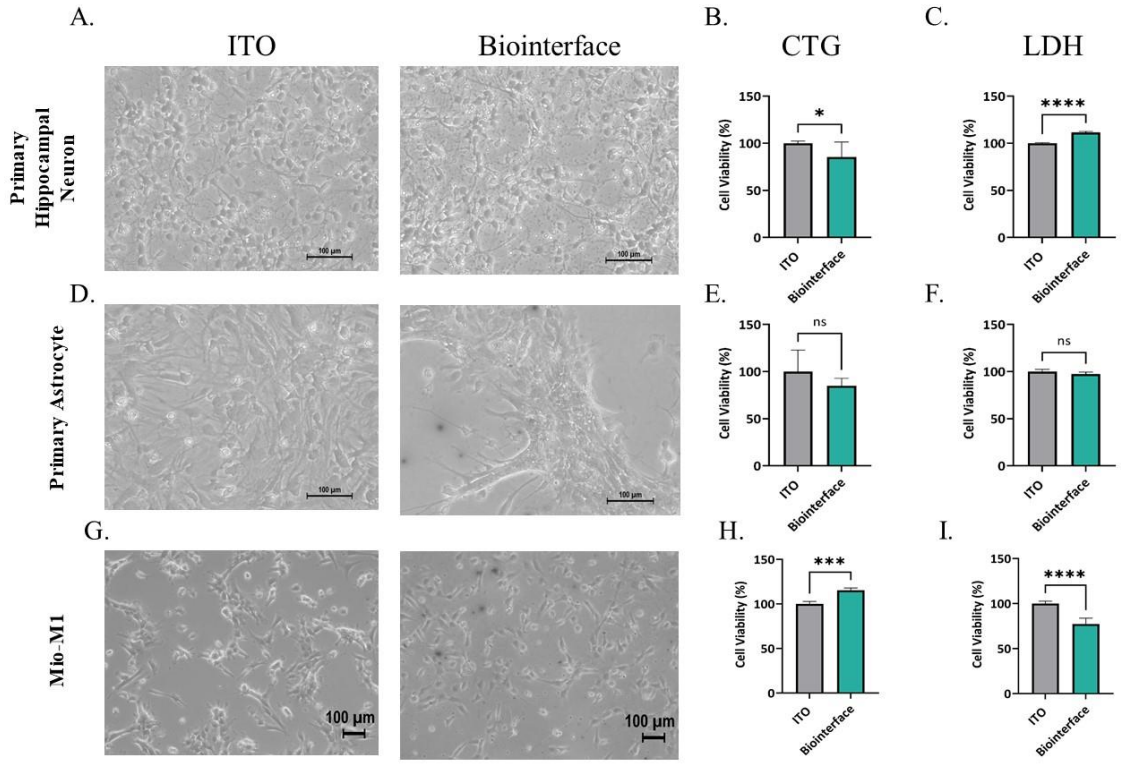

Figure 3.4 Biocompatibility of P3HT:ITIC biointerface. Bright field light microscope images of primary neuron, primary astrocyte and Mio-M1 cells on ITO and P3HT:ITIC (A.,D.,G.) (Scale bar, 100μm). CTG analysis of neurons, primary astrocytes and Mio-M1 cells cultured ITO and P3HT:ITIC biointerface (B.,E.,H.,) and LDH cell viability results (C.,F.,I.) (mean ± SD for n = 4).

While cells generally respond to toxic materials in a short time, chronic toxicity can be examined by the response to long term culture conditions. Survival of cells and maintenance of their characteristics for two weeks of culture period on the biointerface was visualized by immunofluorescence staining of cell specific biomarkers (Figure 3.5). To observe the ratio of neuron cells on the surface, neuron nuclei were stained with NeuN antibody and positive cells were seen similar to the control and biointerface. To check whether long-term culture on the biointerface causes toxicity or not, the cytoskeleton of neurons were examined by F-actin staining and similar cell morphology and cellular network development was visualized. Astrocytes were observed with GFAP staining.

Primary cell cultures were continued throughout the 14 days, showing that the biointerfaces provide a suitable surface environment in long term culture conditions. Immunofluorescence staining of cells on ITO and P3HT:ITIC demonstrated preserved cell viability and morphology which highlight material's biocompatibility.

Beside that there is a possibility of degradation of biointerfaces over time due to factors such as humidity, temperature and pH changes in the culture condition. Possible degradations and release of intermediate materials into culture media must be non-toxic to cells. In this study, we aimed to obtain a rapid response to the suitability of the environment by using primary cells. The response of primary neurons to inappropriate conditions results in rapid cell death. The viability of primary cells during the 2 weeks of the culture period was not affected by compounds that could be released into culture environment due to potential interface disruption. It would be useful to conduct detailed studies on the structural and functional changes in the biointerfaces.

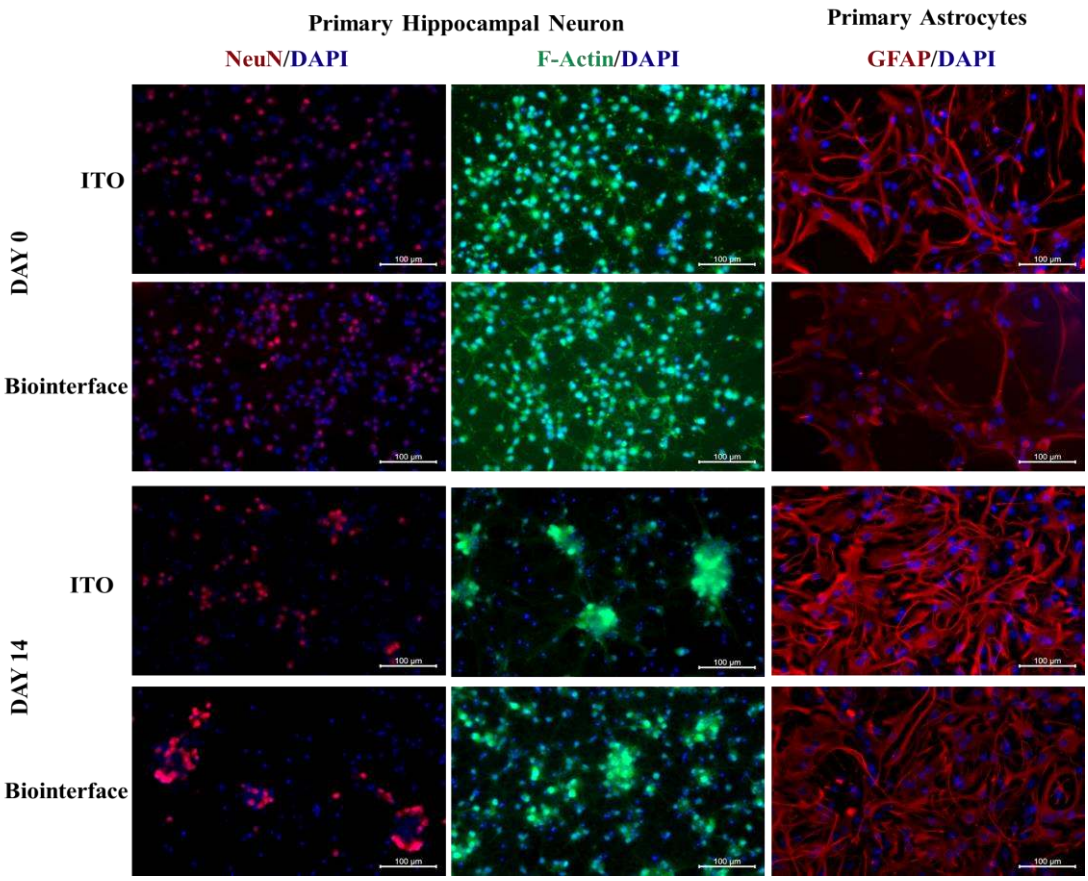

Figure 3.5 Comparison of primary cells cultured on ITO control and P3HT:ITIC biointerface by immunofluorescence staining. Primary neurons were stained with NeuN and F-actin to show expression of neuronal biomarker and to show structure. Primary astrocytes were stained with GFAP (Scale bar, 100µm).

Expression of glutamine synthetase enzyme, a unique biomarker of Müller cells, was also checked and no structural differences were observed (Figure 3.6).

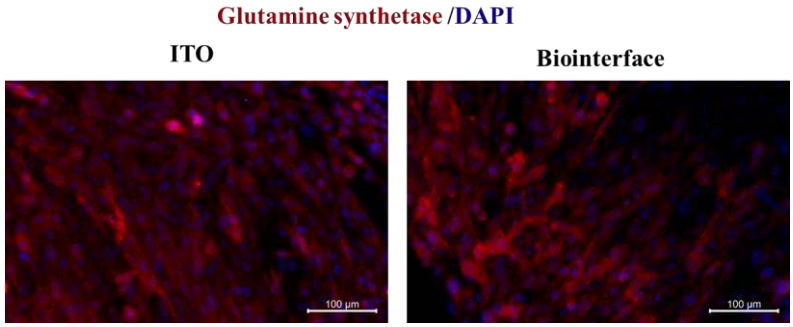

Figure 3.6 Expression of glutamine synthetase of Mio-M1 cells cultured on ITO and biointerface (Scale bar, 100µm).

In order to measure the neural dynamics and physiological activity in individual neurons, the intracellular calcium flux in the neurons on the device was examined during light stimulation. Flou-4AM dye was used to visualize calcium influx under time-lapse fluorescence microscopy during photostimulation. According to the signals obtained from 9 independent cells, rapid calcium release in soma was observed in one cell and a more gradual increase in signals was observed in the others.

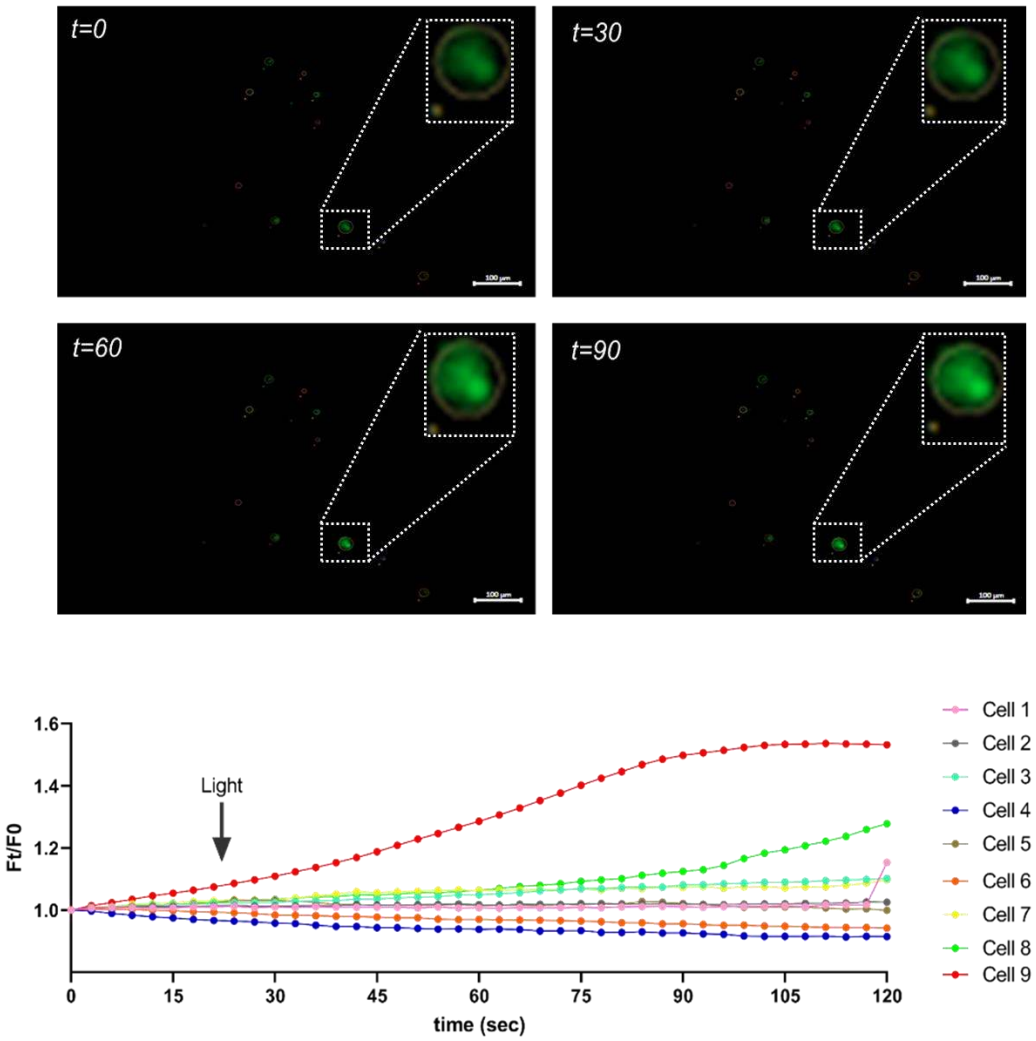

Figure 3.7 Calcium imaging of neuron on the biointerface (Scale bar, 100μm).

3.2 Near Infrared Stimulation of Neurons by $AgBiS_2$ Nanocrystals

(Reproduced with permission from Balamur R, et al. (2024) (Balamur et al., 2024)
"Balamur R, Oh JT, Karatum O, Wang Y, Onal A, **Kaleli HN**, Pehlivan C, Şahin A, Hasanreisoglu M, Konstantatos G, Nizamoglu S. Capacitive and Efficient Near-Infrared Stimulation of Neurons via an Ultrathin AgBiS2 Nanocrystal Layer. ACS Applied Materials & Interfaces. 2024 May 29.")

3.2.1 Background

Nanomaterials capable of generating currents when stimulated by specific light intensity and wavelength have gained significant importance in recent years for effectively developed as optoelectronic biointerfaces for neural stimulation. These interfaces can be designed with different materials to adapt to the cellular environment. The use of quantum dot particles has become widespread in optoelectronic device structures due to their unique structural characteristics and photoelectrochemical features depending on their controlled synthesis procedures (Rühle et al., 2010).

The optical properties of quantum dot based interfaces are changed by particle size and composition, and they can provide bioelectrical stimulation in neurons by light pulses given at certain durations (Karatum, Yildiz, et al., 2022a),(Karatum, Kaleli, et al., 2022b). This ability of quantum particles has strengthened the idea that they can be used for neural interfaces (Han, Karatum, et al., 2022). The functionality of QD based interfaces can contribute to the development of retinal prosthesis thanks to their special optoelectronic properties (Ren & Xu, 2022).

Nanocrystals (NCs) with well-defined crystalline features hold high promise for bioelectronics due to ease to synthesis and high absorption coefficient depending on the size and composition. In current study, we examined toxic heavy metal free $AgBiS_2$ NCs based optoelectronic biointerface for effective optoelectronic neurostimulation in near infrared region (Balamur et al., 2024).

3.2.2 Performance Assessments of $AgBiS_2$/P3HT:RuO_2 Biointerface

Fabrication of the photovoltaic $AgBiS_2$:P3HT biointerface starts with spin-coating of ZnO nanoparticles (NPs) as electron transport layer on ITO glass substrates and following $AgbiS_2$ and P3HT as photoactive layer. ITO/ZnO/$AgBiS_2$/P3HT:RuO_2 biointerface was designed with RuO_2 layer (1:3 area ratio) to provide high capacitance (Figure 3.8 A). When light is absorbed, electron-hole pairs are generated. Band alignment causes these pairs to split apart, with electrons and holes traveling in the direction of the electron to hole transport layer. After that, electrons go to the lower energy states of ZnO before reaching the conductive ITO layer (Figure 3.8 B). At 780 nm, the device's external quantum efficiency (EQE) spectrum displays 0.12 A/W responsivity and ~ 20% device efficiency (Figure 3.8 C). At 0.5 mW/mm2 780 nm light irradiation, the biointerface can generate a photocurrent of 2.15-2.19 mA/cm^2 (mean ± SEM for n=10), photovoltaic maxima of 231-243 mV (mean ± SEM for n=10), and 10.90-11.04 µC/cm^2 charge (mean ± SEM for n=10) (Figure 3.8 D-G).

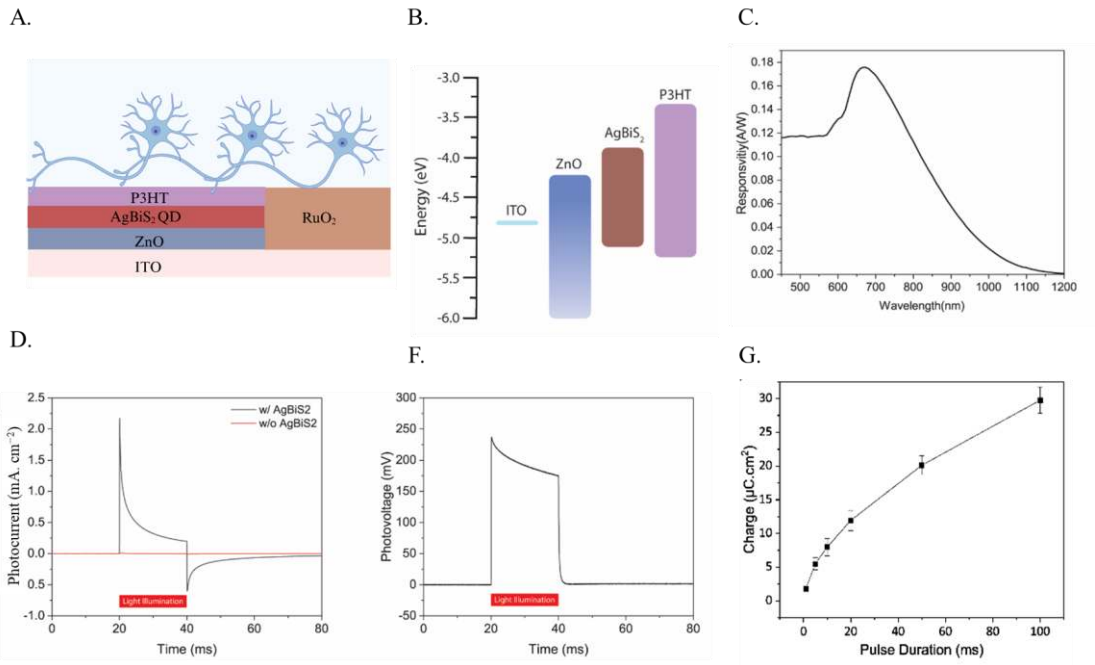

Figure 3.8 $AgBiS_2$ NC based biointerface electrochemical measurements. A. Schematic representation of ITO/ZnO/$AgBiS_2$/P3HT biointerface structure. Created with BioRender. B. Representation of energy band diagram. C. Visible to NIR

absorption spectrum. D. ITO/ZnO/$AgBiS_2$/P3HT biointerface photocurrent response and control without $AgBiS_2$ under 780 nm NIR and 20 ms ON). F. Photovoltage value measured with 780 nm LED. G. Charge levels with different pulse durations.

3.2.3 Biocompatibility Assessments of $AgBiS_2$/P3HT:RuO_2 Biointerface

For optimization of devices in culture condition, SH-SY5Y neuroblastoma cells were used before primary neuron to culture on control ITO and biointerface device. Cell distribution and morphological characteristics were checked under inverted microscope and cells attached similarly on both control and device (Figure 3.9 A). Then cell viability was evaluated through CTG and LDH tests and both results had more than 95% cell viability on devices which indicates suitability of material for biological experiments (Figure 3.9 B, C).

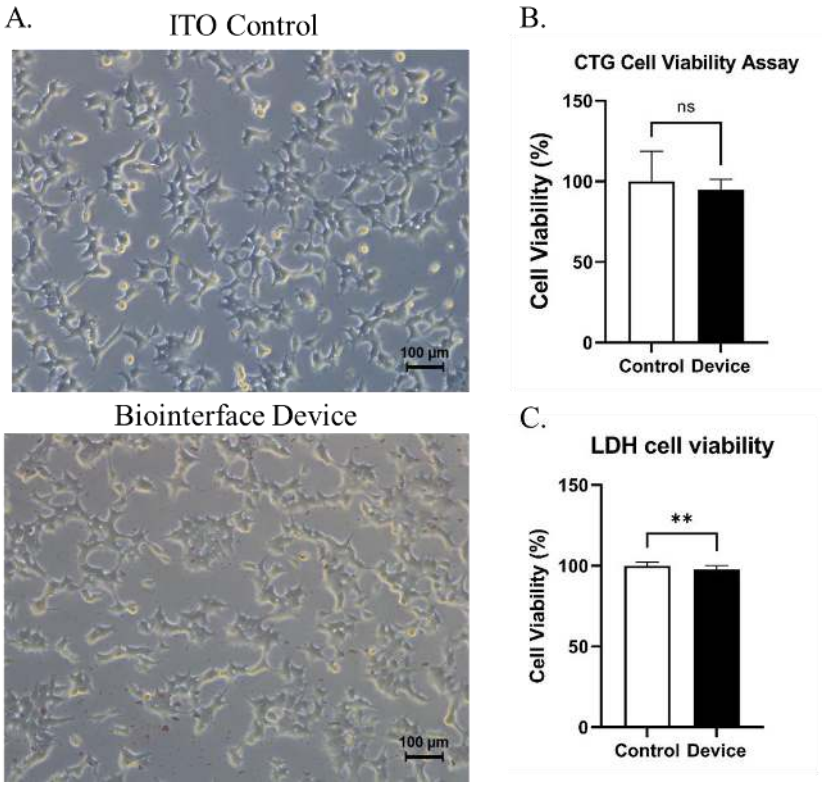

Figure 3.9 Biocompatibility tests of SH-SY5Y neuroblastoma cells cultured on control ITO and biointerface device. A. Light microscope images of cells on ITO and device (Scale bar, 100µm). B. CTG cell viability assay (mean ± SD, n = 4). C. The integrity of the cell membranes on the materials is measured using the LDH leakage assay (mean ± SD for n = 4).

Firstly, to check effect of $AgBiS_2$ layer without biocompatible P3HT layer, only substrate with $AgBiS_2$ (ITO/ZnO/$AgBiS_2$) was used in neuron culture. At Day 0 (DIV5), the short-term consequences of the $AgBiS_2$ biointerface on culture were assessed, and at Day 14 (DIV19), the long term alteration in morphology and properties of neurons were investigated. Bright field images and βIII Tubulin was utilized to assess neuronal structures (Figure 3.10 A). Throughout the 14 days of culture period, the cells remained viable, maintaining their specific characteristics, and exhibiting expanded neural connections, both on the ITO and the $AgBiS_2$ device.

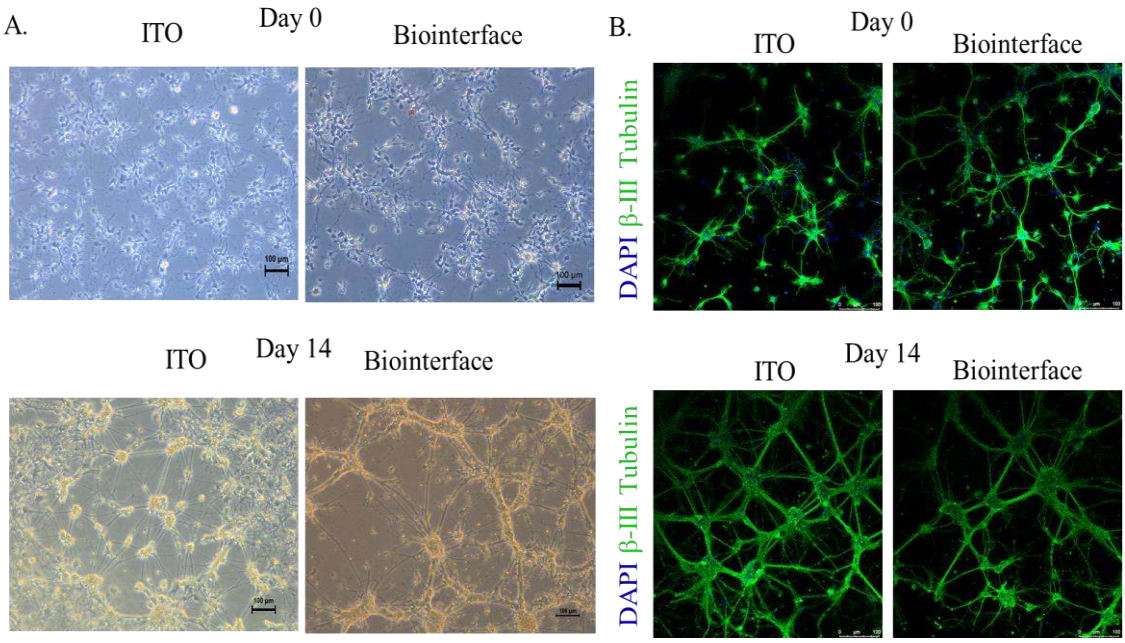

Figure 3.10 Biocompatibility tests of control ITO and ITO/ZnO/$AgBiS_2$ biointerface. A. During the two-week culture period, neurons were cultivated on ITO and biointerface. B. Immunofluorescence pictures of neurons grown on the ITO and ITO/ZnO/$AgBiS_2$ at Days 0 and 14. The nuclear marker DAPI (blue) and the neuronal structural marker anti-β-III-tubulin (green) were used to co-stain the cells (Scale bar: 100μm).

After examining $AgBiS_2$ layer on cell characteristics, complete photovoltaic device (ITO/ZnO/$AgBiS_2$/P3HT) was analyzed in cell culture (Figure 3.11). The cytotoxicity of neurons grown on the samples was investigated through different tests. The LDH assay detects LDH released from cytosol in a culture media, whereas the CTG test determines cell viability based on the quantity of ATP. High survival of cells on $AgBiS_2$ and ITO was demonstrated by CTG assessment (Figure 3.11 B). Additionally, LDH leakage shows biocompatibility, meaning that the primary hippocampus neurons' cellular membrane integrity was unaffected by the biointerfaces (Figure 3.11 B).

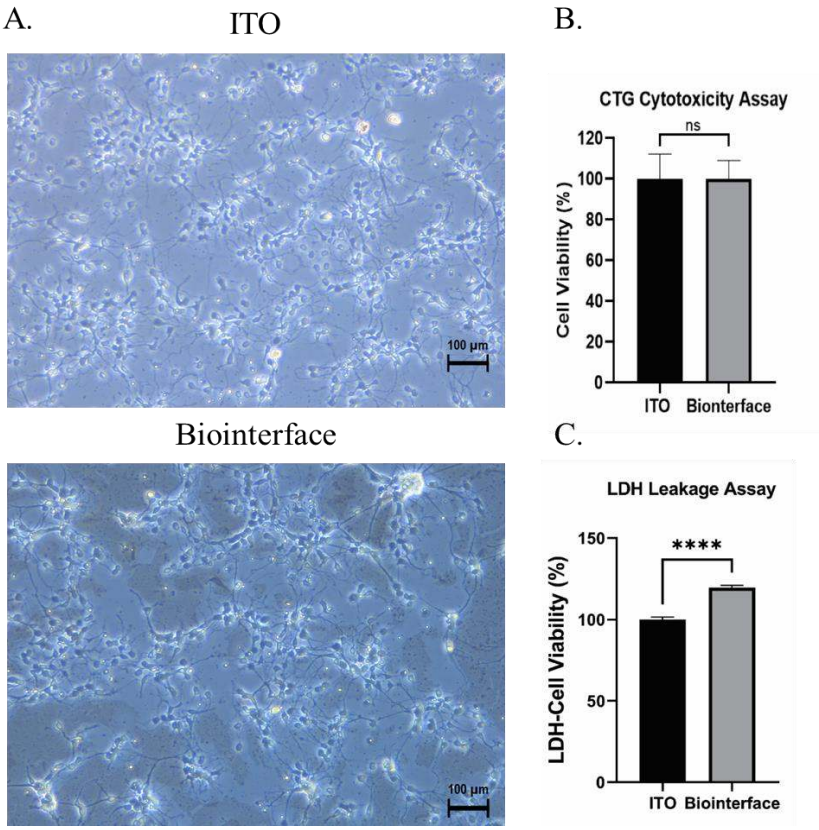

Figure 3.11 Cell viability tests of neurons cultured on biointerface. A. phase contrast images of neurons (Scale bar: 100µm). B. CTG and C. LDH cell viability of neuronal cells on ITO/ZnO/$AgBiS_2$/P3HT and ITO control samples.

Experiments were conducted until Day 14 (DIV19) and during culture period, cell survival and networking were observed under regular microscopic checks. The amount of cells and their morphological characteristics were monitored the short (Day 0) and long term (Day 14) impacts of the materials on neurons. βIII-Tubulin and NeuN labeling was conducted to assess the cellular specific characteristics.

Cells maintained their viability while maintaining their unique features, including an expanded neural network and expressed cell specific proteins. Expression of the NeuN protein, found in the nucleus of mature and non-dividing neurons, over a long period of culture is a good method to observe the suitability of the culture condition. In our study, the number of neurons and all cell/unit area was determined by analyzing DAPI and NeuN-positive cells, and the cells stayed viable in the two-week culture duration(Figure 3.12). The mean number of neurons and total cells at Day 0 on ITO was counted as 753.1 ± 182.4 (mean ± SD, n=4); 1024 ± 240.5 (mean ± SD, n=4) while on biointerface was 742.2 ± 34.01 (mean ± SD, n=4); 804.3± 71.44 (mean ± SD, n=4). The mean number of neurons and total cells at Day 14 on ITO was counted as 579.5 ± 83.97 (mean ± SD, n=4); 749.7 ± 107.7 (mean ± SD, n=4) while on biointerface was 664.0 ± 107.7 (mean ± SD, n=4); 1036 ± 175.0 (mean ± SD, n=4).

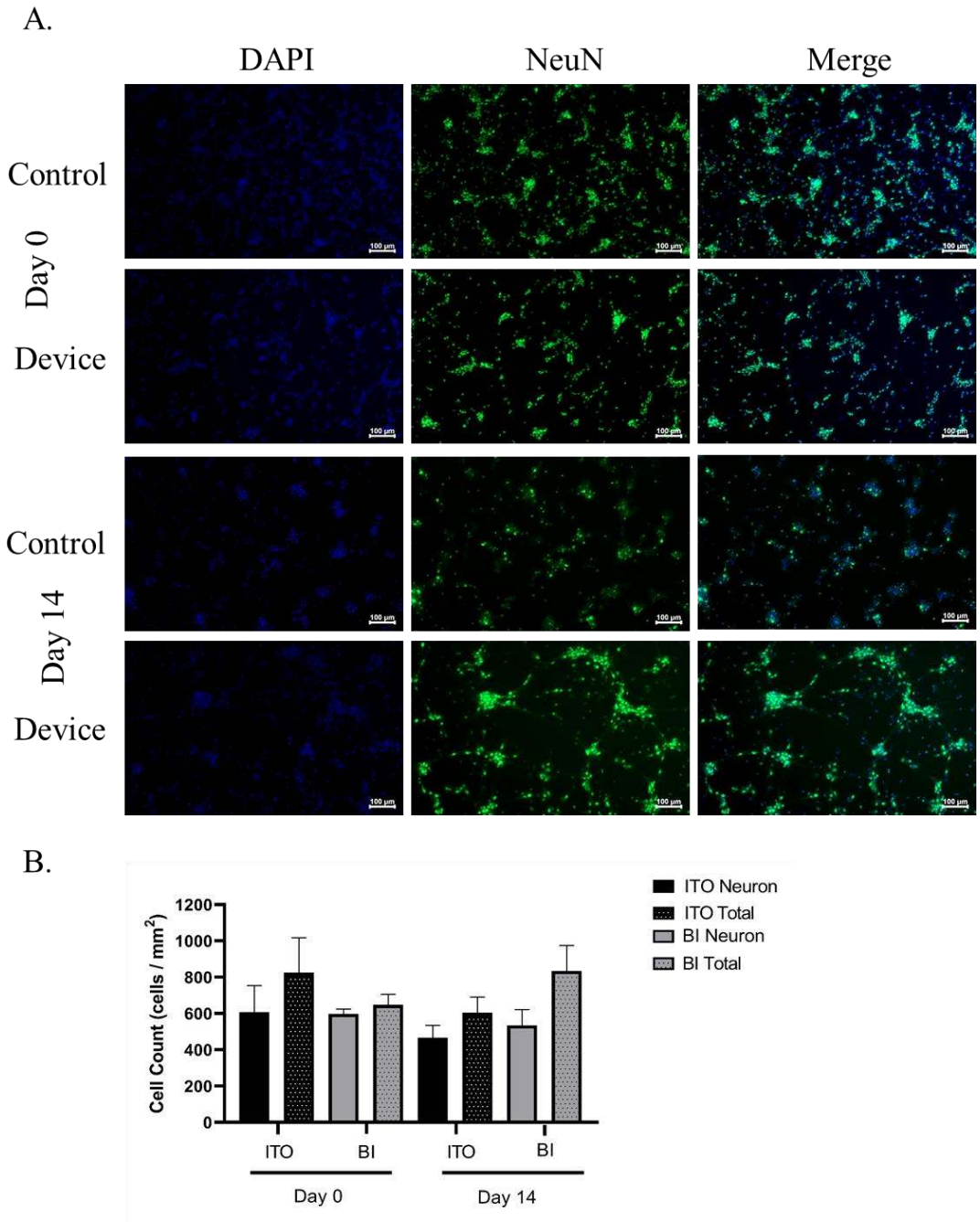

Figure 3.12 Immunofluorescence images of neuronal nucleus on the ITO and biointerface. A. DAPI (blue) and Anti-NeuN (green) nuclear markers were used to co-stain the cells (Scale bar: 100μm). B. Comparison of NeuN expressed cells to the total amount of cells/mm^2 during culture period (mean ± SD, n = 4).

One of the primary indicators of the cytoskeleton that regulates processes including cell shape maintenance, intracellular transport, and division is βIII Tubulin, which is particularly highly expressed in neurons. In contrast to the NeuN protein, βIII Tubulin is present in both adult and developing neurons. It is a good technique to visualize the migration, and development of neurons in culture.

In the current study, neurite length analysis was performed by anti-βIII Tubulin staining and the length of neurite was measured by manually tracing a neurite from the boundary of the soma to the end of neurite. The neurons' neurite outgrowth on the ITO appears to be longer during the first week as 274.2 ± 83.36 μm (mean ± SD, n=50) compared to the biointerface 197.1 ± 69.10 μm (mean ± SD, n=50) (Figure 21). It is thought that different neuron characteristic may be due to the surface morphology of our device. Over the next few days, it was noted that the biointerface's cell populations and axon extensions had increased 199.7 ± 60.67 μm (mean ± SD, n=50) compared to ITO 163.0± 52.73 μm (mean ± SD, n=50) (Figure 3.13).

In long-term culture conditions, cells come closer and create organoid-like formations which enable the development of connections between groups and between cells. The decrease in neurite length seen in ITO at Day 14 compared to Day 0 may come from the development of clump-like forms and the networking established within the group and between the groups.

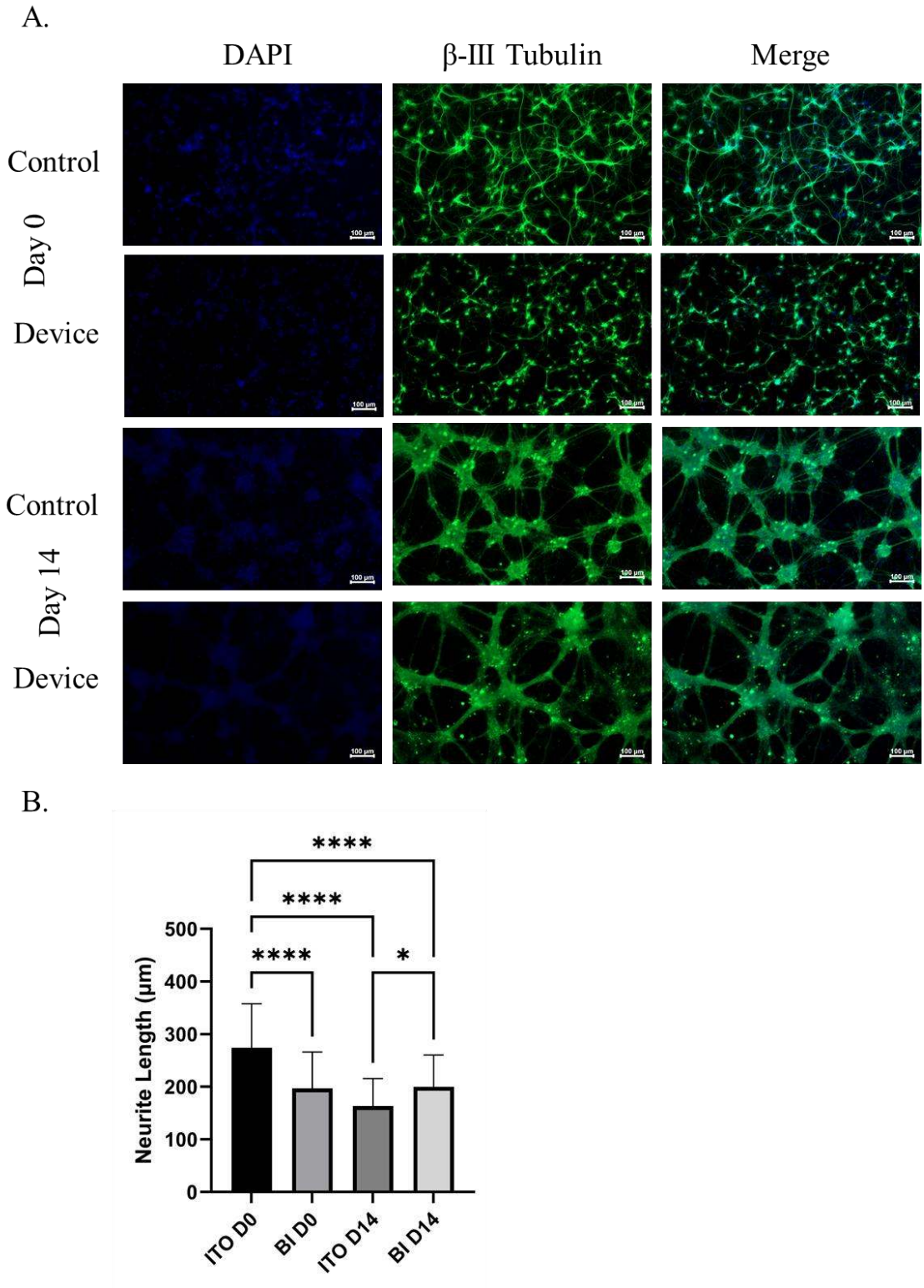

Figure 3.13 Immunofluorescence images of neuronal structures. A. Co-staining with DAPI (blue) and anti-βIII Tubulin (green) (Scale bar, 100μm). B. Comparison of neurite length (mean ± SD, n = 50 cells).

3.3 Biointerfacing with $AgBiS_2$ Quantum Dots for Pseudocapacitive Photostimulation

(Reproduced with permission from Balamur R, et al. (2025)
"Balamur R, Kaya TS, Sariyer S, **Kaleli HN**, Onal A, Caliskan UB, Hasanreisoglu M, Demir-Cakan R, Nizamoglu S. Biointerfacing with AgBiS2 Quantum Dots for Pseudocapacitive Photostimulation. Advanced Functional Materials." Under peer-revision.)

3.3.1 Background

Within a photovoltaic device design, $AgBiS_2$ QDs are integrated onto ZnO nanowires to efficiently convert light to electrical signals with higher efficiency. To enhance device performance, $AgBiS_2$ QDs based biointerface were fabricated with ZnO NWs as shown at Figure 3.14 A. Because of their high surface to the volume ratio structure, nanowires improve light absorption and charge transport in photochemical processes by increasing the surface contact of the active layer in optoelectronic devices.

3.3.2 Photo-electrochemical performance of ITO/ZnO NW/AgBiS2 NC Biointerface

The ZnO NW- $AgBiS_2$ QD device showed more than 2 times higher photocurrent peak (1.6-2.2 mA/cm^2) and 3 times higher charge injection (26.7-31.3 $\mu C/cm^2$) than the optimized QD-based device without NWs (Figure 3.14 C-D). The better performance of the NW-based devices arises from several factors. With increase of light intensity from 15 to 58 mW/cm^2, the total charge injection also increases from 4.4-6 $\mu C/cm^2$ to 26.7-31.3 μC/cm2 (Figure 3.14 C), which is suitable charging capacity for neuron activation.

We compared photocurrent generation of newly designed ITO/ZnO NW/$AgBiS_2$ NC with control ITO/ZnO/P3HT and only ITO/ZnO/$AgBiS_2$ (Figure 3.14 D). The control group exhibited two spikes during the turn-on and turn-off phases of light exposure. This indicates that the photocurrent is sensitive to the light intensity variation indicating a double-layer assisted photocurrent generation. After replacing P3HT with $AgBiS_2$ QD layer, rise in decay time under the light illumination was observed, which is indicative of a Faradaic charge transfer mediated photoresponse.

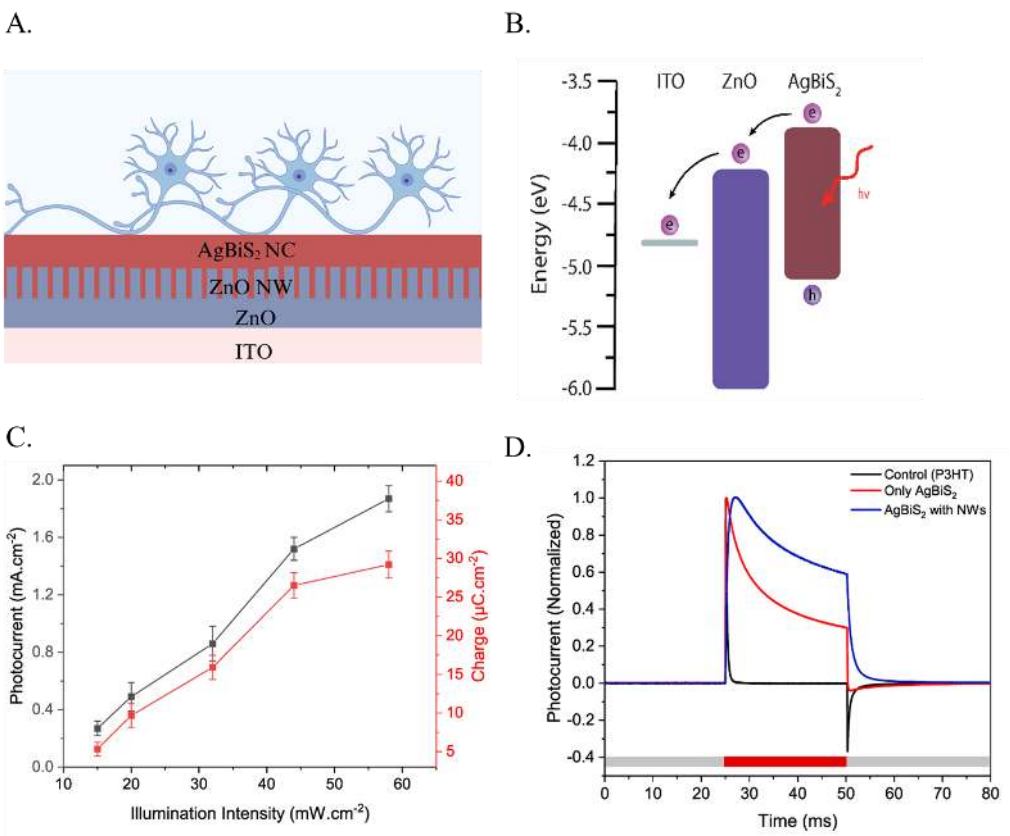

Figure 3.14 ZnO NW-$AgBiS_2$ NC based biointerface electrochemical measurements. A. Schematic representation of ITO/ZnO NW/$AgBiS_2$ biointerface structure. Created with BioRender. B. Representation of energy band diagram. C. Charge as function of illumination intensities under 780 nm light for 20 ms. D. Photocurrent of the control (ITO/ZnO seed/P3HT), devices with ITO/ZnO seed/$AgBiS_2$ and NW-QD under pulsed light illumination. The red line at the bottom indicates when the light is on, while the gray bar represents when the light is off.

3.3.3 Biocompatibility of ITO/ZnO NW/$AgBiS_2$ NC Biointerface

Biocompatibility tests were performed using primary hippocampal neurons isolated from embryonic rats at days 16-18. Primary neurons were cultured on both ITO as a control and the $AgBiS_2$ QD based nanowire devices (**Figure 3.15**). To evaluate the cytotoxic effects of the culture conditions on primary neuron cells, live and dead cell labeling was performed. The results showed similar cell viability on the device and control group.

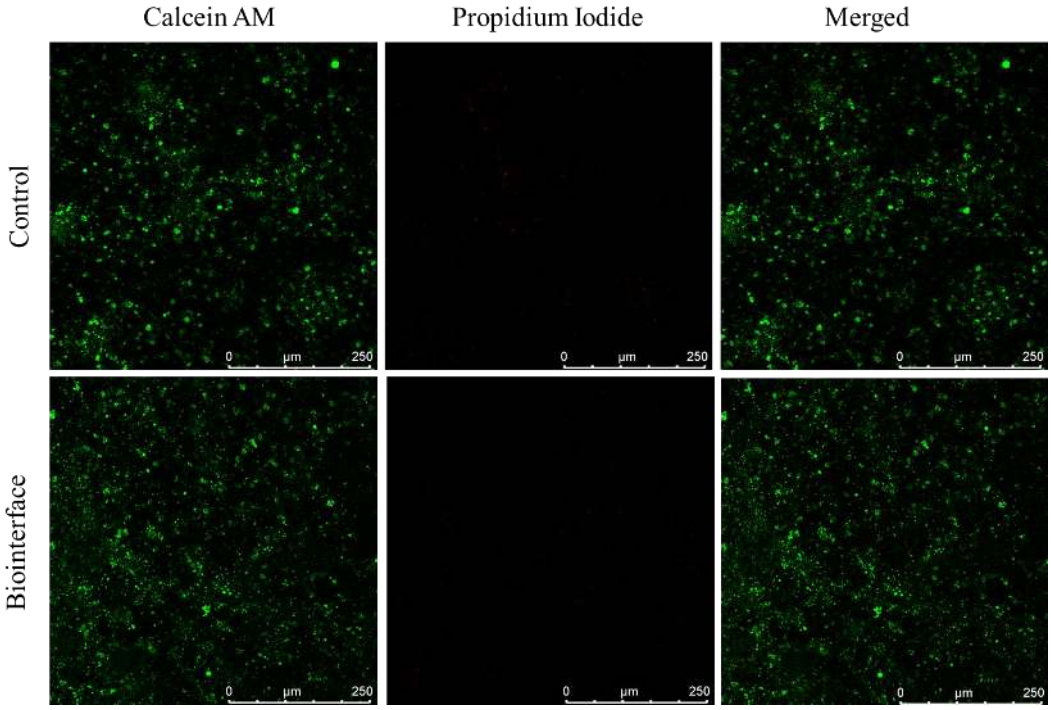

Figure 3.15 The live/dead-calcein AM/PI co-staining was visualized for the viability of cells. Propidium iodide (PI) in red denotes dead cells, whereas calcein AM in green indicates living cells (Scale bar, 250 µm).

Reactive oxygen species (ROS) generation in primary hippocampus neurons grown on biointerfaces was visualized by measuring the fluorescence intensity of the H_2DCFDA agent before and after exposure to light (Figure 3.16 A). A positive control was neurons on ITO treated with 100 µM H_2O_2, while a negative control was neurons grown on ITO. The positive control exhibited high oxidative stress however in terms of fluorescence intensity, and no statistical significant difference between neurons cultivated on ITO and the device before and after illumination observed (Figure 3.16 B).

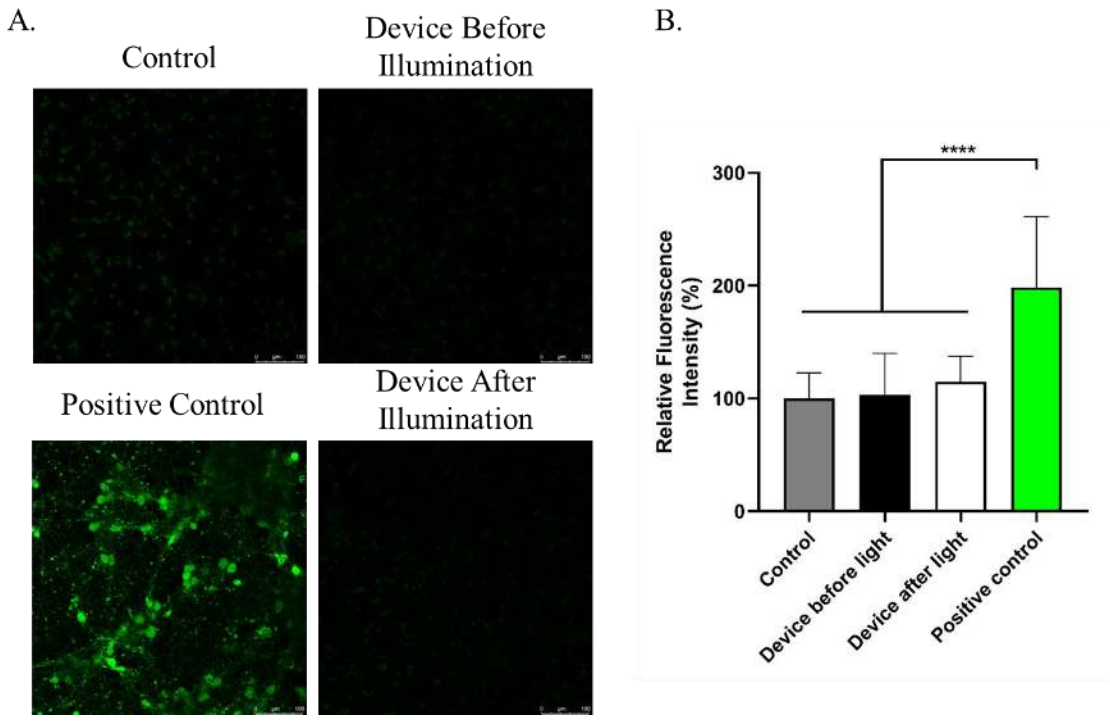

Figure 3.16 Changes in intracellular oxidative stress under light illumination. with ROS assay. A. ROS level of primary neurons cultured on device. Cells were illuminated with 780 nm LED with 10000 cycle, illumination: 5 Hz, 20 ms pulse and 1.5 mW.mm-2 intensity. ITO is negative control and ITO with H_2O_2 is positive control (Scale bar, 100 μm). B. Measured relative intracellular fluorescence intensities.

Another indicator of cellular stress is changes in mitochondrial membrane potential. Since mitochondria play a dynamic role in cellular homeostasis and enhance axonal networking in neurons by supplying energy to axonal and dendritic ends, maintaining mitochondrial membrane potential is crucial for sustaining cellular metabolism. Here, JC-1, a fluorescent indicator of mitochondrial membrane potential, was used to visualize healthy and disrupted organelles after light illumination (Figure 3.17). The ratio of aggregate to monomer signals before and after light illumination indicates the preservation of mitochondrial membrane potential and overall mitochondrial health.

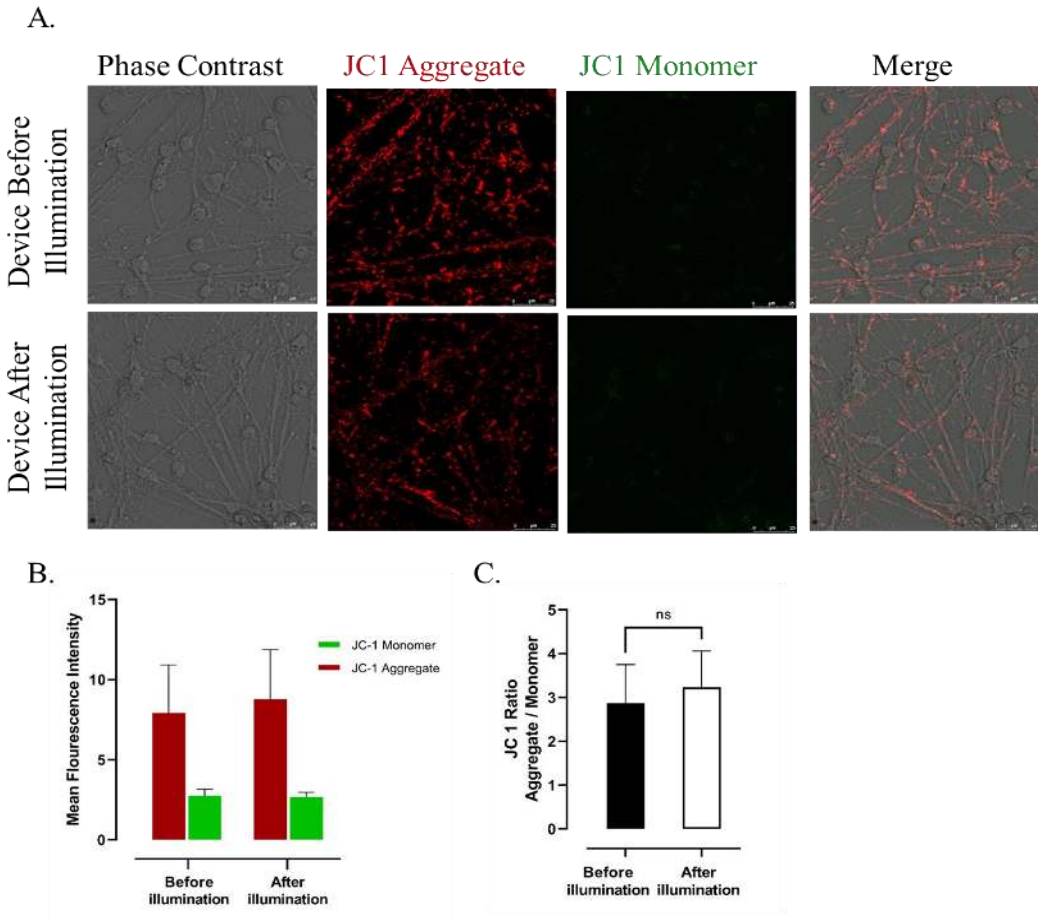

Figure 3.17 Mitochondrial membrane potential (MMP) changes in neurons cultured on biointerface. A. JC-1 red aggregates refer to healthy mitochondria while JC-1 green monomers show disrupted mitochondria. Cells were illuminated with 780 nm LED with 10000 cycle, illumination: 20 ms pulse, 5 Hz, 1.5 mW/mm^2 intensity. B. Mean fluorescence intensity of red and green signals in device before and after light illumination. C. Ratio of aggregate to monomer in device before and after light illumination.

To detect light dependent activation of neuron cells cultured on the biointerface, an intracellular calcium release test was performed. Calcium is a crucial agent in neurons, playing a significant role in action potentials and synaptic transmission by triggering the release of neurotransmitters for signal transduction. When calcium levels rise in the synaptic cleft, it facilitates the release of neurotransmitters from vesicles, enabling synaptic transmission. To observe this release, cells were stained with Fluo-4 AM, a calcium indicator, and calcium levels were recorded for 180 seconds (Figure 3.18 A, B). The light illumination at 5 Hz, 20 ms ON – 180 ms OFF for 10 seconds duration with 1.5 mW/mm² intensity was applied during capturing. The fluorescence intensity of randomly selected cell at a given time point (ΔF) was divided by the starting fluorescence intensity of cells (F0) to determine changes in fluorescence levels over time. The fluorescence intensities of neurons on the device increased upon light exposure as shown in Figure 3.18 C. Analysis of eleven randomly selected cells showed an average increase of 5% in calcium fluorescence traces (Figure 3.18 D).

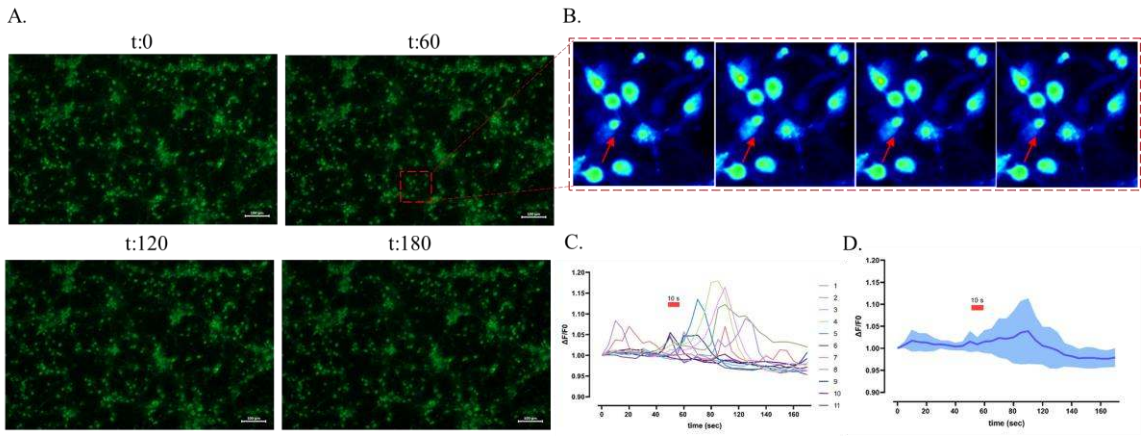

Figure 3.18 Flou-4AM calcium imaging. A. Changes in fluorescence signals before, during, and after light illumination. B. Rainbow representation of calcium release of single neuron (red arrow) cultured on biointerface after 780nm light stimulation with stimulus frequency, 5 Hz; 20 ms pulse-width; light duration, 10s. C. Florescence intensity changes before and after illumination on single neurons. Light stimulation was performed at 60s for 10s. D. Mean of relative florescence intensity changes of eleven different neurons on biointerface.

3.4 Near infrared photostimulation of *in vitro* neuron and *ex vivo* retina via ZnO nanowire based $AgBiS_2$ NC

(Reproduced with permission from Kaleli HN & Kaya TS, et al. (2025)
"**Kaleli HN***, Kaya TS*, Joffrois C, Chaffiol A, Pehlivan C, Şahin A, Hasanreisoglu M, Nizamoglu S. Near infrared photostimulation of in vitro neuron and ex vivo retina via ZnO nanowire based $AgBiS_2$ NC. Full text under preparation."

3.4.1 Background

As a final design of biointerface, we created an enhanced structure with ITO/ZnO NW/$AgBiS_2$/P3HT with RuO_2 return electrode after confirming cellular excitation and biocompatibility with QD based biointerfaces and ZnO nanowire with our previous studies. The active device's capacitive current increase as a result of the RuO_2 structure. Additionally, as we showed in our earlier work, the P3HT structure greatly enhanced the device performance. The final structure with P3HT in active layer and RuO2 as return electrode combination provides more than two-fold increase in photocurrent compared to devices without them.

In blind retinas, retinal prosthesis that bridge the internal retinal signaling pathways broken due to photoreceptor degeneration can directly stimulate retinal ganglion cells by transforming light energy into electrical stimulation. *Ex vivo* experiments on blind retina provide testing our biointerface's functionality and demonstrating robust responses under light stimulation. Despite our earlier studies, current study demonstrated for the first time the tissue stimulating capability of the biointerface we developed.

3.4.2 Performance Analysis of ITO/ZnO NW/$AgBiS_2$ NC/P3HT:RuO_2 Biointerface

The biointerface is composed of ITO/ZnO NW/$AgBiS_2$ QD/P3HT active area for photocurrent generation as well as ITO/RuO_2 as return electrode to complete the electrical circuit as shown at Figure 3.19 A. Cross-sectional scanning electron microscopy (SEM) shows 20 nm ZnO seed layer, 240 nm ZnO NW-QD interdigitated layer, 60 nm QD overlayer, and 20 nm P3HT layer (Figure 3.19 B).

The biointerface exhibited peak photocurrent and photovoltage values of 2.42 mA and 294 mV, respectively, under 880 nm near-infrared (NIR) light illumination (Figure 3.19 C, D). The amount of charge generation is also a critical factor for effective neuronal stimulation. The biointerface induces a charge density of 12-15 $\mu C/cm^2$ at an illumination intensity of 89 mW/cm^2 using 20 ms pulses and the value increases with pulse width as shown in Figure 3.19 E. Also, the charge generation performance of the biointerface increases with increasing light intensity. The device can generate a charge density of 3.5 $\mu C/cm^2$ even at low light intensities as 18 mW/cm^2 of 880 nm near-infrared (NIR) light illumination.

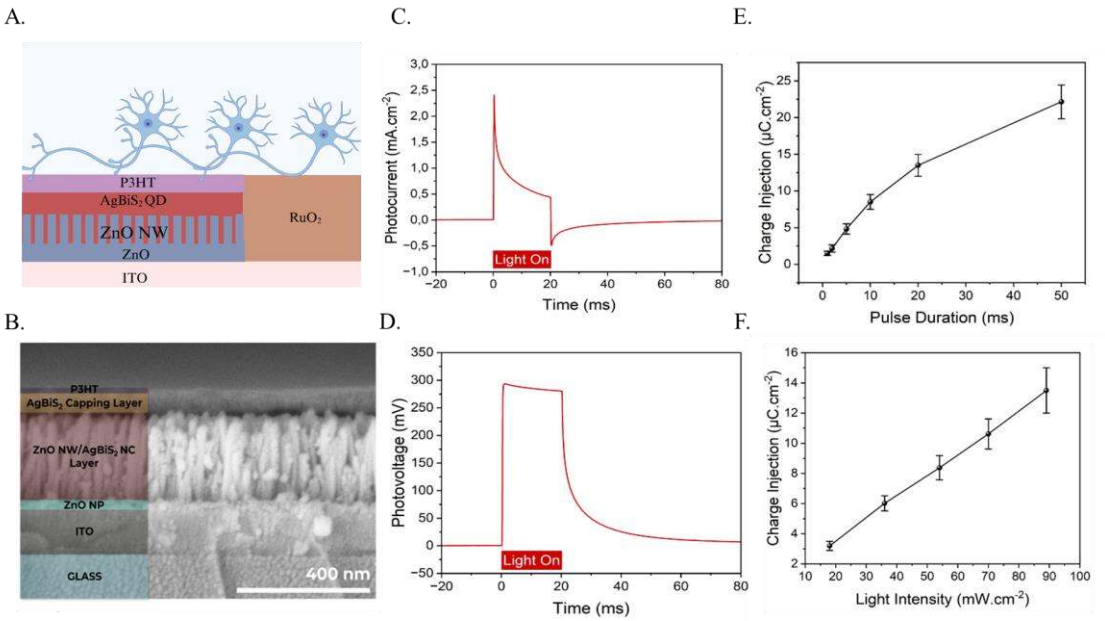

Figure 3.19 Electrochemical features of ITO/ZnO NW/$AgBiS_2$ NC/P3HT:RuO_2 Biointerface. A. Schematic representation of biointerface structure. Created with BioRender. B. Cross-sectional SEM image. C. Photocurrent and D. photovoltage of the biointerface under 880 nm NIR light (20 ms, 89 mW/cm^2). E. Photogenerated charge density of the biointerface for different pulse durations. F. Charge density of the biointerface by change in light intensity.

3.4.3 Biocompatibility of ITO/ZnO NW/$AgBiS_2$ NC/P3HT:RuO_2 Biointerface

Biocompatibility tests were conducted with neurons cultured on two different samples: ITO and fabricated photovoltaic nanowire device. The cell survival of neurons grown on substrates was examined using the CTG, MTT cytotoxicity, and LDH tests. Neurons on the biointerface showed high cell viability similar to the control (Figure 3.20 B). In addition to the CTG assay, a colorimetric MTT test is also performed to examine metabolically active cells on devices. Primary hippocampus neurons on the biointerface demonstrated greater viability than control in the MTT cytotoxicity test (Figure 3.20 C). Furthermore, LDH leakage test showed that the devices had no adverse effects on the viability and integrity of the cell membrane (Figure 3.20 D, E).

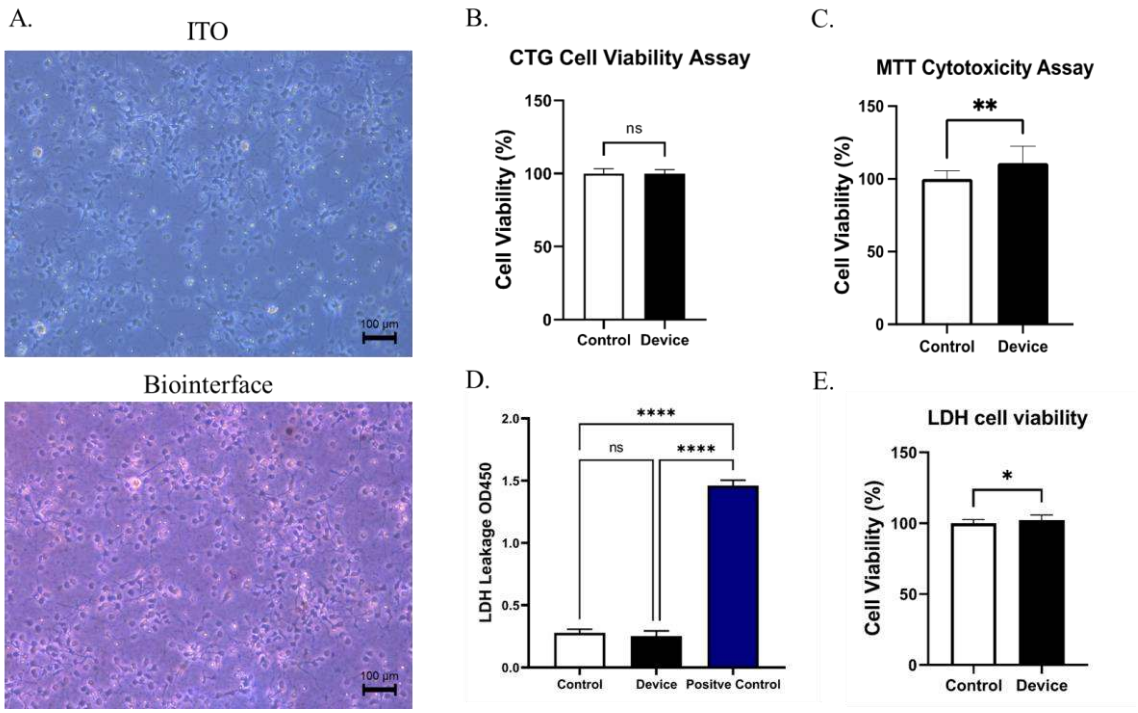

Figure 3.20 Cell viability tests of neurons cultured on control and device. A. Bright field images of cells at DIV 3 (Scale bar, 100 µm). B. CTG assay for quantifying cell viability through cellular ATP level (mean ± SD, n = 4). ITO sample was used as a control. C. MTT assay for measuring cytotoxicity of neurons (mean ± SD, n = 4). D. LDH leakage from neurons (mean ± SD for n = 4). E. Relative cell viability.

The neuronal population in the culture was evaluated using NeuN and βIII-Tubulin immunostaining, as in our earlier studies. NeuN protein expression provides identification of non-dividing neurons, allowing to assess the viability and maturation of them over time. Additionally, neuronal cytoskeletal structures were examined through βIII-Tubulin immunostaining. This protein is widely expressed in both developing and mature neurons, and used to evaluate neuron cells' morphology, differentiation, and dendritic-axonal growth.

The mean number of neurons and total cells at Day 0 on control was counted as 596.4 ± 335.0 (mean ± SD, n=8); 914.9 ± 345.3 (mean ± SD, n=8) while on the device was 814.1 ± 132.0 (mean ± SD, n=8); 936.3 ± 207.1 (mean ± SD, n=8). The mean number of neurons and total cells at Day 14 on control was counted as 579.7 ± 98.03 (mean ±

SD, n=8); 891.6 ± 145.5 (mean ± SD, n=8) while on the device was 650.2 ± 77.68 (mean ± SD, n=8); 800.8 ± 98.33 (mean ± SD, n=8). Consistent with the cell viability results, the immunofluorescence staining technique showed that the photovoltaic nanowire device has good biocompatibility.

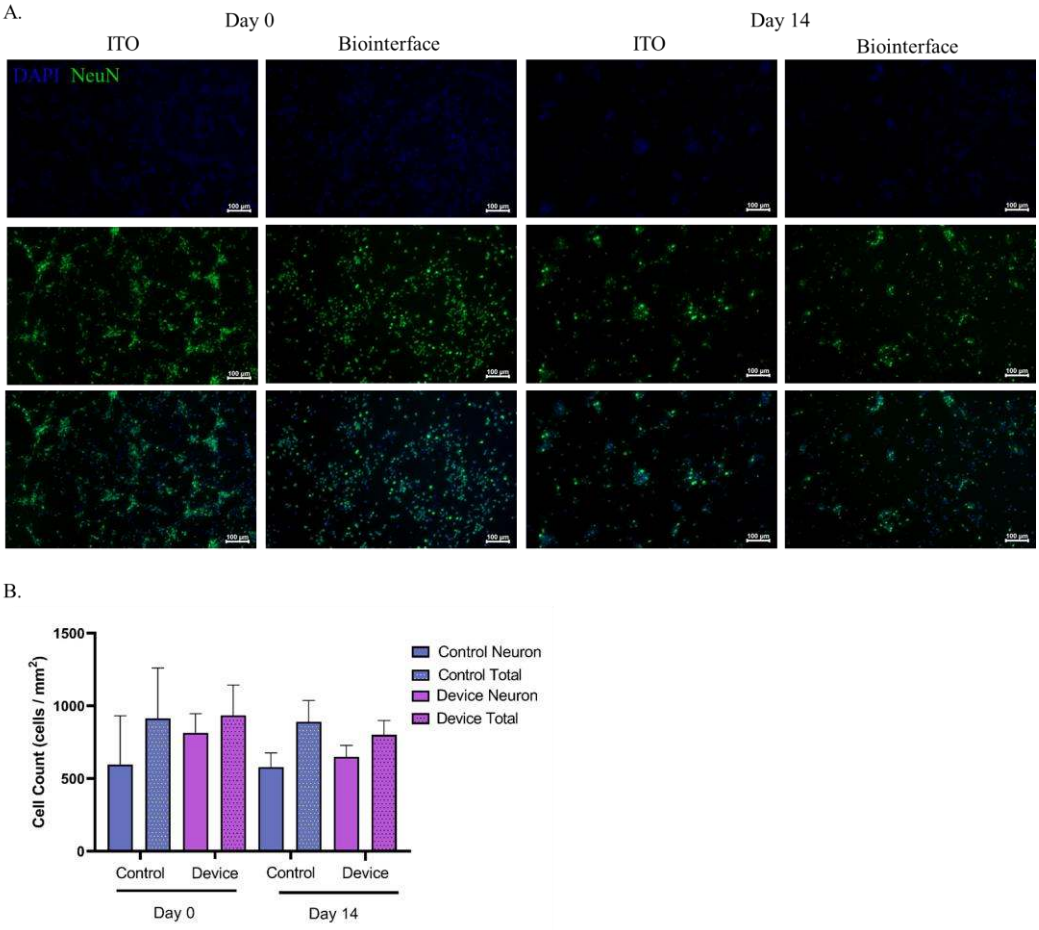

Figure 3.21 Short and long term neuron culture on substrates. A. Co-staining with DAPI (blue) and anti-NeuN (green) (Scale bar, 100μm). B. Comparison of NeuN expressed and total number of cells per mm^2 during culture period shown in immunofluorescence images (mean ± SD, n=8).

Over the duration of the 14-day culture period, the primary hippocampus cells maintained their viability and displayed their unique properties with parallel distribution on the control and biointerface (Figure 3.21).

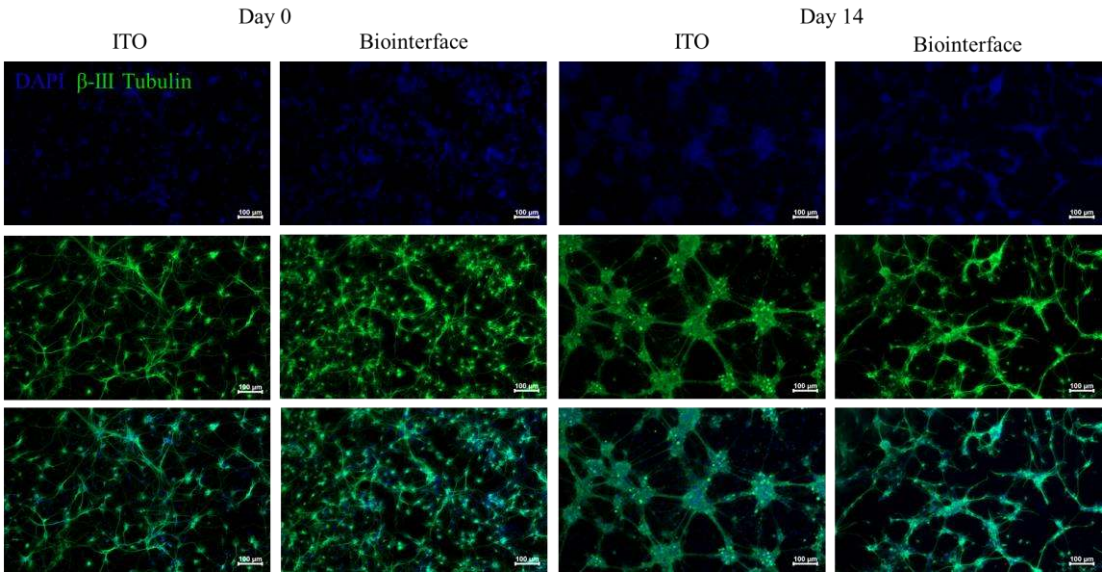

Figure 3.22 Short and long term neuronal structural changes cultured on substrates. DAPI (blue) and anti-βIII-Tubulin (green)(Scale bar: 100μm).

Since activation of biointerface is facilitated by light stimulation, it is crucial to check how the modulation of reactive oxygen species (ROS) generated under illumination influence cellular processes. ROS play a dual role in cellular physiology where at low or moderate levels they function as signaling molecules to facilitate cellular metabolism, but at high levels, they cause oxidative stress and damage cellular components. So, it is important to investigative how repetitive light illumination on optoelectronic device affects ROS levels in neurons cultured on. For this purpose, the H_2DCFDA agent was used as a reporter, which reacts with ROS and converts into the fluorescent end product DCF within the cell (Figure 3.23 A). Visualization of ROS production in primary hippocampal neurons cultured on biointerfaces was performed by measuring the fluorescence intensity of the H_2DCFDA agent before and after illumination of the devices with 780 nm light with 10000 cycle, illumination: 5 Hz, 20 ms pulse, 1.5 mW/mm^2 (Figure 3.23 B). Neurons cultured on ITO were used as a negative control, while neurons on ITO incubated with H_2O_2 1(00 μM) used as a positive control. As expected, the positive controls showed higher fluorescence intensity because of increased oxidative stress. No significant difference was observed in fluorescence intensities of cells cultured on control, the device before illumination, and the device after illumination (Figure 3.23 C).

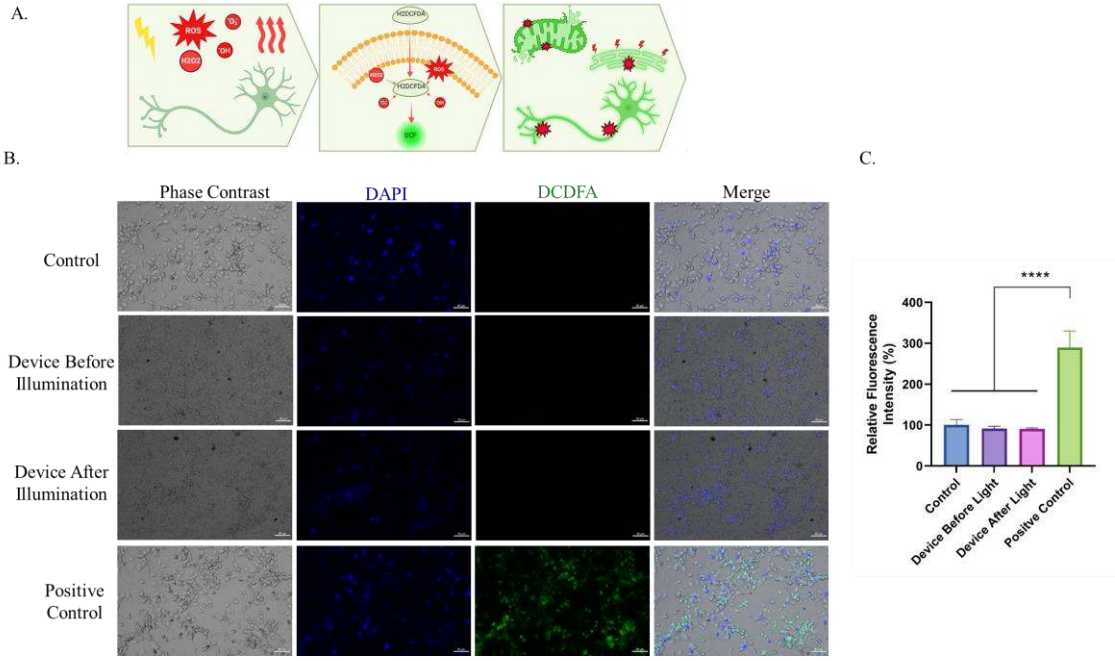

Figure 3.23 Intracellular oxidative stress with ROS assay. A. Representative image of H_2DCFDA working principle. B. Stress level of primary neurons cultured on the biointerface was visualized after subjecting to 10000 photoexcitation cycle, illumination: 5 Hz, 20 ms pulse, 1.5 mW/mm^2 intensity. ITO is negative control, ITO with H_2O_2 is positive control (Scale bar, 50 μm). C. Measured relative intracellular fluorescence intensities.

Mitochondria are highly dynamic structures that primarily function in energy production and cellular homeostasis in cells. In neuronal cells, mitochondria are located in pre and post synaptic regions and regulate axonal-dendritic development, axonal regeneration, and networking. Mitochondrial dysfunction is a critical factor in neurodegenerative diseases, as overstimulated oxidative stress can lead to mitochondrial dysfunction, triggering cellular clearance mechanisms like autophagy and ultimately resulting in cell death. Changes in MMP are a key indicator of mitochondrial dysfunction. In healthy cells, the fluorescent dye JC-1 forms red aggregates; in damaged cells, it transforms into green monomers (Figure 3. 24 A). The maintenance of mitochondrial health is shown by the ratio of aggregate to monomer signals.

As demonstrated through H_2DCFDA staining, 30 minutes of light stimulation did not cause oxidative stress in neurons. Additionally, to assess potential mitochondrial changes, cells were exposed to 780 nm light for 2 seconds with 5 Hz, 20 ms, 1.5 mW/mm^2, and the levels of aggregates and monomers were measured over time (Figure 3.24 B). The data showed a slight decrease in aggregate but not increase in monomer fluorescence intensity in both the control and the device starting from the capturing (Figure 3.24 C). The decrease in the aggregate-to-monomer ratio was likely due to a decrease in red signals from JC-1 under continuous laser exposure during experiment, rather than mitochondrial dysfunction (Figure 3. 24 D).

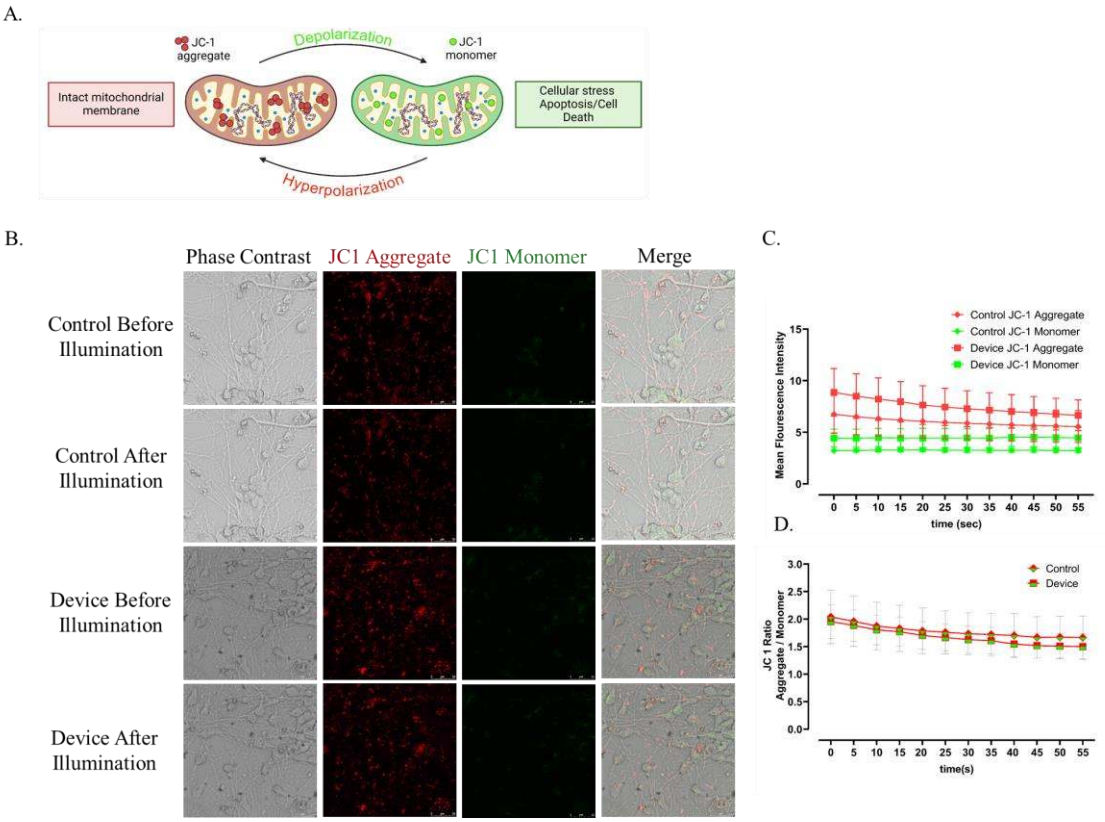

Figure 3.24 Dynamic mitochondrial health assessment through JC-1 staining before and after light illumination. A. Schematic representation of mitochondrial membrane polarization. B. Bright field and fluorescence images of cells cultured on ITO control and devices. (Scale bar, 50 µM). Cells were subjected to 780 nm light for 2 sec with 5 Hz, 20 ms, 1.5 mW/mm^2 intensity. C. Average fluorescence intensity of

green monomer and red aggregate in the device and control over time. D. Comparison of JC-1 aggregate to monomer fluorescence intensity ratio.

To visualize neural activities cultured on a device, stimulations within the near-infrared (NIR) spectrum utilizing with 780 nm light were employed for real-time calcium imaging (Figure 3.25). Primary embryonic hippocampal cells were culture on devices until DIV 10, then treated with the Fluo-4 AM, calcium indicator to detect intracellular Ca^{2+} fluorescence under 780nm light stimulation with stimulus frequency, 5 Hz; 20 ms pulse-width; light duration, 2s or 10s; intensity, 1.5 mW/mm^2. The fluorescence intensity of randomly chosen cells at particular time point (ΔF) was divided by cell's initial fluorescence intensity (F0) to determine the change in fluorescence levels. Notably, the fluorescence intensities of neurons on the device exhibited an incline upon exposure to light for 10 sec (Figure 3. 25 C-E) and for 2 sec (Figure 3. 25 B, F, G). Analysis of eleven randomly selected cells revealed an average 20% increase in calcium fluorescence traces (ΔF/F0) under 10 sec illuminations (Figure 3.25 E) while nine cells illuminated for 2 sec showed 5% increase (Figure 3.25 F) in calcium influx. ITO was used as negative control of light experiments.

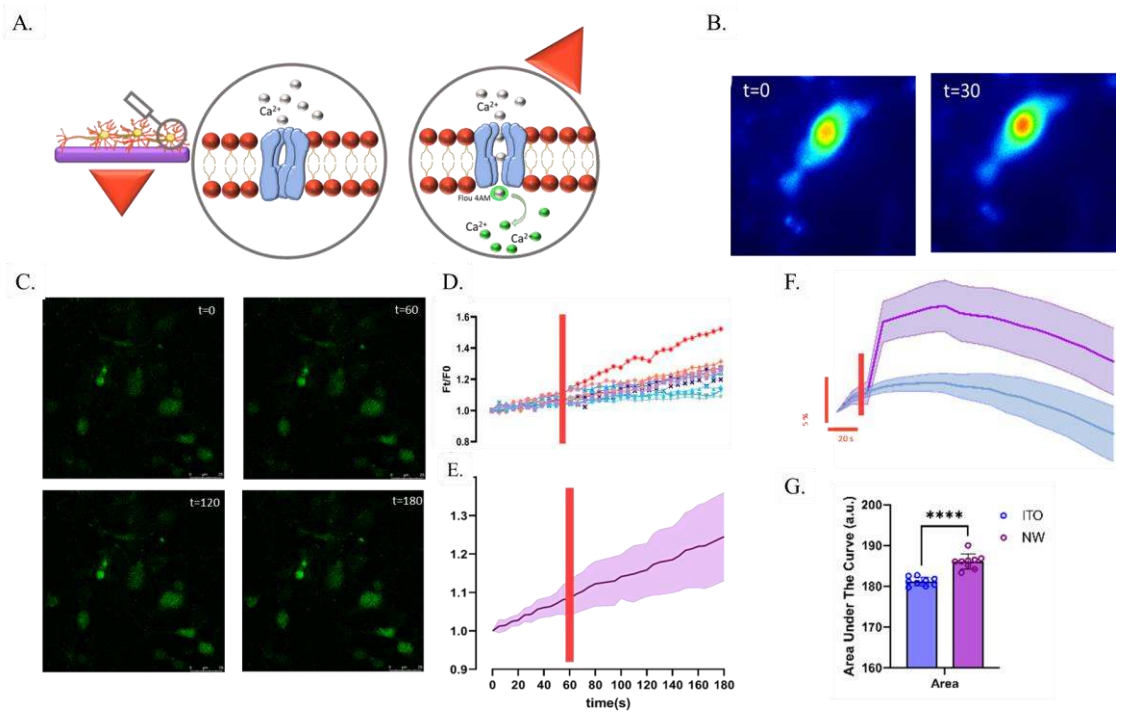

Figure 3.25 Calcium signal traces (Ft/F0) of randomly selected neurons before, during, and after light illumination. A. Schematic representation of calcium release under illumination. B. Calcium release of single neuron cultured on biointerface after 780nm light stimulation (stimulus frequency, 5 Hz; 20 ms pulse-width; light duration, 2s or 10s). C. Time dependent florescence intensity changes before and after illumination. D. Relative florescence intensity changes of selected cells on biointerface. E. Average of florescence intensity changes. F. Comparison of ITO control and the biointerface averaged florescence changes after 780nm light stimulation (stimulus frequency, 5 Hz; 20 ms pulse width; light duration, 2s). G. Area under the curve of graph F.

3.4.4 Ex vivo Retina stimulation through ITO/ZnO NW/$AgBiS_2$ NC/P3HT:RuO_2 Biointerface

Before retina experiments, light response (noise due to only light) was measured with MEA electrodes. 850 nm near-infrared light was used for initial light illumination experiments. Only light with maximum power showed -20-40mV photocurrent (Appendix C Figure 8.1). It is important to distinguish signals coming from cells and artifacts due to only light. The power that does not create background noise is

determined during recordings and 850 nm light illumination with 50% intensity shows no change in photovoltage and able to activate biointerface (Appendix C Figure 8.2). Then photocurrent of a small piece of biointerface with area of 4 mm^2 was recorded with the system and current generation upon light stimulation was observed (Appendix C Figure 8.3). Retina tissues were isolated from Dark Agouti rat to optimize newly built MEA setup. Since optimum culture condition for retina tissue is critical for getting good electrophysiology recordings; isolation timing, perfusion time, culture media temperature and recording duration is optimized.

Isolated retina was placed on the MEA array as retina ganglion cells towards the electrode array and photoreceptors towards to biointerface (Appendix C Figure 8.4). 78 electrode have active spikes over recording and the spontaneous activity of retinal ganglion cells, and how they react when stimulated by light, were successfully recorded. To minimize the negative effect of the device's thickness, which may cause adverse effects on the retina during prolonged recordings, leading to a decrease in spontaneous spiking rates over time, we have designed various tissue holder structures to optimize the interaction between the device and the retina.

To evaluate light and biointerface stimulation in a blind eye model, the MEA recording team from The Institute de la Vision Paris, including researchers Dr. Antoine Chaffiol and Corentin Joffrois, conducted similar measurements on blind rats with retinal dystrophy. Sustained spontaneous activity was recorded after the retinal tissue was positioned between the biointerface and the MEA surface. Recordings were performed using the retinas of P23H retinal degeneration blind rat model under 880 nm near-infrared (NIR) laser illumination at 5 Hz, with of 5, 10, 20, and 50 ms pulse durations, and a power intensity of ~5 $mW \cdot mm^{-2}$ for 100 repetitions.

In the measurements, active responses were obtained from approximately 100 of 256 electrodes. Half of this active response comes from the device activation under light illumination. In detail, in 5 ms 5 Hz light stimulation, RGCs at 41 of 95 (43.2 %) active electrodes responded to light stimulation; in 10 ms 5 Hz light stimulation, 38 of 76 (50 %) active electrodes responded to stimulation (Figure 3.26).

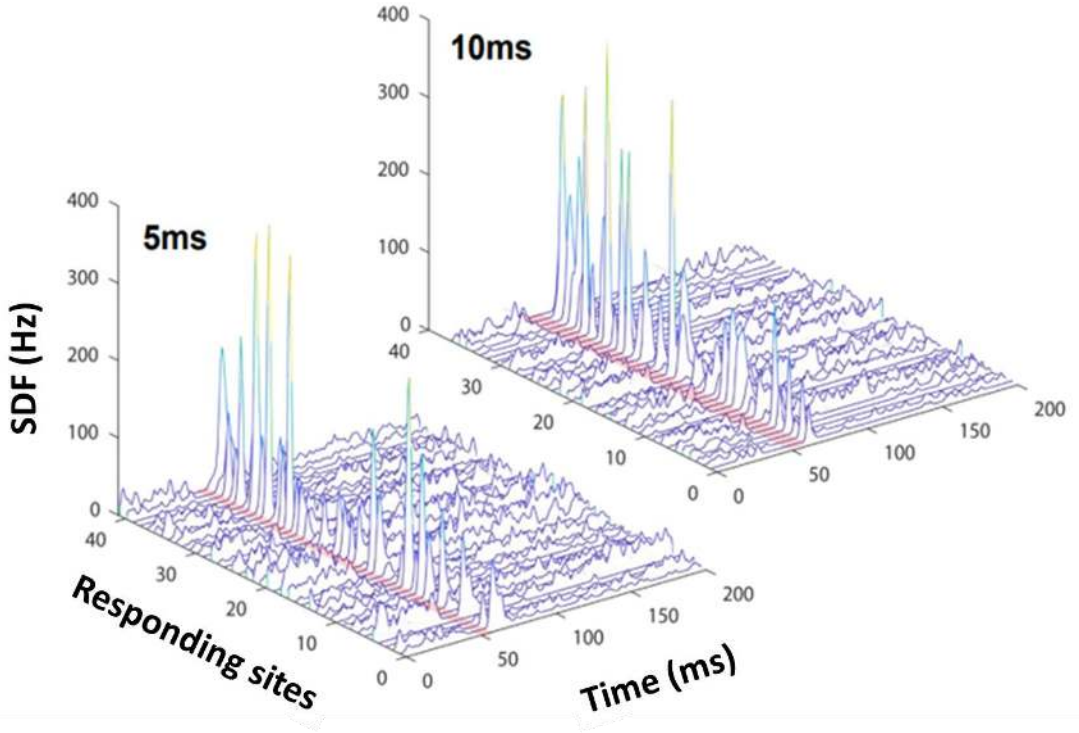

Figure 3.26 Light responsive electrodes during recording and their firing rate peaks at 5 and 10 ms pulse width. Red area indicated as 880 nm near-infrared (NIR) laser illumination pulses with 5 Hz frequency, 5 or 10 ms durations, ~5 mW/mm^2 power intensity for 100 repeats.

When the obtained results were evaluated among those responding to light stimulation, an average spike profile of around 100 Hz was obtained in both stimuli, as indicated in Figure 3.27. Due to high photovoltage value generated in biointerface under light illumination, the signals on lightening duration was shown as dashed lines without any spike form. The spikes before and after the light illumination were taken into measurements.

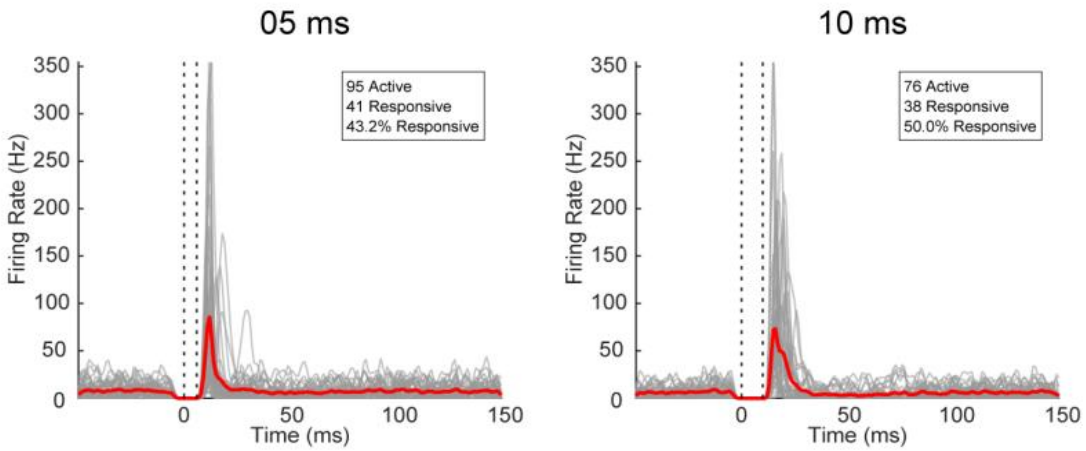

Figure 3.27 Averaged firing rate peaks of 5 ms and 10 ms light durations and RGC response during recordings. Spontaneous activity was indicated in graphs as active electrode while light stimulation generated response indicated as responsive electrode.

In 20 ms 5 Hz light stimulation, 44 of 97 (45.4 %) active electrodes responded to light stimulation; while in 50 ms 5 Hz light stimulation, 27 of 98 (27.6 %) active electrodes responded to stimulation (Figure 3.28). An average spike profile was found around 100 Hz was obtained in 20 ms while it reduced to 50 Hz in 50 ms stimulation duration (Figure 3.29).

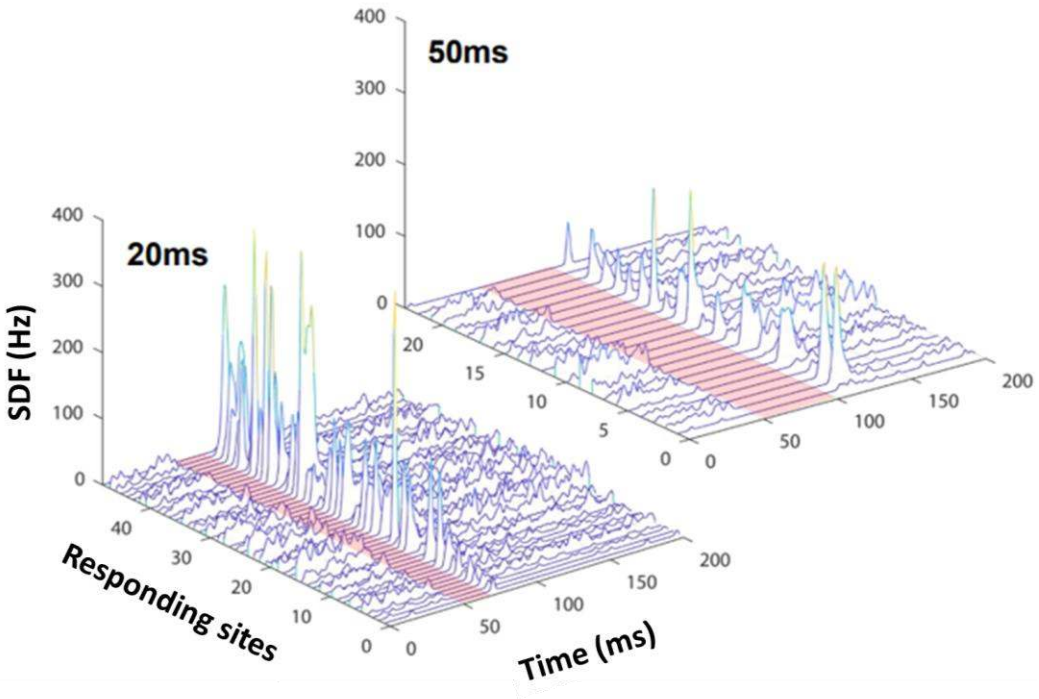

Figure 3.28 Light responsive electrodes during recording and their firing rate peaks at 20 and 50 ms pulse width. Red area indicated as 880 nm near-infrared (NIR) laser illumination pulses with 5 Hz frequency, 20 or 50 ms durations, ~5 mW/mm^2 power intensity for 100 repeats.

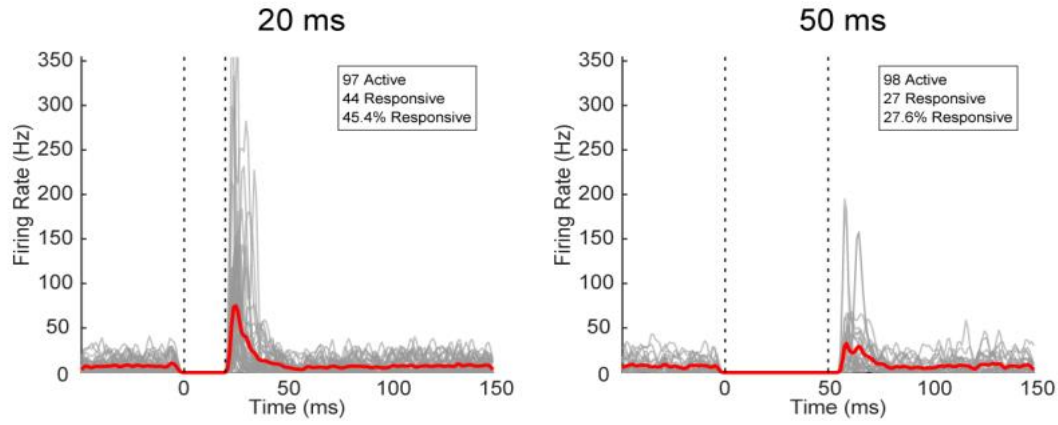

Figure 3.29 Averaged firing rate peaks of 20 ms and 50 ms light durations and RGC response during recordings. Spontaneous activity was indicated in graphs as active electrode while light stimulation generated response indicated as responsive electrode.

Firing rates of RGCs with different light durations showed slight but not significant increase from 5 ms to 20 ms and decrease with 50 ms ON duration. For obtaining better RGCs spike rates, 10 ms or 20 ms pulse widths are more suitable with biointerface activation (Figure 3.30). Also peak response latency was calculated however it could not show the spikes during stimulation due to high level of artifacts coming from biointerface.

Additional to retina with biointerface recordings, light illumination and RGC activity from retina without biointerface were also measured as a negative control (Figure 3.31). Firing rates without biointerface are significantly lower than RGC activity recorded with the biointerface. These results highlight the promise of $AgBiS_2$ based photovoltaic platforms for safe and effective use in neural prosthetics and vision restoration therapies.

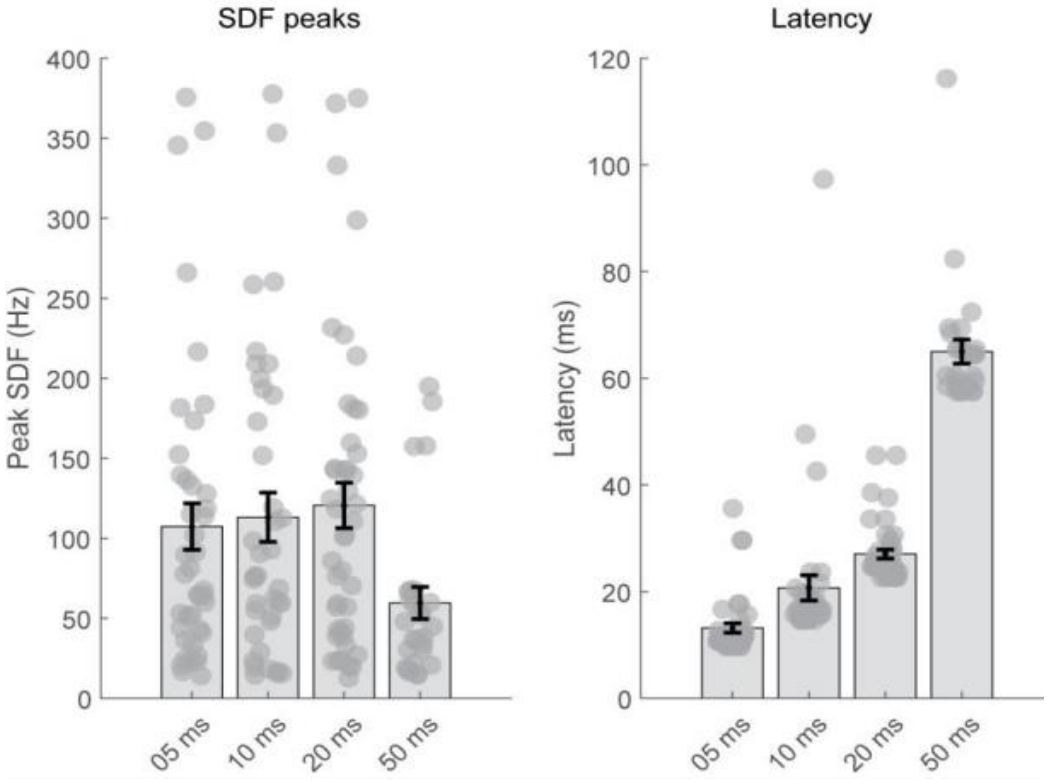

Figure 3.30 Comparison of averaged firing rate peaks of 5, 10, 20 and 50 ms light durations and latency during recordings.

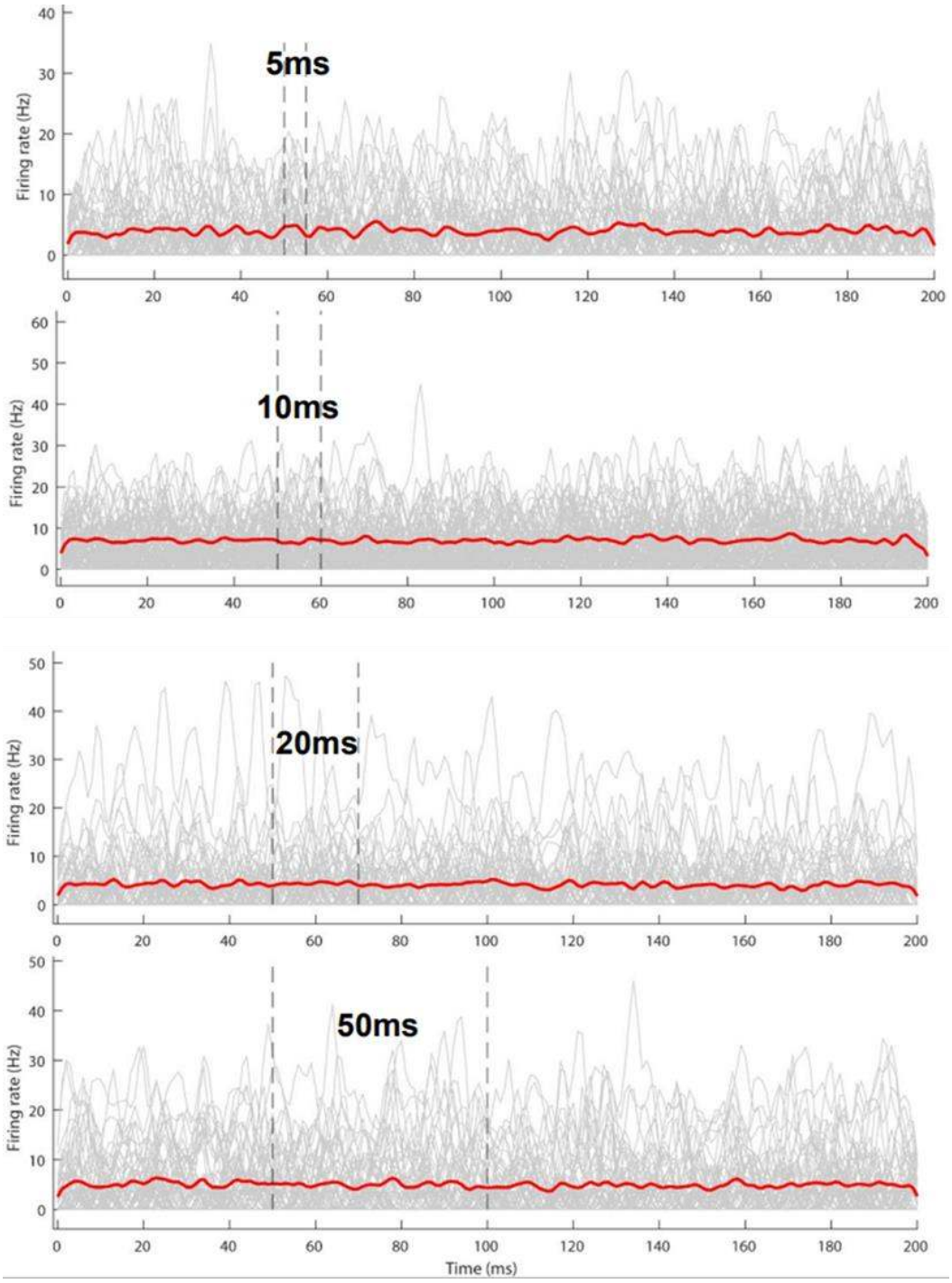

Figure 3.31 Averaged firing rate peaks of RGC response during 5, 10, 20 ms and 50 ms light durations at 5 Hz without active device.

3.5 A Preliminary Study to Determine ONC Injury Duration and Degree of Gliosis

Full text prepared with permission from Kaleli HN, et al. (2025) (Kaleli et al., 2025)
"**Kaleli HN**, Kesim C, Hasanreisoğlu M. Optic Nerve Damage Model: A Preliminary Study to Determine Injury Duration and Degree of Gliosis. Acta Ophthalmologica. 2025 Jan; 103(S284)."

3.5.1 Background

Although research into the cellular and molecular factors that contribute to optic nerve injury field is expanding, there is yet no treatment that can completely eliminate the structural and functional effects of the damage. Steroid based drugs or antibiotics are used to reduce inflammation and risk of infection to reduce pain and progress of vision loss. Therefore, there is a need for innovative treatment methods that can provide solutions to improve neuroregeneration after the optic nerve injury. Since the devices we have developed are sensitive to NIR light with high tissue penetration, they may be good candidates for improving neuroregeneration with optoelectronic stimulation in cases of subcutaneous neural injuries. For this reason, the final part of the thesis focuses on optimizing the duration of *in vivo* optic nerve damage prior to testing the fabricated biointerface on the injured area in future researches.

As stated in the procedure, lateral canthotomy and lateral bulbar conjunctiva incision were carried out to manage optic nerve injury. The lateral rectus muscle was removed in order to reach the retrobulbar region. In our ONC model, intraorbital portion of the optic nerve was compressed for the process. It was crushed for 15 seconds, 30 seconds, and 120 seconds. Daily checks were provided after the operation to observe tissue repair and the visible changes on eye (Figure 3.32). There were not observable changes on experimental eye of 15 sec ONC and 30 sec ONC group however in the 120 sec ONC group, there was a progressive opacity and edema that occurred from the second day and the increase in vascularization continued a week. The experimental period of 120 sec ONC group was discontinued and the eyes were isolated by sacrificing animal with inhalation of CO_2 after ERG and VEP-EEG measurements under anesthesia.

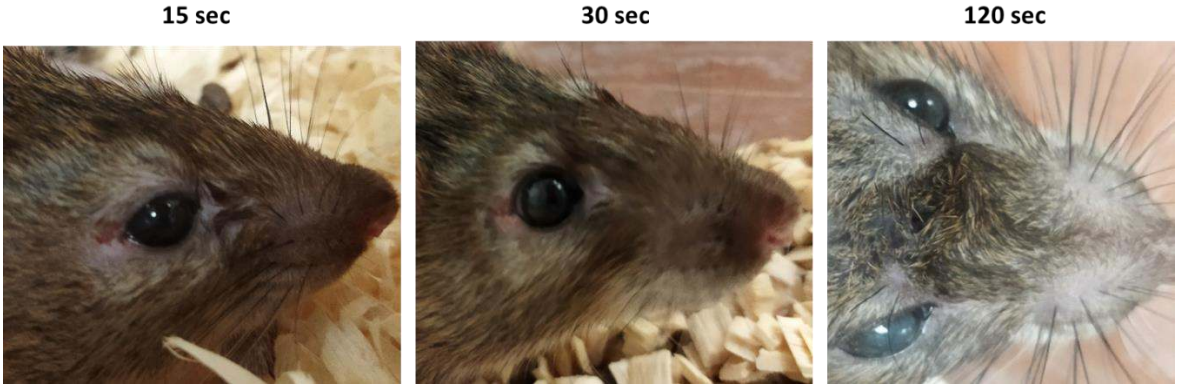

Figure 3.32 Right eyes with ONC during the one-week recovery period after injury operation.

3.5.2 ERG and VEP-EEG measurements

Under anesthesia, ERG measurements were recorded from the dark-adapted animals. Using a needle electrode, the grounding electrode was positioned under the rat's tail skin, also reference electrode was positioned on cornea. To reduce the background noise, a Faraday cage was placed around the system. In order to apply pulsed light in the ERG procedure, 500 $\mu W/cm^2$ of daylight was used at 1 Hz.

To evaluate the effects of optic nerve damage on retinal function, ERG tests were conducted. In ERG waveforms, a-wave represents photoreceptor function, while b-wave indicates bipolar interneurons. Photoreceptor dysfunction indicates a decline in a-wave amplitude, while inner retinal layer dysfunction is shown by a decrease in b-wave amplitude. In both cases, the decrease in amplitude may be related to disruption in retinal function. Based on the data given in Figure 3.33, it was observed that as the duration of optic nerve damage increased, the response to light in both a-wave and b-wave decreased in the ONC groups compared to the control.

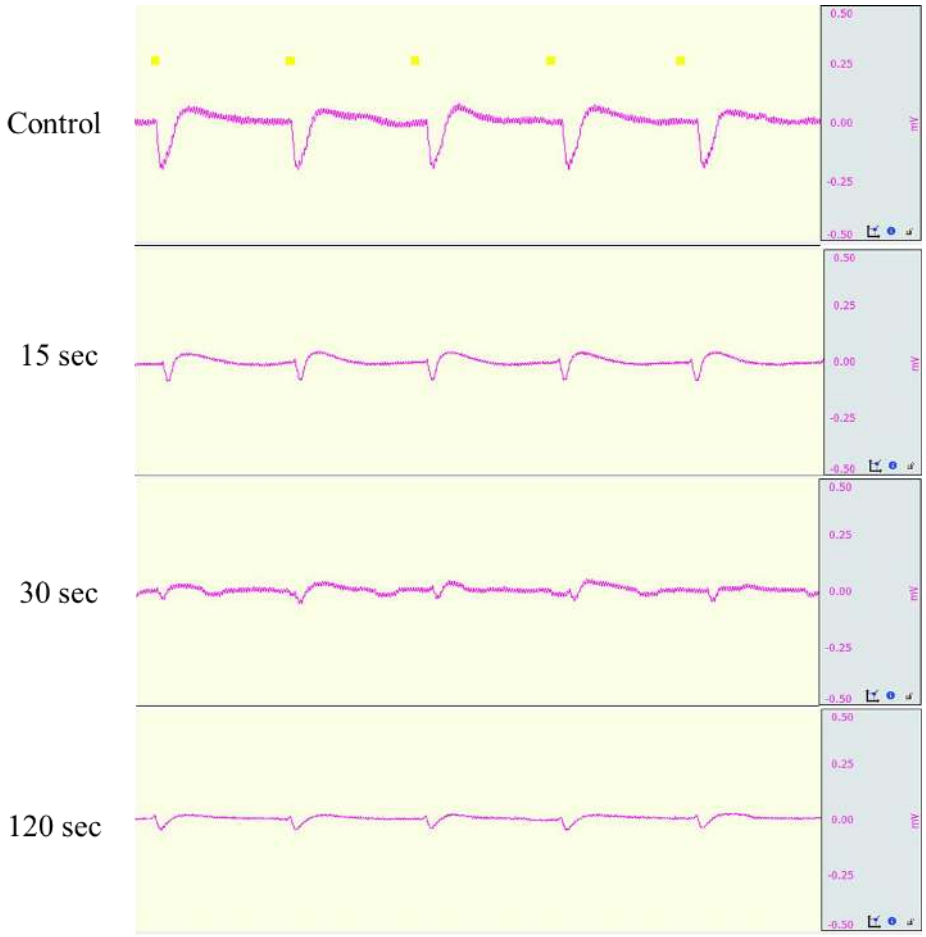

Figure 3.33 . ERG measurements in the Dark Agouti rat retina under 1 Hz frequency with 20 ms pulse width of white LED light stimulation at 500 µW/cm^2 light intensity. Pulsed lights are expressed as yellow dashes.

To demonstrate how visual signals from retina to brain functions and assess the amount of electrical impulses generated in visual cortex in relation to light stimuli, we implanted electrodes on the visual cortex of animals for the VEP-EEG procedure. During recovery period after the surgery, some of the electrodes on the skulls of the animals fell off. Although, some of the electrodes seen in the skin were not penetrated in skull and moving. The diameter of the electrodes used in the experiment, the size of the drill bit, and the fixation material applied after the surgery were not considered suitable for long-term procedures. Only significant results were obtained for the

control and 120 sec ONC groups (Figure 3.34) while other groups could not be included in the functional examining of VEP-EEG test.

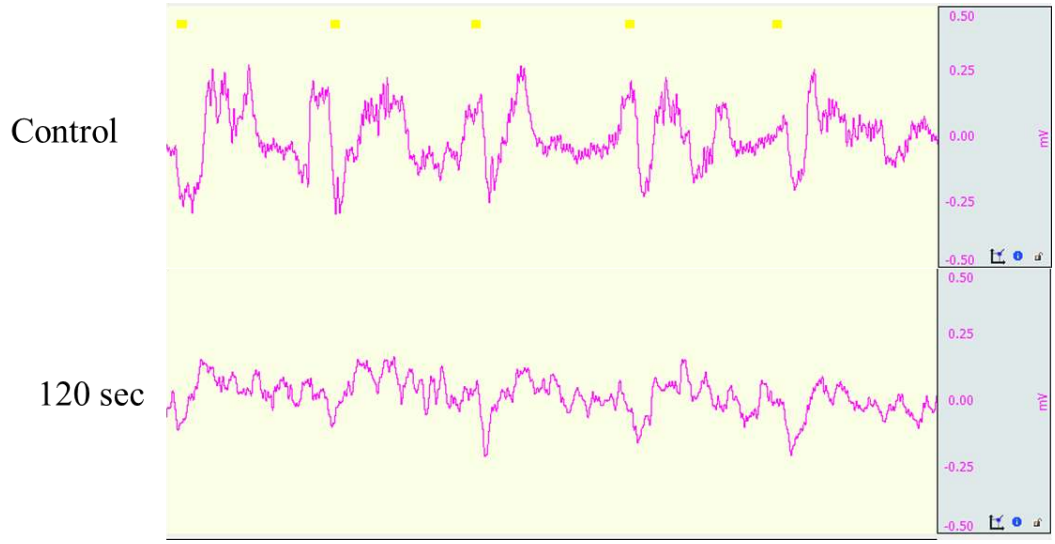

Figure 3.34 VEP-EEG measurements in the control and 120 sec ONC group under 1 Hz frequency with 20 ms pulse width of white LED light stimulation at 500 µW/cm^2 light intensity. Pulsed lights are expressed as yellow dashes

3.5.3 Histological Evaluation of Tissue Sections

Between the control and injured eyes, hematoxylin and eosin staining demonstrated significant alterations in the cellular organization of retinal layers and optic nerve tissue (Figure 3.35). The severity of the damage was particularly evident in the 120 sec ONC group. The natural architecture of the retina was disrupted, with degeneration leading to increased vascularization and hemorrhaging, as indicated by the red arrows. In the 120-second injury group, the main retinal layers were no longer distinguishable. In contrast, the progression of retinal damage was less observable in the 15 sec ONC group compared to the 30 sec ONC group and 120 sec ONC group, reflecting a duration-dependent effect of optic nerve injury.

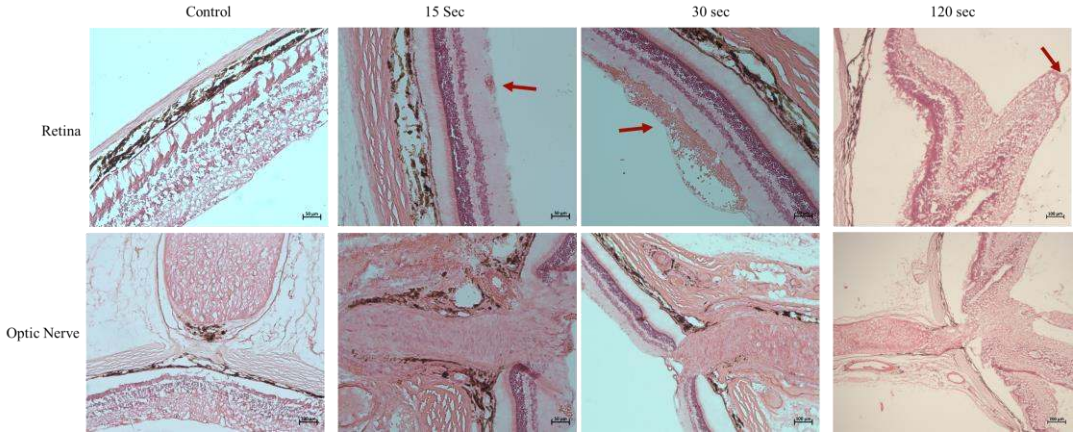

Figure 3.35 Hematoxylin and eosin-stained images of control and damaged Dark Agouti rat retina and optic nerve sections. Red blood cells represented as red arrows were observed in the injury groups (scale bar: 50µm).

Apoptotic cell level in the retinal layers was assessed using TUNEL-positive nuclei staining on retinal sections. An increase in TUNEL-positive cells was observed with increased injury duration, while no positive staining was detected in the retinal sections of the untreated control group (Figure 3.36). Retinal layer deformation and high cell death was observed in the 120 sec ONC group.

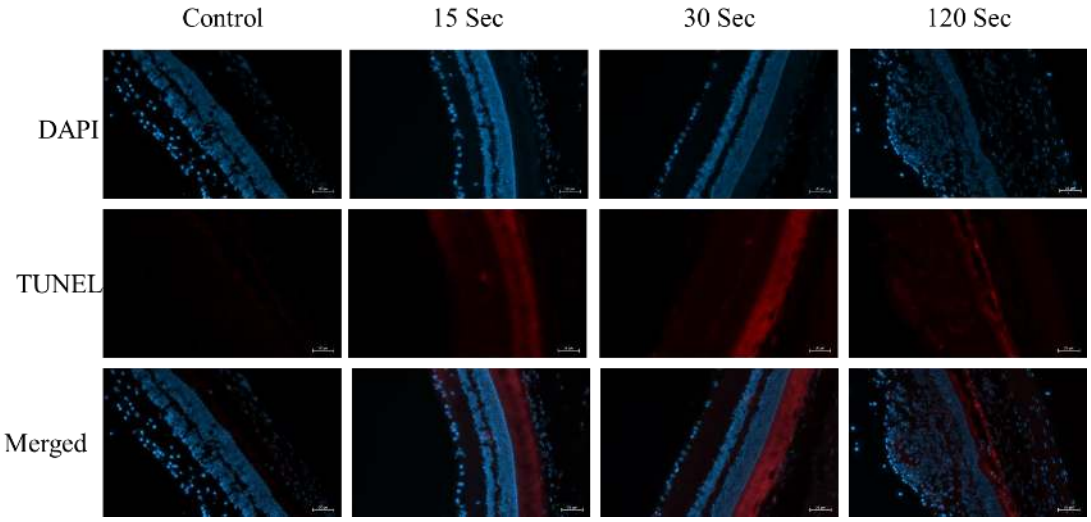

Figure 3.36 The progressive increase in apoptotic cells in response to the ONC injury. TUNEL stained cells (red) and DAPI nuclear marker (blue).

The structural alterations and cellular changes in ONC model, immunofluorescence staining for specific cell markers as NeuN for neuronal nuclei; GFAP for active Müller cells and astrocytes; Glutamine Synthetase for Müller glia; Vimentin for active Müller glia and fibroblasts; and Rhodopsin for photoreceptor cell markers were studied.

GFAP was found highly expressed in damaged groups compared to the control showing the accumulation of both active Müller glia and astrocytes in retina and optic nerve in ONC groups (Figure 3.37).

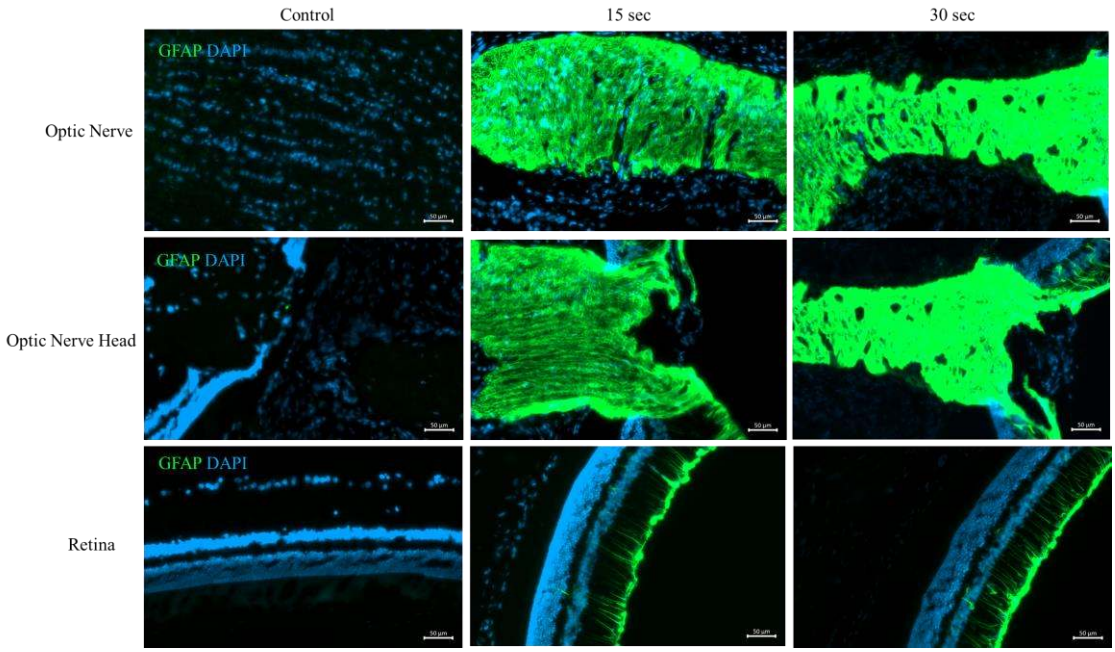

Figure 3.37 Immunofluorescence staining of control 15 sec and 30 sec ONC rat retinas and optic nerve. Tissue sections were stained with the glial cell marker, GFAP (green), and the cell nuclear marker, DAPI (blue).

Glutamine synthetase expression was increased with injury duration and advanced expression was found the area where the RGC layer is located in 30 sec ONC, indicating active retinal gliosis. Irregular Müller glia localization is visible in inner layers. Also under ONC, it is observed that retinal fibrosis occurs due to the disruption

of the healthy retinal layer and blood vessels, and thus the fibrous tissue extends from the outer surface to the inner surface of the retina.

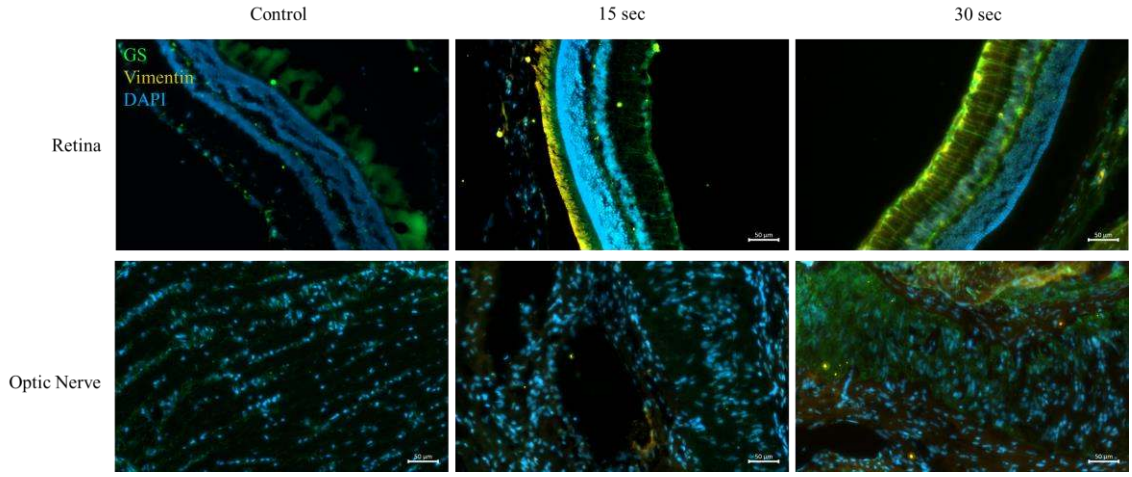

Figure 3.38 Immunofluorescence staining of control, 15 sec and 30 sec ONC rat retinas and optic nerve. Rat retinas and optic nerve were stained with the Müller cell indicator, glutamine synthetase (green), active Müller glia and fibroblast marker, Vimentin (orange), and the cell nucleus marker DAPI (blue).

Lastly, expression of rhodopsin and NeuN indicating photoreceptor and neurons were found decreased in 30 sec ONC group compared to untreated control and 15 sec ONC group (Figure 3.39).

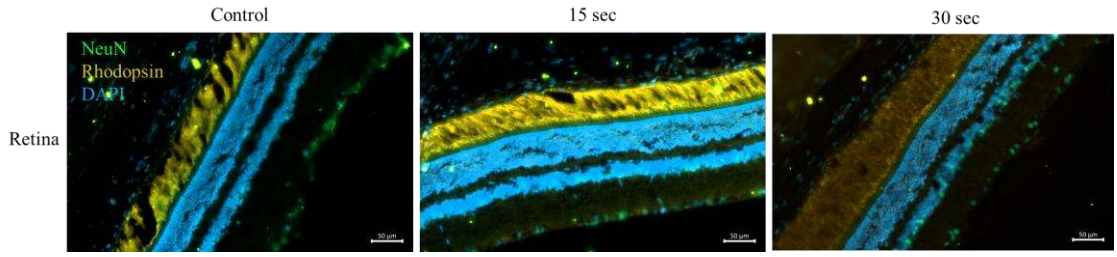

Figure 3.39 Immunofluorescence staining of control 15 sec and 30 sec ONC rat retinas. Rat retinas were stained with the photoreceptor cell marker, rhodopsin (orange), the ganglion cell marker, NeuN (green), and the cell nucleus marker, DAPI (blue). retinas.

4. CHAPTER 4

DISCUSSION

Implantable neural interfaces aim to provide solutions for neurodegenerative diseases. Localized and safe stimulation of neurons are important both as a research and therapeutic tools. Silicon bioelectronics (Huang et al., 2023), semiconductor nanocrystals (Marshall & Schnitzer, 2013), organic semiconducting polymers (Medagoda & Ghezzi, 2021), or inorganic biointerfaces (Jiang & Tian, 2018) are some of bioelectronic approaches that are currently available for appropriate neuronal response generation under illumination. It has been shown that nanocrystal-based biointerfaces can stimulate primary neurons (Han et al., 2021b) and explanted retina (Bareket et al., 2014). Flexible photovoltaic devices has high potential for clinical use in the future and there are several studies showed neural modulation both *in vitro* through cultured neurons and *in vivo*, including peripheral nerves (Silverå Ejneby et al., 2022), vagus nerve (Donahue et al., 2022) and the retina (Ferlauto et al., 2018).

The integration of optoelectronic devices into biological environments has raised several important questions over time. One key concern is the biocompatibility of the device's surface when in contact with cells or tissues. Since the initial introduction of solar cell-based electronics in biological applications, various bioelectronic devices have been developed for cellular stimulation. While successful excitation or inhibition of neurons via photomodulation has been achieved, thanks to the electrical properties and outstanding electrochemical characteristics of these devices, some of them include toxic or heavy metal based quantum dots, such as HgTe (Pappas et al., 2007), PbS (Karatum, Kaleli, et al., 2022a), CdSe (Lugo et al., 2012). These materials may create significant challenges for long-term usage due to their potential cytotoxicity of the release of mercury, lead or cadmium ions into the cellular environment.

Another important aspect is the type of photoelectrochemical currents generated during photostimulation. Faradaic and capacitive reactions are the two ways that the electrode and electrolyte interact (Merrill et al., 2005). In faradaic reactions between electrode and electrolyte, electrons are exchanged and causing simultaneous oxidation or reduction processes. In capacitive or non faradaic one, the mobility of charged ions drives the reaction in the electrolyte rather than the transport of electrons.

With minimizing chemical reactions on surface, the risk of chemical cytotoxicity decreased in capacitive current generation. Faradaic reaction may create more stable and high performance however electron transfers between the biointerface and the electrolyte may have impact on the biological environment through changing the pH and temperature. Outcome of the reaction may create irreversibly damage the cells. Apart from the potential damage to the neurons, the electron transfer reactions may cause disruption of the devices and its stability. Capacitive current generation is preferable for long term usages because it eliminates the risk of cellular damage due to chemical reactions on the device surface. For these reasons, photoelectrical stimulation needs to be preferred as capacitive to eliminate alteration in cellular metabolism.

Photovoltaic devices with organic materials offer very promising approaches in terms of high level interaction with living organisms. The fact that they are made of carbon polymers similar to biological macromolecules ensures high tissue biocompatibility. Organic semiconductor polymer-based neural interfaces have been demonstrated to photostimulate primary neurons and *ex vivo* retina, and create light sensitivity on blind retinas *in vivo* (Airaghi Leccardi et al., 2020; Ghezzi et al., 2011; Martino et al., 2013; Maya-Vetencourt et al., 2017; Medagoda & Ghezzi, 2021).

Savva A. et al.'s recent study showed the excitatory effects of the PDCBT-ITIC organic semiconductor on primary cortical neurons, attributed to its high Faradaic yield resulting from oxygen reduction reactions (Savva et al., 2023). To explore how light stimulates neurons through PDCBT-ITIC photochemical reactions, the researchers investigated HEPES buffer solutions and varying concentrations of H_2O_2 to assess oxygen reduction reactions. They proposed that light-induced chemical alterations in the

cell culture media, which interact with ROS and electrons from the active organic layer, are triggering neural activity.

In this thesis, the biocompatibility and activation tests of optoelectronic devices were conducted using various light sensitive materials, including the organic semiconductor P3HT:ITIC and different formulations of $AgBiS_2$-based nanocrystal biointerfaces, on neural cells. In the first part of the thesis, the biocompatibility of P3HT:ITIC device across primary neuron, primary astrocyte and Müller Glia cell types was indicated. P3HT:ITIC structure combines the strong absorption potential of P3HT in blue and green with the effective absorption potential of ITIC in the red and near infrared region, allowing to make photoactive stimulation devices to sensitive both visible and NIR light (Figure 3.1) with high potential for working under ocular safety limits.

The P3HT:ITIC biointerface has a non-toxic and heavy metal-free structure. As it is based on organic polymers and operates through a capacitive mechanism, it is considered biocompatible and safe for use in biological systems. The device has the potential to show an effective performance functionally as seen in the electrochemical measurements (Figure 3.2). Considering that the devices will be placed very close to the neurons as implants, we predict that this high photovoltage value formed on the surface will be at a level that can stimulate the neurons near the device without causing any light related thermal or photochemical damages. Also, the thin structure of device with thickness <200nm can minimize the risk of tissue damage by reducing mechanical stress applied to the retinal surface (Figure 3.3). All these advantages of P3HT:ITIC device created the starting point of our study.

We tested our device on both nervous and vision cells which are important for tissue-biointerface relation and any side effects as gliosis. In retina, Müller glia and astrocytes are responsible for tissue homeostasis in terms of maintaining structural, metabolic, and functional integrity. However, under pathological conditions, these cells can become activated and overexpress cytokines, leading to inflammation and scar formation at the tissue level. Therefore, under normal conditions, we investigated the viability of

astrocytes and Müller glia on the P3HT:ITIC biointerface. Dynamic regulation of cellular energy production, ATP, is crucial for maintaining healthy culture conditions, and this mechanism can be negatively affected in damaged cells and the release of lactate dehydrogenase (LDH) indicates cell membrane integrity. Both ATP generation and cell membrane integrity assays were used to evaluate viability, and it was discovered that more than 80% of cells were alive on the biointerface (Figure 3.4).

In addition to the viability assays, the morphological developments of the primary cells were examined in short and long term culture conditions (Figure 3.5). At Day 0 (DIV 5) and Day 14 (DIV 19), the cells were stained with their own biomarkers and visualized. Primary hippocampal neurons were stained with the neuronal nuclear protein NeuN and the general cytoskeletal protein F-actin. Synaptic network development was observed in cells cultured on both the ITO surface and the active device. After two weeks of culture, the neuronal survival rate was found to be similar to that of the control group. The survival status of astrocytes on the active device was also comparable to the control group, as confirmed by GFAP protein staining and both groups showed similar GFAP expression and cell proliferation patterns. Primary neurons and astrocytes maintained their cell specific structures throughout a 2-week culture period.

Müller cells are precursor cells for the maintenance of retinal cells and synthesize certain enzymes to eliminate waste neurotransmitters accumulated into the environment. Glutamine synthetase is an enzyme regulating the formation of glutamine by catalyzing the neurotransmitters. Müller cells are capable of converting glutamate and ammonia, which may be harmful to neurons, into the glutamine (Limb et al., 2002). While Müller cells take charge in a supportive role in the healthy retina, under injury or retinal degeneration, they can switch to an active form and cause irregular cellular distribution, migration to the neuron layer, and damage to intercellular connections (Agarwal et al., 2023; Zhao et al., 2024). The role of Müller cells in maintaining retinal health is critical both in healthy and diseased conditions, and it is important to evaluate biocompatibility of developed biointerfaces on Müller cells as well. In our first study, Müller glia cells cultured on the active device and control group showed similar morphological changes providing further biosafety of device in culture environment (Figure 3.6).

To confirm neuronal photostimulation, we evaluated the light dependent activation of neuronal cells cultured on P3HT:ITIC by calcium influx. Calcium plays a vital role in neurons by facilitating synaptic transmission by triggering neurotransmitter release for signal transduction. Elevated calcium levels in the synaptic cleft promote neurotransmitter release from vesicles, enabling effective synaptic communication. To monitor this process, the cells were labeled with the calcium indicator Fluo-4 AM and subsequently recorded. Primary hippocampal neuron activation on P3HT:ITIC devices was assessed under repetative near-infrared (NIR) light stimulation (Figure 3.1). Light stimulation induced an approximately 5% incline in calcium levels suggests the device is suitable for neuronal stimulation at certain levels, although higher activation levels were required for more responses.

The next step in the thesis focuses on a novel biointerfaces developed by quantum dots which are made from nontoxic materials with high absorption coefficient with absorption spectra in range between 400–1000 nm. This advancement aims to enhance the efficiency of neuronal stimulation by improved biointerface performance in further applications. Quantum dots (QDs) have been integrated into photovoltaic devices designed for neuronal stimulation (Han et al., 2021a; Karatum, Kaleli, et al., 2022b; Karatum, Yildiz, et al., 2022b). In these devices, QDs can convert photons into electron hole pairs then transfer those pairs in electrode-electrolyte for cell stimuli. Although heavy metal based QDs have high electrochemical features and possibility to activate neuronal cells, they are not suitable for long term usages. Therefore, the non-toxic and heavy metal-free QDs are favorable for photostimulation.

The electrochemical properties of InP QD-based biointerfaces was generated through type-I or type-II to enhance neural activation under blue visible light. Biocompatible devices allow the growth of PC12 cells (Bahmani Jalali et al., 2018) and induce light activated action potential in primary hippocampal neurons (Karatum et al., 2021). However, the redox reaction may create irreversible Faradaic reactions and cause cellular damage for long term photostimulation. Another promising QD for photovoltaic devices is AlSb QDs which generate capacitive current instead of irreversible Faradaic current with high biocompatible for neural stimulation (Han et al., 2021a). The

activation of the device with AlSb QDs occur under blue light below ocular safety limit. There is need for another type of material working under safe photostimulation reactions as well as under near-infrared light window with high tissue penetration and operating below the ocular safety limit.

Light in visible spectrum has tissue penetration with few millimeters. In contrast, NIR light has the highest penetration depth within centimeter range depending on tissue type as it can reach depths of up to 3cm in skull, skin and brain (Henderson & Morries, 2015; Jagdeo et al., 2012). Due to its ability to penetrate deeper retinal layers with minimal scattering and without causing significant damage, NIR light is better candidate for photostimulation and phototherapy in ophthalmology.

For achieving both good electrochemical properties and safe neuron stimulation we present a novel bioelectronic interface using $AgBiS_2$ QDs, which mediate pseudocapacitive interaction at the electrode-electrolyte interface and absorption spectra from visible to NIR (Bernechea et al., 2016; Onal et al., 2024) (Figure 3.8). The device is designed with 2/3 of area made up of ITO/ZnO/$AgBiS_2$/P3HT as active layer and 1/3 of area made of ITO/RuO2 as return electrode. The return side of the active device provides generation of capacitive photocurrent described by our previous study (Karatum, Yildiz, et al., 2022b). High photocurrent and photovoltaic production of $AgBiS_2$ nanocrystals (NCs) were measured and $AgBiS_2$-fabricated devices showed good biocompatibility in cellular environment (Figure 3.9-13). Biocompatibility is a critical parameter for materials for long-term use in biological system and the preservation of cellular viability and functionality is very important during the biointerface applications in neuronal stimulation. Within the parameters of ocular safety, the device photostimulates primary hippocampal neurons through a capacitive current. It is the first heavy metal free, optoelectronic biointerface with $AgBiS_2$ nanocrystal structure functioning in NIR spectrum and offering a promising advancement for neural interfaces (Balamur et al., 2024).

To enhance current generation for neuronal stimulation while maintaining high biocompatibility, we designed a novel biointerface that integrates ZnO nanowires and $AgBiS_2$ nanocrystal. This biointerface was constructed as a photovoltaic nanoassembly

on an indium tin oxide (ITO), enabling safe and efficient photostimulation of neurons. Well-defined active layer composed of $AgBiS_2$ QDs on ZnO NWs and the presence of ZnO nanowires significantly increased the surface area-dependent current generation, as evidenced by our experimental results, demonstrating the effectiveness of this approach for enhancing neuronal photostimulation (Figure 3.14).

The biocompatibility of the ZnO nanowire (NWs) and $AgBiS_2$ quantum dot (QD)-based biointerface was evaluated through live and dead cell staining (Calcein-AM/PI) and showed that the biointerface supports cell survival at levels comparable to the ITO control. This indicates that the ITO/ZnO NW/ $AgBiS_2$ device design did not induce significant cytotoxicity (Figure 3.15).

Furthermore, the oxidative stress response, assessed using the H_2DCFDA indicator, showed no observable incline in intracellular ROS levels after light stimulation, even after prolonged exposure (10,000 cycles). This finding suggests that the ZnO NW and $AgBiS_2$ QD combination does not induce oxidative damage, a common concern in photoactive materials (Figure 3.16).

In addition to oxidative stress assessment, the mitochondrial status was observed using the JC-1 assay, which provided further evidence of the biointerface's biocompatibility. The stable JC-1 aggregate-to-monomer ratio before and after light stimulation indicates that mitochondrial membrane potential which is a critical marker of cellular energy homeostasis. The device does not disrupt energy metabolism, further supporting its potential for safe and long-term neuronal applications (Figure 3.17). Dynamic calcium imaging was performed to observe cellular stimulation under light. The results indicated a 5% increase in intracellular calcium levels upon light stimulation, demonstrating the device's effectiveness in cellular activation. Taken together, these findings highlight the biocompatibility of the ZnO NW/ $AgBiS_2$ QD biointerface, making high potential candidate for photostimulation applications for further studies (Figure 3.18).

After validating cellular stimulation and biocompatibility with ZnO nanowire and QD-based biointerfaces, we developed an enhanced design by a P3HT:$AgBiS_2$ layer with a ZnO nanowire interlayer and a RuO_2 return electrode. The addition of the RuO_2 layer

significantly enhanced the device's capacitive injection capacity, so increasing the capacitive current of the active device. This modification was designed to achieve superior performance and more effective neuronal stimulation in both cellular environments and *ex vivo* retina recordings under repetitive light illumination. Furthermore, the inclusion of the P3HT layer, as demonstrated in our previous study, significantly improved the efficiency and stimulation capacity of the device. Also, the RuO_2 return layer facilitates in a more than twofold increase in photocurrent compared to devices without return electrode (Figure 3.19).

To evaluate the biocompatibility and functional efficacy of the new device, we checked the viability of primary neurons, intercellular network formation, intracellular stress levels, and excitability capacity *in vitro*. The device demonstrated high biocompatibility, with primary neurons exhibiting sustained viability and maintaining healthy morphological characteristics throughout two weeks of culture period (Figure 3.20-22). Enhanced synaptic network formation indicates the device's capability to support synaptic connectivity during long period of culture. As in previous study, intracellular stress levels and mitochondrial membrane potential were assessed to identify repetitive light illumination effects on living cells. Herein, the enhanced photocurrent and electrophysiological characteristics of new device did not cause undesired outcomes and light stimulation remained within acceptable stress level, comparable to control conditions (Figure 3.23-24).

Functionally, the device achieved 20% neuronal stimulation, a significant improvement over previously reported designs (Figure 3.25). This enhanced stimulation highlights the ability of the modified biointerface to facilitate more efficient and reliable neuronal activation. High biocompatibility and enhanced stimulation capacity demonstrate the potential of newly design of ITO/ZnO NW/ $AgBiS_2$ QD/P3HT: RuO_2 for optoelectronic therapeutic approaches as neural and retinal prosthetics.

In the next stage, *ex vivo* retina stimulation was performed using the developed device. The retinas of P23H rats, a model for retinitis pigmentosa, which is characterized by progressive vision loss, were effectively stimulated, as evidenced by the recording of RGC’s responses using a multi-electrode array (MEA). Remarkably, the current study is

the first time showing the stimulation in a blind retina by providing significant evidence that ITO/ZnO NW/$AgBiS_2$ QD/P3HT:RuO_2 can induce neural activity in degenerated retinal tissues (Figure 3.26-30). This finding not only validates the functional capacity of the device but also highlights its potential for future applications in retinal prosthetics and vision restoration.

The retina processes visual information before sending it to the brain through the optic nerve. The optic nerve serves as a fundamental link between the retina and the visual cortex, the part of the brain responsible for processing visual information. From the retina, signals continue to be transmitted through optic nerve, optic tract, and lateral geniculate nucleus. The route proceeds through visual cortex by optic radiation. Signals related to saccadic eye movements and pupil reflexes are transferred to the pretectal nucleus and superior colliculus (SC).

Many ocular, neurological, and systemic disorders can cause disruption of optic nerve, rested in visual impairment (Pardue & Allen, 2018; Yu-Wai-Man, 2015). While vision problems due to lens or refractive errors can be corrected with glasses or surgery, diseases involving trauma, the optic nerve damage, glaucoma, ischemic optic neuropathy can cause vision loss due to nerve cell death if not treated immediately. In most optic nerve diseases, the damage mechanisms and pathophysiology are not fully known and are still being investigated in experimental animal models. Despite many questions that have not yet been answered, extensive research over the years has made great progress in understanding optic nerve diseases with experimental models focusing on different optic nerve injuries.

One of the animal models used to investigate the visual system and neuronal survival following degeneration is the optic nerve crush model (ONC). The literature has employed both direct and indirect ways of optic nerve damage. RGC degeneration after ONC is correlated with the forced applied and injury duration (Liu et al., 2020). For consistent results, instruments that apply constant force for desired duration are often preferred (Feng et al., 2010; Knöferle et al., 2010; Liu et al., 2020; Ohlsson et al., 2004; Sarikcioglu et al., 2007). This model is used in neuroprotection and neurostimulation

studies in glaucoma and many other optic nerve diseases (Dratviman-Storobinsky et al., 2008; Levkovitch-Verbin, 2004; Maeda et al., 2004; Morrison et al., 2011).

Restoring vision loss due to optic nerve damage is a difficult process that requires simultaneously dealing with many important and complex mechanisms as survival, nerve regeneration, neural transmission and vision rehabilitation (Fague et al., 2021; Newman et al., 2023). Innovative treatment methods can approach to solve the multifaceted problems of the disease including progressive cell death, induced inflammatory pathways, gliosis and fibrosis (Chiang et al., 2024; Mesentier-Louro & Liao, 2019; Mesentier-Louro et al., 2019; Srivastava et al., 2022). There are still needs for the treatment and rehabilitation of optic nerve neurodegenerative (glaucoma), traumatic or ischemic diseases. With working under near infrared light, our biointerfaces holds high potential to be used deeper tissue applications as optic nerve to investigate the neurostimulation properties of newly designed implants in the nerve damage model. For further examination of tissue repair after implantation, ERG and VEP-EEG measurements can provide observation of electric current triggered nerve fiber regeneration in vision recovery of damaged model after repetitive near infrared light. For this purpose, firstly the process of degeneration was studied on animal models with different injury duration process to be used further studies to evaluate the potential applications of the developed devices beyond retinal prostheses.

The final part of my thesis focused on an optic nerve damage model. Our initial study examined the duration of damage and the degree of gliosis in the retinal layers. Further studies are needed to evaluate the impact of an optoelectronic interface on neuroregeneration for comprehensive device validation on ONC regeneration. To develop the model, the optic nerves of rats with intact vision were injured manually using calibrated forceps for 15, 30 or 120 seconds. This approach allowed us to examine the changes occurring in retinal cells across varying degrees of injury and time intervals. The effects of the damage were assessed using multiple parameters, including cell viability, preservation of the intercellular network structure, glial cell responses, and neuronal functions, as measured through electroretinography (ERG). A detailed analysis of the biological responses of retinal cells, particularly in relation to the degree of damage, provided crucial insights. The results revealed a significant loss of retinal

layer integrity, increased gliosis and fibrosis, and a decline in retinal ganglion cell (RGC) activity with prolonged injury durations (Figure 3.33-39).

To evaluate the potential of prosthesis-based treatments following optic nerve damage, it is essential to ensure that retinal function is preserved at a treatable level. This study demonstrated the effects and extent of long-term trauma. Our findings suggest that damage induced for 15 seconds or less may be suitable for promoting neuron regeneration, as the retina maintains partial visual perception despite the injury. Under these conditions, retinal layers and structural integrity are preserved, and the level of gliosis may be mitigated with additional anti-inflammatory interventions. This study represents an important step toward both assessing performance of these devices *in vivo* in the further research and understanding retina cells' responses to repetitive light stimuli with optoelectronic biointerfaces in the optic nerve damage. To ensure more consistent model generation, a motorized system could be developed to minimize operational variability and to create a controlled injury. Additionally, designing flexible, stable, and tissue-compatible optoelectronic devices will be suitable for implantation in the optic nerve region. These devices should enable efficient light stimulation within the tissue environment, advancing their potential for clinical applications.

5. CHAPTER 5

FUTURE DIRECTIONS AND CONCLUSION

With the findings of this thesis, a platform for the development of potential quantum dot based implant for the treatment of retinal degeneration will be advanced, with *in vivo* testing planned for the next stages. Conventional electrostimulation devices currently require an external power source. In contrast, our implant, which were tested *in vitro* and *ex vivo* for its photostimulation capabilities, is providing a wireless platform. This design eliminates access to external batteries or power sources attached to the prosthesis. Although *in vivo* testing has not yet been performed, this comprehensive approach highlights the originality of the implant and its potential for practical application.

From a material perspective, the proposed device structures demonstrate sensitivity to the visible to near infrared light spectrum with cost effective material production in lab environment. Further studies will enhance its value compared to previous studies since the thesis demonstrated that the material can be developed into improved and more practical versions through different fabrication processes on the active layer structure. The structure of the presented implants produces a neural stimulation that can trigger action potential by depolarizing the neuron membrane potential through inducing a strong and harmless capacitive photocurrent on the neuron membranes. However, it should be noted that Faradaic currents, while capable of delivering higher charge density, may cause toxicity to cells due to byproduct generation, therefore making capacitive currents is more suitable and safer choice for long-term stimulation applications.

Near infrared light stimulation has been shown through multi electrode array measurements, to successfully induce stimulation in retinal ganglion cells in the damaged retina using our quantum dot based photovoltaic devices. In addition to the preliminary cellular and *ex vivo* optimization process for *in vivo* studies, the elasticity, flexibility, and stability of the photovoltaic device should also be considered. For curved surfaces such as the eye and optic nerve, structures with morphological characteristics are important for the targeted implantation area and tissue-implant compatibility. In order to ensure the continuity of communication between cells and to mimic the environment as normal physiological conditions, it is important to design structures for animal models that will not block the flow of nutrients and oxygen travel. Retinal prosthesis aims to improve low visual acuity caused by retinal degeneration, so that stimulation can be targeted at the individual cell level with quantum dot based photovoltaic devices with pixelated fabrication.

In the future, when designing photovoltaic structures containing quantum dot particles such as $AgBiS_2$, some points should be considered in cell culture. The developed device without any toxic ingredient allows cells to be grown in a healthy way and provides preliminary data to be obtained for tissue-device compatibility. While the biocompatibility of the materials is the first thing to consider to prevent any adverse effects, there are other check points to be considered such as surface properties, surface roughness, hydrophilicity, pH and surface charge. Surface properties including topography and chemistry are an optimization process frequently encountered in *in vitro* conditions before tissue tests. Additionally, adhesion capabilities of adherent cells as neurons on hydrophobic surfaces may decrease due to the force applied in the opposite direction. In these cases, there are different methods that can be applied according to the characteristics of the device, such as O_2 plasma, UV treatment, overnight incubation in water or H_2O_2 plasma sterilization. Surface pH is another factor affecting cell adhesion and it is very important to provide a physiological environment with a pH value of 7-7.4. Additionally, since outer surface of cell membrane is negatively charged, the positively charged culture surface significantly affects the adhesion and cellular

development profiles of the cells. For this reason, the use of surface coating agents as extracellular matrix, PLL, PDL, matrigel, or laminin at an appropriate concentration, that will not affect the performance of the device and will increase cell adhesion, can be considered in the culture conditions.

6. Appendix A
List of Materials

Table 6.1Cell Culture Solutions & Reagents

Cell Culture Reagents	Manufacturer / Cat No
Dulbecco's Modifed Eagle's Medium	Multicell 319005
Neurobasal Plus Medium	Gibco A3582901
DMEM-F12	Multicell 319085
B27 supplement	Gibco 17504 100mL
Fetal Bovine Serum (FBS)	Biowest S160H-500
Trypsin-EDTA (0.5 mM EDTA, 0.25% Trypsin)	Multicell 325-542
Phosphate Buffer Saline	Biowest L0615-500
N-acetyl-Lglutamic acid	Sigma Aldrich 855642-100mg
AraC	Sigma Aldrich C6645-100mg
Poly-L-Lysine	Sigma Aldrich P2658
Hoechst 33342	Thermo Scientific 62249
Ames Medium	Sigma Aldrich A1420-1L
Dnase-I	NeoFroxx 9003-98-9

Table 6.2 Antibodies for immunofluorescence staining

Antibody	Manufacturer / Cat No
GFAP	Abcam ab7260
NeuN	Abcam ab177487
Glutamine synthetase	Abcam ab64613
Rhodopsin	Abcam ab190307
FITC-conjugated Phalloidin	Sigma Aldrich P5282
Vimentin	Abcam ab92547
Anti-beta III Tubulin	Abcam ab18207
Alexa Flour (AF) 488 anti-mouse	Invitrogen A11029
AF 594 anti-mouse	Abcam ab150116
AF 488 anti-rabbit	Abcam ab150077
Cy3 anti-rabbit	Abcam ab6939
Cy3 anti-mouse	Abcam ab97035
AF 555 anti-rabbit	Abcam ab150078
AF 594 anti-rabbit	Abcam ab150080

Table 6.3 Assays and Kits

Kit	Manufacturer / Cat No
CellTiter Glo CTG Assay	Promega G7571
CytoSelect^{TM} LDH Cytotoxicity Assay	Cell Biolabs CBA-241
Cellular ROS Assay Kit	Abcam ab113851
TUNEL Assay Kit BrdU-Red	Abcam ab6110
Fluo-4 AM	Invitrogen F14201
Probenecid-water soluble	Invitrogen P36400
JC-1	Invitrogen A59688DJ
MTT	Invitrogen M6494

Table 6.4 Chemicals & Reagents

Chemical	Manufacturer / Cat No
Calcium chloride	Sigma Aldrich C1016
2-Mercaptoethanol	Gibco 21985-023
DMSO	Sigma Aldrich D2650
Sodium chloride	Isolab 969.036.1000
DAPI supplemented mounting medium	Abcam ab104139
HBSS 10X	X0510-500
Glycerol	Sigma Aldrich 15524
D-Glucose	Sigma Aldrich G8270
Live Cell Solution	Invitrogen A14291DJ
Potassium chloride	Sigma Aldrich 12636
Tween 20	Genaxxon Bioscience M3171
Triton-X100	Sigma Aldrich X100
Sodium Bicarbonate	Sigma Aldrich 31437
Ethanol	Isolab 920.026.2500
HCl	Sigma Aldrich 7102
Magnesium Chloride	Sigma Aldrich M8266

HEPES	Sigma Aldrich H6147
Superblock	ScyTek AAA125
Paraformaldehyde	Sigma Aldrich 158127
Mounting Medium with DAPI	Ibidi 50011
Hematoxylin	Merck 1.09249.2500
Eosine	HistoPlus HST-EOQ-1000
Entellan	Merck 107960
Xylene	VWR 28973.363
H2O2	Sigma Aldrich 18304
OCT (DdCryo)	DDK 22-118
Low profile microtome blades	Accu-Edge 4810
Superfrost Plus Adhesion Microscope Slides	Epredia J1800AMNZ

Table 6.5 Preparation of Solutions and Culture Media

Buffer/Solution	**Ingredients**
aCSF	HEPES-10mM KCl-3mM D-Glucose-10mM MgCl2-1mM CaCl2-2mM NaCl-140mM pH 7.4 w/ 1 M NaOH 290 mOsm
AMES medium	8.8g AMES powder 1.9g sodium bicarbonate 1L water with 100% CO2
Neurobasal Complete medium	Neurobasal Plus Medium 2% B27 Supplement 1% 100x L-glutamine 1% 100x Pen/Strep
Neurobasal Plating medium	100 ml NBM complete medium 10 µM β-Mercaptoethanol 25 µM Glutamatic acid
Neurobasal Inhibition medium	10 ml NBM complete medium 2 µM AraC
Transfer solution	1X HBSS 43.8 mM Sucrose % 100x Pen/Strep 33.3 mM D-Glucose

Table 6.6 List of Softwares

Name	Purpose
ImageJ	Image analysis
NeuroJ	Image analysis
GraphPad Prisim	Data analysis
Zen Blue 3.5 software	Image capturing & analysis
LASX software	Image capturing & analysis
AcqKnowledge software	ERG & VEP-EEG Data Recording & analysis

Table 6.7 List of Equipments

Equipment	Supplier
Synergy H1 Microplate Reader	Bio-Tek Instruments
Axio Observer Z1 inverted flourescence microscope	ZEISS
M780LP1 LED	Thorlabs
DC2200 LED Driver	Thorlabs
DMI8 SP8 confocal laser scanning microscope	Leica
Ti2-U inverted light microscope	Nikon
SMZ-445 Stereo microscope	Nikon
MEA2100-256 System	Multi Channel Systems (MCS)
256MEA100/30iR-ITO-pr	MCS
256MEA200/30iR-ITO-pr	MCS
Perfusion-Kit	MCS
MP160-System	BIOPAC
ERS100C amplifier	BIOPAC
red LED bulb	Philips
CM1950 cryostat	Leica
Superfrost Plus adhesion microscope slides	Epredia
DMiL upright light microscope	Leica

7. Appendix B
Ethical Committee Approvals

.

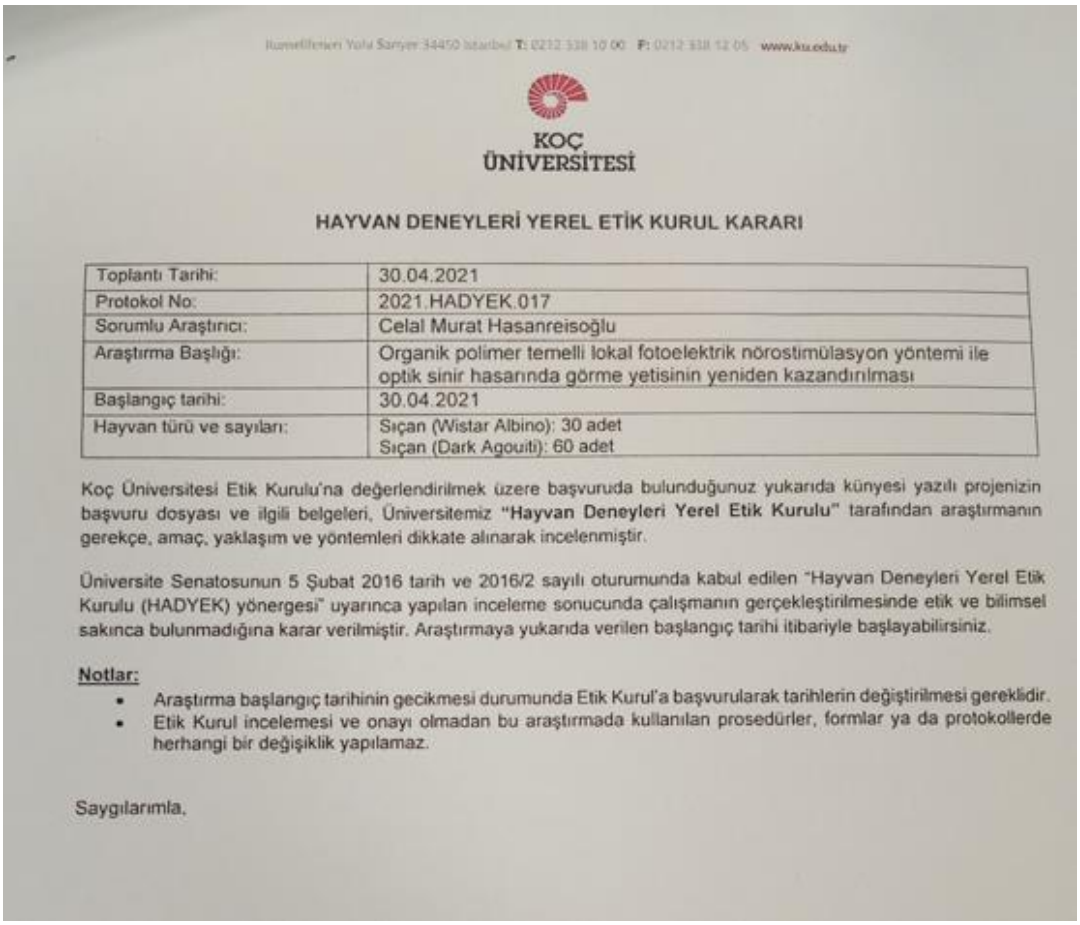

Rumelifeneri Yolu Sarıyer 34450 İstanbul T: 0212 338 10 00 F: 0212 338 12 05 www.ku.edu.tr

KOÇ
ÜNİVERSİTESİ

HAYVAN DENEYLERİ YEREL ETİK KURUL KARARI

Toplantı Tarihi:	30.04.2021
Protokol No:	2021.HADYEK.017
Sorumlu Araştırıcı:	Celal Murat Hasanreisoğlu
Araştırma Başlığı:	Organik polimer temelli lokal fotoelektrik nörostimülasyon yöntemi ile optik sinir hasarında görme yetisinin yeniden kazandırılması
Başlangıç tarihi:	30.04.2021
Hayvan türü ve sayıları:	Sıçan (Wistar Albino): 30 adet Sıçan (Dark Agouiti): 60 adet

Koç Üniversitesi Etik Kurulu'na değerlendirilmek üzere başvuruda bulunduğunuz yukarıda künyesi yazılı projenizin başvuru dosyası ve ilgili belgeleri, Üniversitemiz **"Hayvan Deneyleri Yerel Etik Kurulu"** tarafından araştırmanın gerekçe, amaç, yaklaşım ve yöntemleri dikkate alınarak incelenmiştir.

Üniversite Senatosunun 5 Şubat 2016 tarih ve 2016/2 sayılı oturumunda kabul edilen "Hayvan Deneyleri Yerel Etik Kurulu (HADYEK) yönergesi" uyarınca yapılan inceleme sonucunda çalışmanın gerçekleştirilmesinde etik ve bilimsel sakınca bulunmadığına karar verilmiştir. Araştırmaya yukarıda verilen başlangıç tarihi itibariyle başlayabilirsiniz.

Notlar:

- Araştırma başlangıç tarihinin gecikmesi durumunda Etik Kurul'a başvurularak tarihlerin değiştirilmesi gereklidir.
- Etik Kurul incelemesi ve onayı olmadan bu araştırmada kullanılan prosedürler, formlar ya da protokollerde herhangi bir değişiklik yapılamaz.

Saygılarımla,

Rumelifeneri Yolu Sarıyer 34450 İstanbul T: 0212 338 10 00 F: 0212 338 12 05 www.ku.edu.tr

KOÇ
ÜNİVERSİTESİ

HAYVAN DENEYLERİ YEREL ETİK KURUL KARARI

Toplantı Tarihi:	31.05.2021
Protokol No:	2021.HADYEK.022
Sorumlu Araştırıcı:	Sedat Nizamoğlu
Araştırma Başlığı:	Yakın Kızılötesi ve Görünür Işıkta Kuantum Nokta Temelli Fotoaktif Yüzeylerle Nöron ve Miyosit Uyarımı
Başlangıç tarihi:	31.05.2021
Hayvan türü ve sayıları:	Sıçan (Wistar Albino): 30 adet

Koç Üniversitesi Etik Kurulu'na değerlendirilmek üzere başvuruda bulunduğunuz yukarıda künyesi yazılı projenizin başvuru dosyası ve ilgili belgeleri, Üniversitemiz **"Hayvan Deneyleri Yerel Etik Kurulu"** tarafından araştırmanın gerekçe, amaç, yaklaşım ve yöntemleri dikkate alınarak incelenmiştir.

Üniversite Senatosunun 5 Şubat 2016 tarih ve 2016/2 sayılı oturumunda kabul edilen "Hayvan Deneyleri Yerel Etik Kurulu (HADYEK) yönergesi" uyarınca yapılan inceleme sonucunda çalışmanın gerçekleştirilmesinde etik ve bilimsel sakınca bulunmadığına karar verilmiştir. Araştırmaya yukarıda verilen başlangıç tarihi itibariyle başlayabilirsiniz.

Notlar:

- Araştırma başlangıç tarihinin gecikmesi durumunda Etik Kurul'a başvurularak tarihlerin değiştirilmesi gereklidir.
- Etik Kurul incelemesi ve onayı olmadan bu araştırmada kullanılan prosedürler, formlar ya da protokollerde herhangi bir değişiklik yapılamaz.

Rumelifeneri Yolu Sarıyer 34450 İstanbul T: 0212 338 10 00 F: 0212 338 12 05 www.ku.edu.tr

KOÇ
ÜNİVERSİTESİ

HAYVAN DENEYLERİ YEREL ETİK KURUL KARARI

Toplantı Tarihi:	17.04.2023
Protokol No:	2022.HADYEK.043
Sorumlu Araştırıcı:	Sedat Nizamoğlu
Araştırma Başlığı:	Retina Mesh Optoelektronik
Başlangıç tarihi:	17.04.2023
Hayvan türü ve sayıları:	Sıçan (Wistar Albino): 30 adet Sıçan (P23H): 12 adet Sıçan (Sprague Dawley): 12 adet Sıçan (RCS/Kyo): 12 adet Sıçan (Dark Agouti): 12 adet

Koç Üniversitesi Etik Kurulu'na değerlendirilmek üzere başvuruda bulunduğunuz yukarıda künyesi yazılı projenizin başvuru dosyası ve ilgili belgeleri, Üniversitemiz **"Hayvan Deneyleri Yerel Etik Kurulu"** tarafından araştırmanın gerekçe, amaç, yaklaşım ve yöntemleri dikkate alınarak incelenmiştir.

Üniversite Senatosunun 5 Şubat 2016 tarih ve 2016/2 sayılı oturumunda kabul edilen "Hayvan Deneyleri Yerel Etik Kurulu (HADYEK) yönergesi" uyarınca yapılan inceleme sonucunda çalışmanın gerçekleştirilmesinde etik ve bilimsel sakınca bulunmadığına karar verilmiştir. Araştırmaya yukarıda verilen başlangıç tarihi itibariyle başlayabilirsiniz.

Notlar:

- Araştırma başlangıç tarihinin gecikmesi durumunda Etik Kurul'a başvurularak tarihlerin değiştirilmesi gereklidir.
- Etik Kurul incelemesi ve onayı olmadan bu araştırmada kullanılan prosedürler, formlar ya da protokollerde herhangi bir değişiklik yapılamaz.

Saygılarımla,

8. Appendix C
Multielectrode Array Optimization

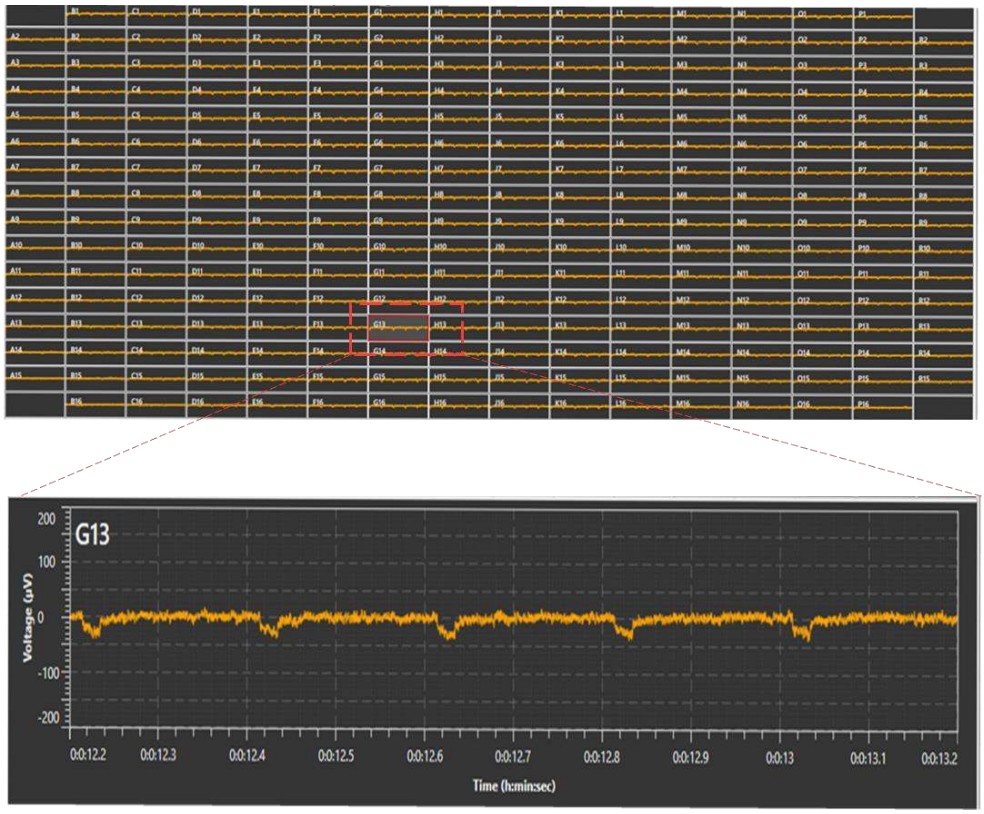

Figure 8.1 Measurement of photovoltage value of only 850 nm light with 100% power.

Figure 8.2 Measurement of photovoltage value of only 850 nm light with 50% power.

Figure 8.3 Measurement of photovoltage value of biointerface with MEA electrodes during 850 nm light illumination with 5 Hz frequency, 20 ms pulse and 50% intensity.

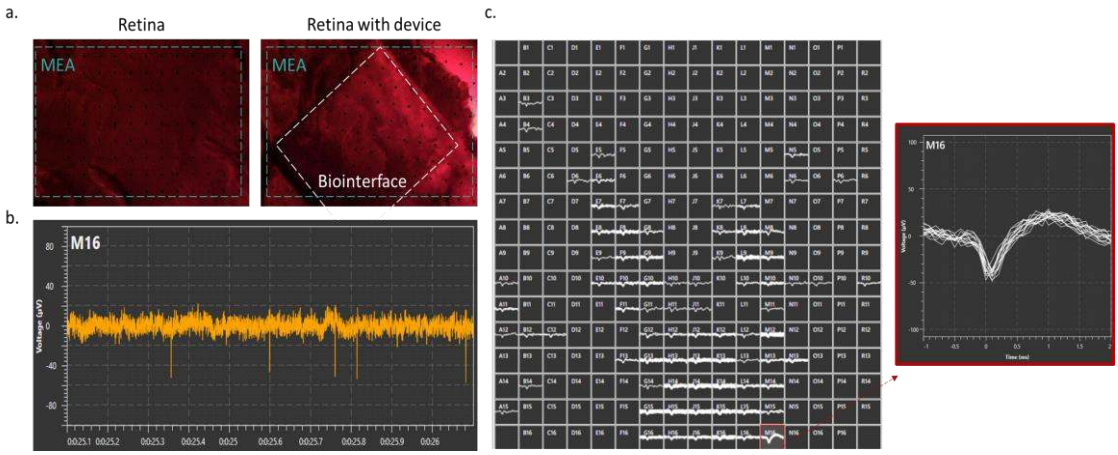

Figure 8.4 Retina recording with ITO/ZnO NW/AgBiS$_2$ NC/P3HT:RuO$_2$. A. retina on MEA electrode with and without bioinerface device (4 mm^2 in area). B. Spontaneous retina ganglion cell spikes at electrode M16. C. spike waveforms recorded from 256 individual electrodes, zoom in spike figure of electrode M16. d.Raster plot of 256 electrodes before and after 850nm light illumination with 5 Hz frequency, 20 ms pulse and 50% intensity.

9. BIBLIOGRAPHY

Acland, G. M., Aguirre, G. D., Ray, J., Zhang, Q., Aleman, T. S., Cideciyan, A. V., Pearce-Kelling, S. E., Anand, V., Zeng, Y., & Maguire, A. M. (2001). Gene therapy restores vision in a canine model of childhood blindness. *Nature genetics*, *28*(1), 92-95.

Agarwal, D., Do, H., Mazo, K. W., Chopra, M., & Wahlin, K. J. (2023). Restoring vision and rebuilding the retina by Müller glial cell reprogramming. *Stem cell research*, *66*, 103006.

Airaghi Leccardi, M. J. I., Chenais, N. A. L., Ferlauto, L., Kawecki, M., Zollinger, E. G., & Ghezzi, D. (2020). Photovoltaic organic interface for neuronal stimulation in the near-infrared. *Communications Materials*, *1*(1), 21.

Arevalo, J. F., Al Rashaed, S., Alhamad, T. A., Al Kahtani, E., & Al-Dhibi, H. A. (2021). Argus II retinal prosthesis for retinitis pigmentosa in the Middle East: The 2015 Pan-American Association of Ophthalmology Gradle Lecture. *International Journal of Retina and Vitreous*, *7*(1), 1-11.

Ayton, L. N., Barnes, N., Dagnelie, G., Fujikado, T., Goetz, G., Hornig, R., Jones, B. W., Muqit, M. M., Rathbun, D. L., & Stingl, K. (2020). An update on retinal prostheses. *Clinical Neurophysiology*, *131*(6), 1383-1398.

Ayton, L. N., Blamey, P. J., Guymer, R. H., Luu, C. D., Nayagam, D. A., Sinclair, N. C., Shivdasani, M. N., Yeoh, J., McCombe, M. F., & Briggs, R. J. (2014). First-in-human trial of a novel suprachoroidal retinal prosthesis. *PloS one*, *9*(12), e115239.

Bahmani Jalali, H., Mohammadi Aria, M., Dikbas, U. M., Sadeghi, S., Ganesh Kumar, B., Sahin, M., Kavakli, I. H., Ow-Yang, C. W., & Nizamoglu, S. (2018). Effective neural photostimulation using indium-Based type-II quantum dots. *ACS nano*, *12*(8), 8104-8114.

Bainbridge, J. W., Smith, A. J., Barker, S. S., Robbie, S., Henderson, R., Balaggan, K., Viswanathan, A., Holder, G. E., Stockman, A., & Tyler, N. (2008). Effect of gene

therapy on visual function in Leber's congenital amaurosis. *New England Journal of Medicine*, *358*(21), 2231-2239.

Balamur, R., Oh, J. T., Karatum, O., Wang, Y., Onal, A., Kaleli, H. N., Pehlivan, C., Şahin, A., Hasanreisoglu, M., & Konstantatos, G. (2024). Capacitive and Efficient Near-Infrared Stimulation of Neurons via an Ultrathin AgBiS2 Nanocrystal Layer. *ACS Applied Materials & Interfaces*.

Bareket, L., Waiskopf, N., Rand, D., Lubin, G., David-Pur, M., Ben-Dov, J., Roy, S., Eleftheriou, C., Sernagor, E., & Cheshnovsky, O. (2014). Semiconductor nanorod–carbon nanotube biomimetic films for wire-free photostimulation of blind retinas. *Nano letters*, *14*(11), 6685-6692.

Bernechea, M., Cates, N., Xercavins, G., So, D., Stavrinadis, A., & Konstantatos, G. (2016). Solution-processed solar cells based on environmentally friendly AgBiS2 nanocrystals. *Nature Photonics*, *10*(8), 521-525.

Bloomfield, S. A., & Dacheux, R. F. (2001). Rod vision: pathways and processing in the mammalian retina. *Progress in retinal and eye research*, *20*(3), 351-384.

Böhm, S., Splith, V., Riedmayr, L. M., Rötzer, R. D., Gasparoni, G., Nordström, K. J., Wagner, J. E., Hinrichsmeyer, K. S., Walter, J., & Wahl-Schott, C. (2020). A gene therapy for inherited blindness using dCas9-VPR–mediated transcriptional activation. *Science advances*, *6*(34), eaba5614.

Borda, E., Gaillet, V., Leccardi, M. J. I. A., Zollinger, E. G., Moreira, R. C., & Ghezzi, D. (2022). Three-dimensional multilayer concentric bipolar electrodes restrict spatial activation in optic nerve stimulation. *Journal of neural engineering*, *19*(3), 036016.

Brandstätter, J. H., Koulen, P., & Wässle, H. (1998). Diversity of glutamate receptors in the mammalian retina. *Vision research*, *38*(10), 1385-1397.

Bringmann, A., Grosche, A., Pannicke, T., & Reichenbach, A. (2013). GABA and glutamate uptake and metabolism in retinal glial (Müller) cells. *Frontiers in endocrinology*, *4*, 48.

Caspi, A., Barry, M. P., Patel, U. K., Salas, M. A., Dorn, J. D., Roy, A., Niketeghad, S., Greenberg, R. J., & Pouratian, N. (2021). Eye movements and the perceived location of phosphenes generated by intracranial primary visual cortex stimulation in the blind. *Brain stimulation*, *14*(4), 851-860.

Chawla, H., & Vohra, V. (2022). Polypoidal Choroidal Vasculopathy. In *StatPearls [Internet]*. StatPearls Publishing.

Chiang, B., Heng, K., Jang, K., Dalal, R., Liao, Y. J., Myung, D., & Goldberg, J. L. (2024). Development of a novel SupraChoroidal-to-Optic-NervE (SCONE) drug delivery system. *Drug Delivery*, *31*(1), 2379369.

Chow, A. Y., Chow, V. Y., Packo, K. H., Pollack, J. S., Peyman, G. A., & Schuchard, R. (2004). The artificial silicon retina microchip for the treatment of visionloss from retinitis pigmentosa. *Archives of ophthalmology*, *122*(4), 460-469.

Chuang, A. T., Margo, C. E., & Greenberg, P. B. (2014). Retinal implants: a systematic review. *British Journal of Ophthalmology*, *98*(7), 852-856.

Chui, T. Y., Song, H., & Burns, S. A. (2008). Adaptive-optics imaging of human cone photoreceptor distribution. *Journal of the Optical Society of America A*, *25*(12), 3021-3029.

Cornsweet, T. (2012). *Visual perception*. Academic press.

da Cruz, L., Dorn, J. D., Humayun, M. S., Dagnelie, G., Handa, J., Barale, P.-O., Sahel, J.-A., Stanga, P. E., Hafezi, F., & Safran, A. B. (2016). Five-year safety and performance results from the Argus II retinal prosthesis system clinical trial. *Ophthalmology*, *123*(10), 2248-2254.

Daiger, S., Sullivan, L., & Bowne, S. (2013). Genes and mutations causing retinitis pigmentosa. *Clinical genetics*, *84*(2), 132-141.

Dalkara, D., Goureau, O., Marazova, K., & Sahel, J.-A. (2016). Let there be light: gene and cell therapy for blindness. *Human gene therapy*, *27*(2), 134-147.

Deng, Y., Qiao, L., Du, M., Qu, C., Wan, L., Li, J., & Huang, L. (2022). Age-related macular degeneration: Epidemiology, genetics, pathophysiology, diagnosis, and targeted therapy. *Genes & diseases*, *9*(1), 62-79.

Dobelle, W. H. (2000). Artificial vision for the blind by connecting a television camera to the visual cortex. *ASAIO journal*, *46*(1), 3-9.

Donahue, M. J., Ejneby, M. S., Jakešová, M., Caravaca, A. S., Andersson, G., Sahalianov, I., Đerek, V., Hult, H., Olofsson, P. S., & Głowacki, E. D. (2022). Wireless optoelectronic devices for vagus nerve stimulation in mice. *Journal of neural engineering*, *19*(6), 066031.

Dratviman-Storobinsky, O., Hasanreisoglu, M., Offen, D., Barhum, Y., Weinberger, D., & Goldenberg-Cohen, N. (2008). Progressive damage along the optic nerve

following induction of crush injury or rodent anterior ischemic optic neuropathy in transgenic mice. *Molecular vision*, *14*, 2171.

Edwards, T. L., Cottriall, C. L., Xue, K., Simunovic, M. P., Ramsden, J. D., Zrenner, E., & MacLaren, R. E. (2018). Assessment of the electronic retinal implant alpha AMS in restoring vision to blind patients with end-stage retinitis pigmentosa. *Ophthalmology*, *125*(3), 432-443.

Euler, T., Haverkamp, S., Schubert, T., & Baden, T. (2014). Retinal bipolar cells: elementary building blocks of vision. *Nature Reviews Neuroscience*, *15*(8), 507-519.

Fague, L., Liu, Y. A., & Marsh-Armstrong, N. (2021). The basic science of optic nerve regeneration. *Annals of Translational Medicine*, *9*(15).

Feng, D.-F., Chen, E.-T., Li, X.-Y., Liu, Y., & Wang, Y. (2010). Standardizing optic nerve crushes with an aneurysm clip. *Neurological research*, *32*(5), 476-481.

Ferlauto, L., Airaghi Leccardi, M. J. I., Chenais, N. A. L., Gilliéron, S. C. A., Vagni, P., Bevilacqua, M., Wolfensberger, T. J., Sivula, K., & Ghezzi, D. (2018). Design and validation of a foldable and photovoltaic wide-field epiretinal prosthesis. *Nature communications*, *9*(1), 992.

Fleckenstein, M., Mitchell, P., Freund, K. B., Sadda, S., Holz, F. G., Brittain, C., Henry, E. C., & Ferrara, D. (2018). The progression of geographic atrophy secondary to age-related macular degeneration. *Ophthalmology*, *125*(3), 369-390.

Fujikado, T., Kamei, M., Sakaguchi, H., Kanda, H., Morimoto, T., Ikuno, Y., Nishida, K., Kishima, H., Maruo, T., & Konoma, K. (2011). Testing of semichronically implanted retinal prosthesis by suprachoroidal-transretinal stimulation in patients with retinitis pigmentosa. *Investigative ophthalmology & visual science*, *52*(7), 4726-4733.

Gaillet, V., Borda, E., Zollinger, E. G., & Ghezzi, D. (2021). A machine-learning algorithm correctly classifies cortical evoked potentials from both visual stimulation and electrical stimulation of the optic nerve. *Journal of neural engineering*, *18*(4), 046031.

Ghezzi, D., Antognazza, M. R., Dal Maschio, M., Lanzarini, E., Benfenati, F., & Lanzani, G. (2011). A hybrid bioorganic interface for neuronal photoactivation. *Nature communications*, *2*(1), 166.

Ghosh, K. K., Haverkamp, S., & Wässle, H. (2001). Glutamate receptors in the rod pathway of the mammalian retina. *Journal of Neuroscience*, *21*(21), 8636-8647.

Gill, J. S., Georgiou, M., Kalitzeos, A., Moore, A. T., & Michaelides, M. (2019). Progressive cone and cone-rod dystrophies: clinical features, molecular genetics and prospects for therapy. *British Journal of Ophthalmology*, *103*(5), 711-720.

GmbH, M. C. S. M. (2013). *MEA Application Note: Retina Recordings (MicroElectroretinograms)from Rattus norvegicus*. https://www.multichannelsystems.com/sites/multichannelsystems.com/files/documents/applications/MEA-Application%20Note_Retina.pdf

Grünert, U., & Martin, P. R. (2020). Cell types and cell circuits in human and non-human primate retina. *Progress in retinal and eye research*, *78*, 100844.

Güler, B. E., Krzysko, J., & Wolfrum, U. (2021). Isolation and culturing of primary mouse astrocytes for the analysis of focal adhesion dynamics. *STAR protocols*, *2*(4), 100954.

Han, M., Bahmani Jalali, H., Yildiz, E., Qureshi, M. H., Şahin, A., & Nizamoglu, S. (2021a). Photovoltaic neurointerface based on aluminum antimonide nanocrystals. *Communications Materials*, *2*(1), 1-10.

Han, M., Bahmani Jalali, H., Yildiz, E., Qureshi, M. H., Şahin, A., & Nizamoglu, S. (2021b). Photovoltaic neurointerface based on aluminum antimonide nanocrystals. *Communications Materials*, *2*(1), 19.

Han, M., Karatum, O., & Nizamoglu, S. (2022). Optoelectronic Neural Interfaces Based on Quantum Dots. *ACS Applied Materials & Interfaces*.

Han, M., Yildiz, E., Kaleli, H. N., Karaz, S., Eren, G. O., Dogru-Yuksel, I. B., Senses, E., Şahin, A., & Nizamoglu, S. (2022). Tissue-Like Optoelectronic Neural Interface Enabled by PEDOT: PSS Hydrogel for Cardiac and Neural Stimulation. *Advanced Healthcare Materials*, *11*(8), 2102160.

Hauswirth, W. W., Aleman, T. S., Kaushal, S., Cideciyan, A. V., Schwartz, S. B., Wang, L., Conlon, T. J., Boye, S. L., Flotte, T. R., & Byrne, B. J. (2008). Treatment of leber congenital amaurosis due to RPE65 mutations by ocular subretinal injection of adeno-associated virus gene vector: short-term results of a phase I trial. *Human gene therapy*, *19*(10), 979-990.

Henderson, T. A., & Morries, L. D. (2015). Near-infrared photonic energy penetration: can infrared phototherapy effectively reach the human brain? *Neuropsychiatric disease and treatment*, 2191-2208.

Hornig, R., Dapper, M., Joliff, E. L., Hill, R., Ishaque, K., Posch, C., Benosman, R., LeMer, Y., Sahel, J.-A., & Picaud, S. (2017). Pixium vision: first clinical results and innovative developments. In *Artificial Vision* (pp. 99-113). Springer.

Huang, Y., Cui, Y., Deng, H., Wang, J., Hong, R., Hu, S., Hou, H., Dong, Y., Wang, H., & Chen, J. (2023). Bioresorbable thin-film silicon diodes for the optoelectronic excitation and inhibition of neural activities. *Nature biomedical engineering*, *7*(4), 486-498.

Humayun, M. S., Dorn, J. D., Da Cruz, L., Dagnelie, G., Sahel, J.-A., Stanga, P. E., Cideciyan, A. V., Duncan, J. L., Eliott, D., & Filley, E. (2012). Interim results from the international trial of Second Sight's visual prosthesis. *Ophthalmology*, *119*(4), 779-788.

Humayun, M. S., Weiland, J. D., Fujii, G. Y., Greenberg, R., Williamson, R., Little, J., Mech, B., Cimmarusti, V., Van Boemel, G., & Dagnelie, G. (2003). Visual perception in a blind subject with a chronic microelectronic retinal prosthesis. *Vision research*, *43*(24), 2573-2581.

Ichinose, T., & Habib, S. (2022). ON and OFF Signaling Pathways in the Retina and the Visual System. *Frontiers in ophthalmology*, *2*, 989002.

Jacobson, S., Sumaroka, A., Luo, X., & Cideciyan, A. (2013). Retinal optogenetic therapies: clinical criteria for candidacy. *Clinical genetics*, *84*(2), 175-182.

Jagdeo, J. R., Adams, L. E., Brody, N. I., & Siegel, D. M. (2012). Transcranial red and near infrared light transmission in a cadaveric model.

Jiang, Y., & Tian, B. (2018). Inorganic semiconductor biointerfaces. *Nature Reviews Materials*, *3*(12), 473-490.

Kaleli, H. N., Karatum, O., Pehlivan, Ç., Kesim, C., Yıldız, E., Sahin, A., Nizamoğlu, S., & Hasanreisoğlu, M. (2024). P3HT: ITIC polymer based photovoltaic biointerfaces for neural photostimulation. *Acta Ophthalmologica*, *102*.

Kaleli, H. N., Kesim, C., & Hasanreisoğlu, M. (2025). Optic nerve damage model: A preliminary study to determine injury duration and degree of gliosis. *Acta Ophthalmologica*, *103*(S284). https://doi.org/https://doi.org/10.1111/aos.17075

Kameneva, T., Maturana, M., Hadjinicolaou, A., Cloherty, S., Ibbotson, M., Grayden, D., Burkitt, A., & Meffin, H. (2016). Retinal ganglion cells: mechanisms underlying depolarization block and differential responses to high frequency electrical stimulation of ON and OFF cells. *Journal of neural engineering*, *13*(1), 016017.

Karatum, O., Aria, M. M., Eren, G. O., Yildiz, E., Melikov, R., Srivastava, S. B., Surme, S., Dogru, I. B., Bahmani Jalali, H., & Ulgut, B. (2021). Nanoengineering InP quantum dot-based photoactive biointerfaces for optical control of neurons. *Frontiers in neuroscience*, 724.

Karatum, O., Kaleli, H. N., Eren, G. O., Sahin, A., & Nizamoglu, S. (2022a). Electrical Stimulation of Neurons with Quantum Dots via Near-Infrared Light. *ACS Nano*, *16*(5), 8233-8243. https://doi.org/10.1021/acsnano.2c01989

Karatum, O., Kaleli, H. N., Eren, G. O., Sahin, A., & Nizamoglu, S. (2022b). Electrical Stimulation of Neurons with Quantum Dots via Near-Infrared Light. *ACS nano*.

Karatum, O., Yildiz, E., Kaleli, H. N., Sahin, A., Ulgut, B., & Nizamoglu, S. (2022a). RuO2 Supercapacitor Enabled Flexible, Safe, and Efficient Optoelectronic Neural Interface. *Advanced Functional Materials*, 2109365.

Karatum, O., Yildiz, E., Kaleli, H. N., Sahin, A., Ulgut, B., & Nizamoglu, S. (2022b). RuO2 supercapacitor enables flexible, safe, and efficient optoelectronic neural interface. *Advanced Functional Materials*, *32*(31), 2109365.

Kim, T., Iseri, E., Peng, M. G., Medvidovic, S., Silliman, T., Pahlavan, P., Niu, G., Huang, C., Simonyan, A., & Pahnahad, J. (2025). Electric field stimulation directs target-specific axon regeneration and partial restoration of vision after optic nerve crush injury. *PloS one*, *20*(1), e0315562.

Kim, U. S., Mahroo, O. A., Mollon, J. D., & Yu-Wai-Man, P. (2021). Retinal ganglion cells—diversity of cell types and clinical relevance. *Frontiers in neurology*, *12*, 661938.

Kitiratschky, V. B., Stingl, K., Wilhelm, B., Peters, T., Besch, D., Sachs, H., Gekeler, F., Bartz-Schmidt, K. U., & Zrenner, E. (2015). Safety evaluation of “retina implant alpha IMS”—a prospective clinical trial. *Graefe's Archive for Clinical and Experimental Ophthalmology*, *253*(3), 381-387.

Klapper, S. D., Swiersy, A., Bamberg, E., & Busskamp, V. (2016). Biophysical properties of optogenetic tools and their application for vision restoration approaches. *Frontiers in systems neuroscience*, *10*, 74.

Knöferle, J., Koch, J. C., Ostendorf, T., Michel, U., Planchamp, V., Vutova, P., Tönges, L., Stadelmann, C., Brück, W., & Bähr, M. (2010). Mechanisms of acute axonal degeneration in the optic nerve in vivo. *Proceedings of the National Academy of Sciences*, *107*(13), 6064-6069.

Kocyigit, A., Kasap, B., Guler, E. M., Kaleli, H. N., Kesmen, M., Dikilitas, M., & Karatas, E. (2019). An optimum dose of olive leaf extract improves insulin receptor substrate-1, tyrosine kinase, and glucose transporters, while high doses have genotoxic and apoptotic effects. *American Journal of Plant Sciences*, *10*(11), 1933-1948.

Lamb, T. D. (2016). Why rods and cones? *Eye*, *30*(2), 179-185.

Lemoine, D., Simon, E., Buc, G., & Deterre, M. (2020). In vitro reliability testing and in vivo lifespan estimation of wireless pixium vision PRIMA photovoltaic subretinal prostheses suggest prolonged durability and functionality in clinical practice. *Journal of neural engineering*, *17*(3), 035005.

Levkovitch-Verbin, H. (2004). Animal models of optic nerve diseases. *Eye*, *18*(11), 1066-1074.

Limb, G. A., Salt, T. E., Munro, P. M., Moss, S. E., & Khaw, P. T. (2002). In vitro characterization of a spontaneously immortalized human Muller cell line (MIO-M1). *Investigative ophthalmology & visual science*, *43*(3), 864-869.

Lin, Y., Wang, J., Zhang, Z. G., Bai, H., Li, Y., Zhu, D., & Zhan, X. (2015). An electron acceptor challenging fullerenes for efficient polymer solar cells. *Advanced Materials*, *27*(7), 1170-1174.

Liu, J., Jung, H., Dubra, A., & Tam, J. (2018). Cone photoreceptor cell segmentation and diameter measurement on adaptive optics images using circularly constrained active contour model. *Investigative ophthalmology & visual science*, *59*(11), 4639-4652.

Liu, X., Chen, P., Ding, X., Liu, A., Li, P., Sun, C., & Guan, H. (2022). A narrative review of cortical visual prosthesis systems: the latest progress and significance of nanotechnology for the future. *Annals of Translational Medicine*, *10*(12).

Liu, X., Feng, L., Shinde, I., Cole, J. D., Troy, J. B., & Saggere, L. (2020). Correlation between retinal ganglion cell loss and nerve crush force-impulse established with instrumented tweezers in mice. *Neurological research*, *42*(5), 379-386.

Lugo, K., Miao, X., Rieke, F., & Lin, L. Y. (2012). Remote switching of cellular activity and cell signaling using light in conjunction with quantum dots. *Biomedical Optics Express*, *3*(3), 447-454.

Maeda, K., Sawada, A., Matsubara, M., Nakai, Y., Hara, A., & Yamamoto, T. (2004). A novel neuroprotectant against retinal ganglion cell damage in a glaucoma model and an optic nerve crush model in the rat. *Investigative ophthalmology & visual science*, *45*(3), 851-856.

Marshall, J. D., & Schnitzer, M. J. (2013). Optical strategies for sensing neuronal voltage using quantum dots and other semiconductor nanocrystals. *Acs Nano*, *7*(5), 4601-4609.

Martino, N., Ghezzi, D., Benfenati, F., Lanzani, G., & Antognazza, M. R. (2013). Organic semiconductors for artificial vision. *Journal of Materials Chemistry B*, *1*(31), 3768-3780.

Maya-Vetencourt, J. F., Ghezzi, D., Antognazza, M. R., Colombo, E., Mete, M., Feyen, P., Desii, A., Buschiazzo, A., Di Paolo, M., & Di Marco, S. (2017). A fully organic retinal prosthesis restores vision in a rat model of degenerative blindness. *Nature materials*, *16*(6), 681-689.

Medagoda, D. I., & Ghezzi, D. (2021). Organic semiconductors for light-mediated neuromodulation. *Communications Materials*, *2*(1), 111.

Melikov, R., Srivastava, S. B., Karatum, O., Dogru-Yuksel, I. B., Dikbas, U. M., Kavakli, I. H., & Nizamoglu, S. (2020). Bidirectional optical neuromodulation using capacitive charge-transfer. *Biomedical Optics Express*, *11*(11), 6068-6077.

Menzel-Severing, J., Laube, T., Brockmann, C., Bornfeld, N., Mokwa, W., Mazinani, B., Walter, P., & Roessler, G. (2012). Implantation and explantation of an active epiretinal visual prosthesis: 2-year follow-up data from the EPIRET3 prospective clinical trial. *Eye*, *26*(4), 501-509.

Merrill, D. R., Bikson, M., & Jefferys, J. G. (2005). Electrical stimulation of excitable tissue: design of efficacious and safe protocols. *Journal of neuroscience methods*, *141*(2), 171-198.

Mesentier-Louro, L. A., & Liao, Y. J. (2019). Optic nerve regeneration: considerations on treatment of acute optic neuropathy and end-stage disease. *Current Ophthalmology Reports*, *7*, 11-20.

Mesentier-Louro, L. A., Teixeira-Pinheiro, L. C., Gubert, F., Vasques, J. F., Silva-Junior, A. J., Chimeli-Ormonde, L., Nascimento-dos-Santos, G., Mendez-Otero, R., & Santiago, M. F. (2019). Long-term neuronal survival, regeneration, and transient target reconnection after optic nerve crush and mesenchymal stem cell transplantation. *Stem Cell Research & Therapy*, *10*, 1-12.

Milos, F., Tullii, G., Gobbo, F., Lodola, F., Galeotti, F., Verpelli, C., Mayer, D., Maybeck, V., Offenhäusser, A., & Antognazza, M. R. (2021). High aspect ratio and light-sensitive micropillars based on a semiconducting polymer optically regulate neuronal growth. *ACS Applied Materials & Interfaces*, *13*(20), 23438-23451.

Mitchell, P., Liew, G., Gopinath, B., & Wong, T. Y. (2018). Age-related macular degeneration. *The Lancet*, *392*(10153), 1147-1159.

Molday, R. S., & Moritz, O. L. (2015). Photoreceptors at a glance. *Journal of cell science*, *128*(22), 4039-4045.

Morrison, J. C., Guo, W. O. C. Y., & Johnson, E. C. (2011). Pathophysiology of human glaucomatous optic nerve damage: insights from rodent models of glaucoma. *Experimental eye research*, *93*(2), 156-164.

Muqit, M. M., Velikay-Parel, M., Weber, M., Dupeyron, G., Audemard, D., Corcostegui, B., Sahel, J., & Le Mer, Y. (2019). Six-month safety and efficacy of the intelligent retinal implant system II device in retinitis pigmentosa. *Ophthalmology*, *126*(4), 637-639.

Newman, N. J., Yu-Wai-Man, P., Biousse, V., & Carelli, V. (2023). Understanding the molecular basis and pathogenesis of hereditary optic neuropathies: towards improved diagnosis and management. *The Lancet Neurology*, *22*(2), 172-188.

Nguyen, C. T., Tsai, T. I., He, Z., Vingrys, A. J., Lee, P. Y., & Bui, B. V. (2016). Simultaneous recording of electroretinography and visual evoked potentials in anesthetized rats. *Journal of visualized experiments: JoVE*(113), 54158.

Nowak, J. Z. (2006). Age-related macular degeneration (AMD): pathogenesis and therapy. *Pharmacological reports*, *58*(3), 353.

Ohlsson, M., Mattsson, P., & Svensson, M. (2004). A temporal study of axonal degeneration and glial scar formation following a standardized crush injury of the optic nerve in the adult rat. *Restorative neurology and neuroscience*, *22*(1), 1-10.

Onal, A., Kaya, T. S., Metin, O. n., & Nizamoglu, S. (2024). Emergence of Near-Infrared Photoluminescence via ZnS Shell Growth on the AgBiS2 Nanocrystals. *Chemistry of Materials*.

Oster, G. (1970). Phosphenes. *Scientific American*, *222*(2), 82-87.

Paknahad, J., Machnoor, M., Lazzi, G., & Gokoffski, K. K. (2022). The influence of electrode properties on induced voltage gradient along the rat optic nerve. *IEEE journal of electromagnetics, RF and microwaves in medicine and biology*, *6*(3), 321-330.

Palanker, D., Le Mer, Y., Mohand-Said, S., Muqit, M., & Sahel, J. A. (2020). Photovoltaic restoration of central vision in atrophic age-related macular degeneration. *Ophthalmology*, *127*(8), 1097-1104.

Palanker, D., Le Mer, Y., Mohand-Said, S., & Sahel, J.-A. (2022). Simultaneous perception of prosthetic and natural vision in AMD patients. *Nature communications*, *13*(1), 1-6.

Pappas, T. C., Wickramanyake, W. S., Jan, E., Motamedi, M., Brodwick, M., & Kotov, N. A. (2007). Nanoscale engineering of a cellular interface with semiconductor nanoparticle films for photoelectric stimulation of neurons. *Nano letters*, *7*(2), 513-519.

Pardue, M. T., & Allen, R. S. (2018). Neuroprotective strategies for retinal disease. *Progress in retinal and eye research*, *65*, 50-76.

Paxinos, G., & Watson, C. (2006). *The rat brain in stereotaxic coordinates: hard cover edition*. Elsevier.

Petoe, M. A., Abbott, C. J., Titchener, S. A., Kolic, M., Kentler, W. G., Nayagam, D. A., Baglin, E. K., Kvansakul, J., Barnes, N., & Walker, J. G. (2025). A second-generation (44-channel) suprachoroidal retinal prosthesis: a single-arm clinical trial of feasibility. *Ophthalmology Science*, *5*(1), 100525.

Provis, J. M., Dubis, A. M., Maddess, T., & Carroll, J. (2013). Adaptation of the central retina for high acuity vision: cones, the fovea and the avascular zone. *Progress in retinal and eye research*, *35*, 63-81.

Rando, R. R. (2001). The biochemistry of the visual cycle. *Chemical reviews*, *101*(7), 1881-1896.

Ren, M., & Xu, J. (2022). Quantum dot nanocomposites for flexible retina. *Nature Nanotechnology*, *17*(8), 819-820.

Roessler, G., Laube, T., Brockmann, C., Kirschkamp, T., Mazinani, B., Goertz, M., Koch, C., Krisch, I., Sellhaus, B., & Trieu, H. K. (2009). Implantation and explantation of a wireless epiretinal retina implant device: observations during the EPIRET3 prospective clinical trial. *Investigative ophthalmology & visual science*, *50*(6), 3003-3008.

Rühle, S., Shalom, M., & Zaban, A. (2010). Quantum-dot-sensitized solar cells. *ChemPhysChem*, *11*(11), 2290-2304.

Russell, S., Bennett, J., Wellman, J. A., Chung, D. C., Yu, Z.-F., Tillman, A., Wittes, J., Pappas, J., Elci, O., & McCague, S. (2017). Efficacy and safety of voretigene neparvovec (AAV2-hRPE65v2) in patients with RPE65-mediated inherited retinal dystrophy: a randomised, controlled, open-label, phase 3 trial. *The Lancet*, *390*(10097), 849-860.

Sakaguchi, H., Kamei, M., Fujikado, T., Yonezawa, E., Ozawa, M., Cecilia-Gonzalez, C., Ustariz-Gonzalez, O., Quiroz-Mercado, H., & Tano, Y. (2009). Artificial vision by direct optic nerve electrode (AV-DONE) implantation in a blind patient with retinitis pigmentosa. *Journal of Artificial Organs*, *12*, 206-209.

Sanes, J. R., & Masland, R. H. (2015). The types of retinal ganglion cells: current status and implications for neuronal classification. *Annual review of neuroscience*, *38*(1), 221-246.

Sarikcioglu, L. (2007). Otfrid Foerster (1873–1941): one of the distinguished neuroscientists of his time. *Journal of Neurology, Neurosurgery & Psychiatry*, *78*(6), 650-650.

Sarikcioglu, L., Demir, N., & Demirtop, A. (2007). A standardized method to create optic nerve crush: Yasargil aneurysm clip. *Experimental eye research*, *84*(2), 373-377.

Savva, A., Hama, A., Herrera-López, G., Schmidt, T., Migliaccio, L., Steiner, N., Kawan, M., Fiumelli, H., Magistretti, P. J., & McCulloch, I. (2023). Photo-Chemical Stimulation of Neurons with Organic Semiconductors. *Advanced Science*, *10*(31), 2300473.

Shaheen, N., Khaled, M., Seo, S., Bezchlibnyk, Y., Flouty, O., & Bharmauria, V. (2024). Neurostimulation in neuro-ophthalmology: Mechanisms and therapeutic potential.

Silverå Ejneby, M., Jakešová, M., Ferrero, J. J., Migliaccio, L., Sahalianov, I., Zhao, Z., Berggren, M., Khodagholy, D., Đerek, V., & Gelinas, J. N. (2022). Chronic

electrical stimulation of peripheral nerves via deep-red light transduced by an implanted organic photocapacitor. *Nature biomedical engineering*, *6*(6), 741-753.

Srivastava, G. K., López-Paniagua, M., & Crespo Millas, S. (2022). Advanced Therapy and Clinical Trials to Treat Patients with Optic Nerve Diseases. *Neurotoxicity Research*, *40*(6), 1739-1757.

Stingl, K., Bartz-Schmidt, K. U., Besch, D., Chee, C. K., Cottriall, C. L., Gekeler, F., Groppe, M., Jackson, T. L., MacLaren, R. E., & Koitschev, A. (2015). Subretinal visual implant alpha IMS–clinical trial interim report. *Vision research*, *111*, 149-160.

Stingl, K., Schippert, R., Bartz-Schmidt, K. U., Besch, D., Cottriall, C. L., Edwards, T. L., Gekeler, F., Greppmaier, U., Kiel, K., & Koitschev, A. (2017). Interim results of a multicenter trial with the new electronic subretinal implant alpha AMS in 15 patients blind from inherited retinal degenerations. *Frontiers in neuroscience*, *11*, 445.

Strauss, O. (2005). The retinal pigment epithelium in visual function. *Physiological reviews*.

Veraart, C., Wanet-Defalque, M. C., Gérard, B., Vanlierde, A., & Delbeke, J. (2003). Pattern recognition with the optic nerve visual prosthesis. *Artificial organs*, *27*(11), 996-1004.

Wang, A. L., Knight, D. K., Thanh-thao, T. V., & Mehta, M. C. (2019). Retinitis pigmentosa: review of current treatment. *International ophthalmology clinics*, *59*(1), 263-280.

Wells-Gray, E., Choi, S., Bries, A., & Doble, N. (2016). Variation in rod and cone density from the fovea to the mid-periphery in healthy human retinas using adaptive optics scanning laser ophthalmoscopy. *Eye*, *30*(8), 1135-1143.

Wilke, R., Gabel, V.-P., Sachs, H., Schmidt, K.-U. B., Gekeler, F., Besch, D., Szurman, P., Stett, A., Wilhelm, B., & Peters, T. (2011). Spatial resolution and perception of patterns mediated by a subretinal 16-electrode array in patients blinded by hereditary retinal dystrophies. *Investigative ophthalmology & visual science*, *52*(8), 5995-6003.

Wu, K. Y., Kulbay, M., Toameh, D., Xu, A. Q., Kalevar, A., & Tran, S. D. (2023). Retinitis pigmentosa: novel therapeutic targets and drug development. *Pharmaceutics*, *15*(2), 685.

Yang, K., Oh, J. Y., Lee, J. S., Jin, Y., Chang, G.-E., Chae, S. S., Cheong, E., Baik, H. K., & Cho, S.-W. (2017). Photoactive poly (3-hexylthiophene) nanoweb for optoelectrical stimulation to enhance neurogenesis of human stem cells. *Theranostics*, *7*(18), 4591.

Yang, Y., Zhang, Z.-G., Bin, H., Chen, S., Gao, L., Xue, L., Yang, C., & Li, Y. (2016). Side-chain isomerization on an n-type organic semiconductor ITIC acceptor makes 11.77% high efficiency polymer solar cells. *Journal of the American Chemical Society*, *138*(45), 15011-15018.

Yu-Wai-Man, P. (2015). Traumatic optic neuropathy—Clinical features and management issues. *Taiwan journal of ophthalmology*, *5*(1), 3-8.

Zhao, N., Hao, X.-N., Huang, J.-M., Song, Z.-M., & Tao, Y. (2024). Crosstalk between microglia and Müller glia in the age-related macular degeneration: role and therapeutic value of neuroinflammation. *Aging and Disease*, *15*(3), 1132.